Universitat Autònoma de Barcelona

The Clinical Description, Molecular Etiology, and Pathophysiological studies in Cutaneous Skeletal Hypophosphatemia Syndrome: a Mosaic Disorder of Activating RAS Mutations

Diana Ovejero Crespo

DOCTORAL THESIS

The Clinical Description, Molecular Etiology, and Pathophysiological studies in Cutaneous Skeletal Hypophosphatemia Syndrome: a Mosaic Disorder of Activating RAS Mutations

Diana Ovejero Crespo

Thesis directors:
Dra. Ana Chico Ballesteros
Dra. Rosa Corcoy Plà
Dr. Adolfo Díez Pérez

Thesis tutor:
Prof. Alberto de Leiva Hidalgo

Programa de Doctorat en Medicina.
Departament de Medicina.
Universitat Autònoma de Barcelona.
2017

Syndrome: a Mosaic Disorder of Activating RAS Mutations

Universitat Autònoma de Barcelona

La Dra. Rosa Corcoy Plà y la Dra. Ana Chico Ballesteros , Doctoras en Medicina y Profesoras Asociadas del Departamento de Medicina de la Universitat Autònoma de Barcelona, el Dr. Adolfo Díez Pérez, Doctor en Medicina y Profesor Titular del Departamento de Medicina de la Universitat Autònoma de Barcelona, y el Prof. Alberto de Leiva Hidalgo, Doctor en Medicina y Catedrático Emérito de la Universitat Autònoma de Barcelona certifican:

- Que Diana Ovejero Crespo ha realizado bajo su dirección/tutela la presente tesis doctoral: **"The Clinical Description, Molecular Etiology, and Pathophysiological studies in Cutaneous Skeletal Hypophosphatemia Syndrome: a Mosaic Disorder of Activating RAS Mutations"** y que es apta para su defensa delante de un tribunal para optar al título de Doctor en Medicina en la Universitat Autònoma de Barcelona.

Barcelona, Mayo de 2017

Doctoranda:

Diana Ovejero Crespo

Directores:

Dra. Rosa Corcoy Plà Dra. Ana Chico Ballesteros Dr. Adolfo Díez Pérez

Tutor:

Prof. Alberto de Leiva Hidalgo

National Institute of Dental
and Craniofacial Research

I would like to acknowledge that the work presented in this doctoral thesis was generated at the National Institute of Dental and Craniofacial Research, National Institutes of Health, Bethesda, Maryland, United States of America.

ACKNOWLEGEMENTS

La realización de esta tesis doctoral no hubiera sido posible sin la ayuda de un gran número de personas a las que quiero expresar mi gratitud:

The completion of this doctoral thesis wouldn't have been possible without the help of a great number of people to whom I'd like to express my gratitude:

A mis directores de tesis, la Dra. Rosa Corcoy y la Dra. Ana Chico del Servicio de Endocrinología y Nutrición del Hospital de la Santa Creu i Sant Pau y al Prof. Adolfo Díez, Jefe Emérito del Servicio de Medicina Interna del Hospital del Mar, por su apoyo y sus consejos durante la realización de esta tesis.

A mi tutor de tesis, el Prof. Alberto de Leiva, Jefe del Servicio de Endocrinología y Nutrición del Hospital de la Santa Creu i Sant Pau, por haberme animado a tomar la más que sabia decisión de trasladarme a Estados Unidos para formarme como investigadora en los National Institutes of Health y por su ayuda en ese proceso.

A mis compañeros y mentores del Servicio de Endocrinología y Nutrición del Hospital de la Santa Creu i Sant Pau por haberme acompañado y ayudado siempre que lo he necesitado durante mis años de formación como *azucarillo*. Espero que no me tengáis en cuenta que haya reemplazado la insulina por la hidroxiapatita. Mención especial a mi co-R, la Dra. Inka Membrillo Donaire, que además de recordarme cada otoño de los pagos de tutela de la tesis (y pagármelos más de una vez), ha estado siempre ahí, en los buenos y en los malos momentos, como gran amiga y compañera que es.

A la fundación Obra Social "la Caixa" por haber creído en mí y regalarme la mejor experiencia, personal y profesional, de mi vida.

To Dr. Keith Choate and Young Lim for being exceptional collaborators, for making Dermatology so fascinating, and for elucidating the genetic etiology of CSHS.

To the NIDCR's Veterinary Resource Core staff for taking such good care of my mice and me even when I (completely involuntarily) skipped the rules.

To my CSDB family: Pam Robey, Larry Fisher, Marian Young, Kenn Holmbeck, Vardit Kram, Lynn Cross, Eva Mezey, Natasha Cherman, Sergei Kutznetsov, Li Li, Tina Kilts, and all the fellows. Thank you for your infinite patience with me, for your knowledge, for guiding me in the basic science universe, and for your warmth during my years at the NIDCR. Without your invaluable help this thesis wouldn't have been possible.

To the Section on Skeletal Disorders and Mineral Homeostasis, aka, my lab! Mary Scott, Andrea, Drea, Diala, Alison, Rachel, Beth, Lori, Michelle, Pablo, Jason, Cemre, Sri, Nisan, and Howard: I can't conceive a more fun, knowledgeable, supporting, friendly, and feminist group to work with. You are family to me. Y no me olvido de Luis, mi hermano de PBS, que tantísimo ha contribuido en mi formación como científica. Que aburrida es la vida desde que no puedo contradecirte en todo.

To the patients with CSHS and to their families. Thank you for allowing me to learn so much from you. I can only hope that our efforts will culminate one day in your health, well-being and in very strong bones for anybody affected with CSHS.

A mi querido padre, porque a pesar de su afición a discrepar conmigo, me brinda su apoyo siempre que le necesito. Y a la Beni y al Paco por estar siempre allí.

A los que se fueron, pero siguen en mi: a mi bohemia y maravillosa madre, por haberme transmitido un cachito de su extraordinaria creatividad y curiosidad que tan útiles me han resultado en mi carrera como investigadora. Y a mi abuelo Florián por recibir con más entusiasmo que nadie cualquier logro académico mío por insignificante que fuera. Nadie estaría más orgulloso de este trabajo que él.

A Ricardo, sin duda la mejor aportación que me ha dado la ciencia. Gracias por tu paciencia, tu amor, y por tu apoyo incondicional. Y por darme a Matilde, mi más fiel compañera durante la preparación de esta tesis y la que seguro se convertirá en el proyecto más fascinante de nuestras vidas.

To Dr. Michael T. Collins, chief of the Section on Skeletal Disorders and Mineral Homeostasis, NIDCR, NIH. For teaching me everything I know about bones, mosaicism, and biblical stories. For his warmth, patience, and guidance throughout my years at the NIH. For being the main supervisor, supporter, and sponsor of this work. I couldn't be more grateful for having had such an outstanding mentor.

To Mike Collins.

A Ricardo, a Matilde,
a mis padres y,
a mi abuelo Florián.

"El modo de dar una vez en el clavo es dar cien veces en la herradura."
-Miguel de Unamuno

TABLE OF CONTENTS

SUMMARY

Introduction: Cutaneous Skeletal Hypophosphatemia Syndrome (CSHS) is an ultra-rare mosaic disorder caused by postzygotic *RAS* mutations that is defined by the association of epidermal and/or melanocytic nevi, fibroblast growth factor-23 (FGF23) excess, and a skeletal dysplasia. Because of its rarity, CSHS has been inadequately characterized. Further, unknown are the roles of *RAS* mutations in dysplastic bone formation and the source and physiopathology of FGF23 overproduction in CSHS. **Thesis hypotheses:** 1) A thorough phenotypic assessment of patients with CSHS, and the analysis of all potential reported CSHS cases will provide important clinical information, 2) Dysplastic bone is the source of FGF23 overproduction in CSHS and, 3) The generation of appropriate experimental models will inform of CSHS's physiopathology. **Objectives:** 1) To clinically characterize CSHS through the study of a cohort of subjects and a review of all reported cases, 2) To identify the physiopathology of FGF23 overproduction in CSHS, 3) To investigate the effects of hyperactive RAS on dysplastic bone formation. **Subjects and methods:** Five CSHS subjects were phenotyped and underwent prospective data collection. A review of the literature identified 51 subjects in whom the findings were compatible with CSHS. Data on nevi, bone histology, mineral and skeletal alterations, abnormalities in other tissues, and response to treatments of hypophosphatemia were analyzed. To assess the effects of *RAS* mutations on FGF23 production in "bone-like" cells, FGF23 production/gene expression was measured in 1) human bone marrow stromal cells (hBMSCs) and 2) IDG-SW3 cells transduced with mutated adenoviral *RAS* constructs, in 3) mutant hBMSCs from a CSHS patient, and in 4) IDG-SW3 cells treated with media in which mutant CSHS hBMSCs had been cultured. To further characterize CSHS bone histology, an ossicle formation assay was performed by transplanting mutant CSHS hBMSCs subcutaneously into immunocompromised mice. Finally, 3 tissue-specific mutant *Ras knock-in* mouse models were designed through Cre-Lox recombination technology to investigate the effects of activating *Ras* mutations in bone. The models consisted in the activation of a LoxP-STOP-LoxP-KrasG12D (LSL-KrasG12D) transgene through 3 different Cre-recombinases driven by the following promoters: 1) tamoxifen-inducible 3.6 kb collagen type I α-1, 2) tamoxifen-inducible paired-related homeobox gene-1(Prx1), and 3) non-inducible Prx1. **Results:** From a clinical standpoint, fractures, limb deformities, and scoliosis affected most CSHS subjects. Hypophosphatemia was not present at birth. Bone histology only revealed severe osteomalacia without other obvious abnormalities. Skeletal dysplasia was reported in all anatomical compartments. Phosphate and calcitriol supplementation was effective in treating rickets in most patients. Convincing data that nevi removal improved blood phosphate levels was lacking. An age-dependent improvement in mineral abnormalities was observed. A spectrum of extra-osseous/extra-cutaneous manifestations that included both benign and malignant neoplasms was present in many subjects, although osteosarcoma remains unreported. From an experimental standpoint, increased FGF23 production/expression was not detected with any of the experimental conditions in the *in vitro* experiments. Poor bone formation with the ossicle assay hampered histological characterization of the ossicles. No abnormal findings were detected in the models featuring the tamoxifen-inducible promoters. No double transgenic offspring harboring both LSL-KrasG12D and the non-inducible Prx1-Cre recombinase were identified.

Conclusions: The study of patients and reports of subjects with CSHS provided relevant and novel clinical information. Also, the analysis of affected patient tissues allowed further appreciation of the effects of hyperactive RAS in different organs. Still, the source of excess FGF23 in CSHS remains unknown, although data indicate it is probably not produced by the nevi. Other conclusions include the lack of suitability of BMSCs to study FGF23 production/expression, the poor reproducibility of the subcutaneous ossicle formation assay, and the lethality of widespread *Kras* mutations in early embyrionic skeletal cells in mice.

ABBREVIATIONS

α-MEM: α-modified minimum essential medium
ADHR: autosomal dominant hypophosphatemic rickets
BMD: bone mineral density
BMSC: bone marrow stromal cell
BGP: β- glycerophosphate
cDNA: complementary DNA
CKD: chronic kidney disease
CMN: congenital melanocytic nevus
Col 3.6: 3.6 kb fragment of the collagen type I alpha 1 gene
Col1-CreER: tamoxifen-inducible Col 3.6 cre recombinase
CSHS: cutaneous skeletal hypophosphatemia syndrome
CT: computed tomography
C_T: critical threshold
DEXA: dual-energy X-ray absorptiometry
DMP1: dentin matrix protein 1
EDTA: ethylenediaminetetraacetic acid
ELISA: enzyme-linked immunosorbent assay
EN: epidermal nevi
ENPP1: ectonucleotide pyrophosphatase/phosphodiesterase 1
FAM20C: family with sequence similarity 20 member C
FBS: fetal bovine serum
FD: fibrous dysplasia
FFPE: formalin-fixed paraffin embedded
FGF: fibrobast growth factor
FGF23: fibroblast growth factor 23
FGFR: fibroblast growth factor receptor
FTC: familial tumoral calcinosis
GALNT3: UDP-N-acetyl-α-D-galactosamine polypeptide N-acetylga-lactosaminyltransferase
GAPDH: glyceraldehyde 3-phosphate dehydrogenase
GCMN: giant congenital melanocytic nevus
GDP: guanosine diphosphate
GFP: green fluorescent protein
GTP: guanosine triphosphate
HHS: hyperostosis hyperphosphatemic syndrome
HIF1α: hypoxia inducible factor 1-alpha
H&E: hematoxylin-eosin
IF: immunofluorescence
INFγ: interferon gamma
IRB: Institutional Review Board
KEN: keratinocytic epidermal nevi
LSL: LoxP-STOP codon-LoxP
Luc: luciferase
MAPK: mitogen-activated protein kinase
MAS: McCune-Albright Syndrome
MMA: methylmethacrylate

MRI: magnetic resonance imaging
Na18F: 18F-Sodium Fluoride
NaPi: sodium/phosphate co-transporter
NIDCR: National Institute of Dental and Craniofacial Research
NIH: National Institutes of Health
NS: nevus sebaceous
PBS: phosphate buffered solution
PCR: polymerase chain reaction
PET: positron emission tomography
PFA: paraformaldehyde
PHEX: phosphate regulating endopeptidase homolog X-Linked
PMT: phosphaturic mesenchymal tumor
PPK: phacomatosis pigmentokeratotica
Prx1: paired-related homeobox gene-1
Prx1-CreER: tamoxifen-inducible Prx1 cre recombinase
PTH: parathyroid hormone
RT-PCR: real-time PCR
SPC: subtilisin-like pro-protein convertases
SPECT: single photon emission computed tomography
TIO: tumor-induced osteomalacia
TRP: tubular reabsorption of phosphate
US: ultrasound
VDR: vitamin D receptor
WT: wild type
XLH: X-linked hypophosphatemia

1. INTRODUCTION

1.1 Genetic Mosaicism

A mosaic is an image created through the assembly of small pieces of material that typically differ in size, color and shape. This artistic technique gave rise to the concept of genetic mosaicism, a condition in which non-germline mutations cause individuals to harbor at least two cell populations with distinct genotypes [1]. The mosaic phenotype can vary enormously depending on the type of genetic alteration (e.g. trisomies, isochromosomes, single nucleotide variant etc), the number and type of cells affected, and the point in time at which mutagenesis occurs [1]. Regarding this last point, mutations occurring in multipotent cells during early embryogenesis lead to more extensive and complex phenotypes than those that occur at a later stage of development. From a clinical perspective, it is important to determine whether the mutation is limited to somatic cells (somatic mosaicism) or involves the germ cells (gonadal mosaicism), as the latter have the potential to transmit the mutation to their offspring [1]. Further, mosaics should be distinguished from chimaeras, a term used to describe individuals in whom there are different cellular genotypes that result from the fusion of at least two zygotes, not due to mutations [2].

Some genetic abnormalities identified in the mosaic state can also be found constitutionally e.g. trisomies of chromosome13, 18, or 21. However, certain disorders, including cancers, have only been reported in the mosaic state. The generally accepted belief is that the mutations that cause disorders like cancer would be lethal in germline transmission and can only survive through mosaicism, hence they are considered sporadic and non-inheritable [3]. Such mutations occasionally affect the embryo. A hallmark of this type of developmental mosaicism is McCune-Albright syndrome (MAS), a disorder caused by postzygotic mutations in *GNAS* [4]. Early embryonic mutations in *GNAS* typically result in polyostotic fibrous dysplasia (FD) of the bone (mosaic skeletal lesions), cutaneous café-au-lait spots, and a number of well-established endocrinopathies, including precious puberty, hyperthyroidism, growth hormone excess, and fibroblast growth factor 23 (FGF23)-mediated hypophosphatemia [5]. In contrast, *GNAS* mutations that occur in differentiated (i.e. not multipotent) fetal cells will lead exclusively to tissue-specific lesions such as monostotic FD, or isolated café-au-lait spots.

A strikingly similar developmental pattern to that of MAS is observed in cases of congenital nevi associated to mosaic skeletal lesions and hypophosphatemic rickets. Unlike FD, which has been studied in-depth, the mineral and skeletal abnormalities that have been reported in association with nevoid syndromes have not been adequately described in terms of the spectrum and natural history, nor has the underlying pathophysiology been explored.

1.2 Cutaneous nevi

Congenital nevi are benign, circumscribed, long-lasting lesions affecting dermal and/or epidermal structures, present since birth or first months of life, and by definition reflect mosaicism [6].

Epidermal nevi (EN) derive from epidermal structures such as keratinocytes, sebaceous glands, and/or hair follicles [7]. The most prevalent are keratinocytic epidermal nevi (KEN) and nevus sebaceous (NS), commonly known as birthmarks, with an estimated incidence of 1/1000 births [8]. KEN feature acanthosis (hyperplasia of the stratum basale and spinosum), hyperkeratosis (thickening of the stratum corneum), and papillomatosis (enlargement of contiguous dermal papillae), which contributes to their characteristic verrucous appearance (Figure 1D, image extracted from [7]). KEN typically affect the extremities, torso and back and are distributed in a linear or whorly fashion along the lines of Blaschko (Figure 1.1A, image extracted from [9]). These lines are considered to trace the migration of skin cell progenitors during embryogenesis, and only become visible in certain pigmented mosaic disorders [6]. On the other hand, NS typically appear as round, waxy, alopecic patches at the scalp and/or face (figure 1.1B, extracted from [10]). The histological hallmark of NS is sebaceous hyperplasia, but like KEN, also features acanthosis, hyperkeratosis and papillomatosis. Occasionally, systemic abnormalities can accompany epidermal nevi, frequently in the setting of extensive skin lesions; this constellation of findings is referred to as epidermal nevus syndrome (ENS) [11]. The best characterized ENS is perhaps Schimmelpenning syndrome (OMIM #163200), defined by the association of NS with neurological, ophthalmological and skeletal anomalies [11].

Congenital melanocytic nevi (CMN), commonly known as moles, originate in the neural crest and derive from pigment-producing cells of melanocytic lineage [12]. Giant congenital melanocytic nevi (GCMN), defined as melanocytic lesions present at birth with an estimated diameter ≥20 cm in adulthood, are very rare (incidence estimated in <1:20,000 newborns), and have also been associated with abnormalities in extra-cutaneous tissues [13, 14]. GCMN also reflect cutaneous mosaicism but generally display a checkerboard pattern or large coat-like patches instead of following the lines of Blaschko [1] (figure 1.1 C, image extracted from [12].

Co-existance of EN and CMN are seen in phacomatosis pigmentokeratotica (PPK), an extremely rare disorder with frequent involvement of extra-cutaneous tissues [15] (figure 1.1 E, image extracted from [16]).

1.3 Rickets and Osteomalacia

Bone mineralization is a complex, orchestrated process that leads to the deposition of hydroxyapatite crystals, derived from calcium ions and inorganic phosphate ($Ca_{10}(PO4)_6(OH)_2$), along the collagen fibers in the extracellular matrix. Mineralization is indispensable for providing mechanical resistance and strength to the bone, as well as functioning as the body's main reservoir of mineral ions. The term rickets denotes inadequate mineralization at the growth plates, which are cartilaginous regions at the end of the long bones essential for linear growth. Growth plates only exists in the growing skeleton therefore, rickets are by definition a pediatric disorder. Osteomalacia refers to deficient mineralization of the bone matrix and can occur in children, usually concomitant to rickets, and in the adult skeleton [17].

Linear growth is determined by the process of endochondral bone formation that occurs in the growth plates [18]. The growth plate chondrocytes proliferate, become hypertrophic, secrete large quantities of cartilaginous matrix, and then undergo apoptosis. Following this stage, the

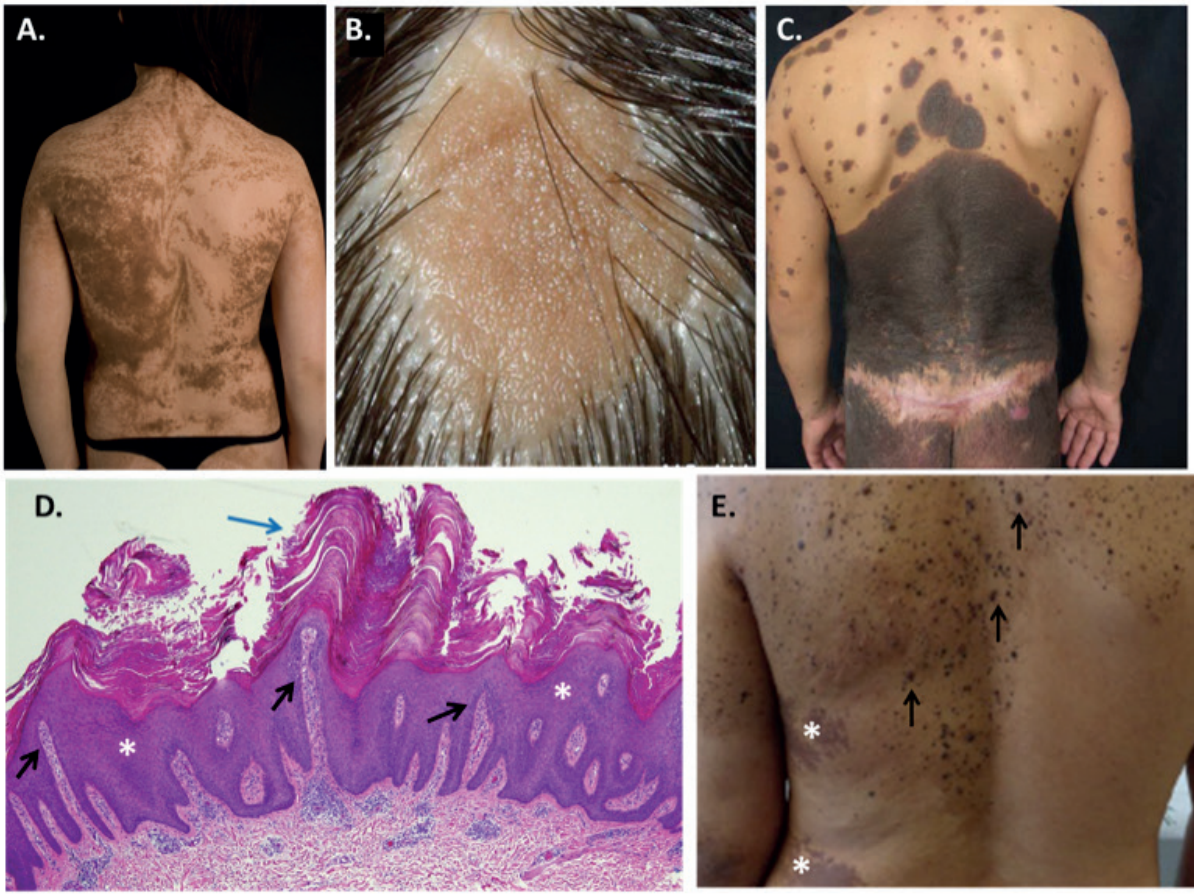

Figure 1.1 Examples of cutaneous nevi. (A.) Woman with an extensive keratinocytic epidermal nevi (KEN) following a whorly pattern that characterizes the lines of Blashcko (image adapted from [9]). (B.) Nevus sebaceous (NS) in the scalp (image adapted from [10]). This lesions tend to be localized in the face and scalp and appear as round, waxy and alopecic plaque as shown in the image. Histologically NS resemble KEN but also feature hyperplasia of the underlying sebaceous glands. Both KEN and NS are of epidermal origin and are a subtype of epidermal nevus. (C.) Giant congenital melanocytic nevus (GCMN) (image adapted from [12]). The most prominent lesion in this patient has a "bathing trunk" distribution which is typical of this type of cutaneous lesion. In contrast to the epidermal origin of KEN and NS, melanocytic nevi originate in the neural crest. (D.) KEN histology (hematoxilyn-eosin section) (image adapted from [7]). KEN's are characterized by (1) acanthosis, which consists in the hyperplasia of the stratums basale and spinosum, the 2 deepest layers of the epidermis (asterisks), (2) papillomatosis, or the enlargement of the dermal papillae (interdigitations of the dermis into the epidermis) (arrows), and (3) hyperkeratosis, or the thickening of the outer layer of the epidermis, the stratum corneum, featuring excessive keratin accumulation (blue arrow). These abnormalities are also present in many other nevi in addition to additional specific features that define each subtype. (E). Man with phacomatosis pigmentokeratotica (PPK) (image adapted from [16]). PPK is characterized by the coexistance of epidermal nevi (asterisks) of epidermal origin, and nevus spilus (arrows) of neural crest origin.

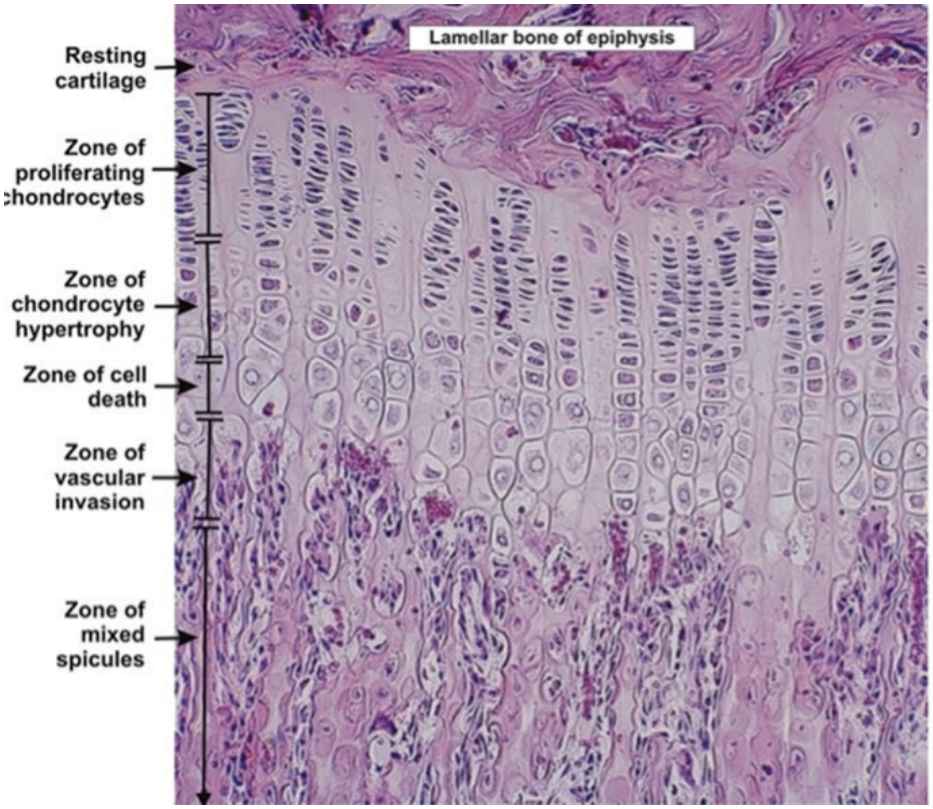

Figure 1.2 Histology (hematoxilin-eosin section) of a growth plate showing the different stages of chondrocyte transformation and endochondral bone formation . Mixed spicules, refers to the areas of new bone deposition mixed with the cartilaginous matrix that will eventually be reabsorbed. Iimage adapted from [18].

matrix is mineralized and is partially reabsorbed by osteoclasts. This is followed by vascular invasion and the appearance of osteoprogenitor cells (bone marrow stromal cells, BMSCs) in the marrow space. Finally, osteoblasts, which derive from BMSCs, initiate bone deposition that eventually replaces the cartilaginous template ultimately leading to longitudinal growth (Figure 1.2., image adapted from [19]).

If the cartilaginous matrix in the growth plate is not adequately mineralized, vascular invasion is altered, and hypertrophic chondrocyte apoptosis impaired. This results in an abnormal accumulation of cartilage that alters the normal structure of the growth plate [18]. Radiographically, rickets can be detected by the widening, fraying and cupping of the metaphysis (Figure 1.3 A, image extracted from [20]). Rachitic abnormalities are more readily identified in rapidly growing bones such as the distal ulna and femur, proximal tibia, and costochondral junctions. Other clinical manifestations related to hypophosphatemia include lateral bowing of the femur and tibia, growth impairment, parietal and frontal bossing, craniotabes, and delayed fontanelle closure [17] (Figure 1.3.B, image extracted from [21]).

Osteomalacia occurs during bone remodeling when newly formed bone is not adequately mineralized, and results in excessive accumulation of osteoid (the unmineralized organic component of the bone) [18]. Bone remodeling, which is the process by which mature bone is resorbed and replaced by new bone, is a lifelong process. Therefore, osteomalacia is not limited to any age group. Typical clinical manifestations of hypophosphatemia include bone pain, muscle weakness, low-impact fractures, and gait abnormalities [22]. Pseudofractures, a.k.a. Looser zones or Milkman's lines, are the radiographic hallmark of osteomalacia and are the manifestation of insufficiency fractures, appearing as sclerotic lucencies perpendicular to

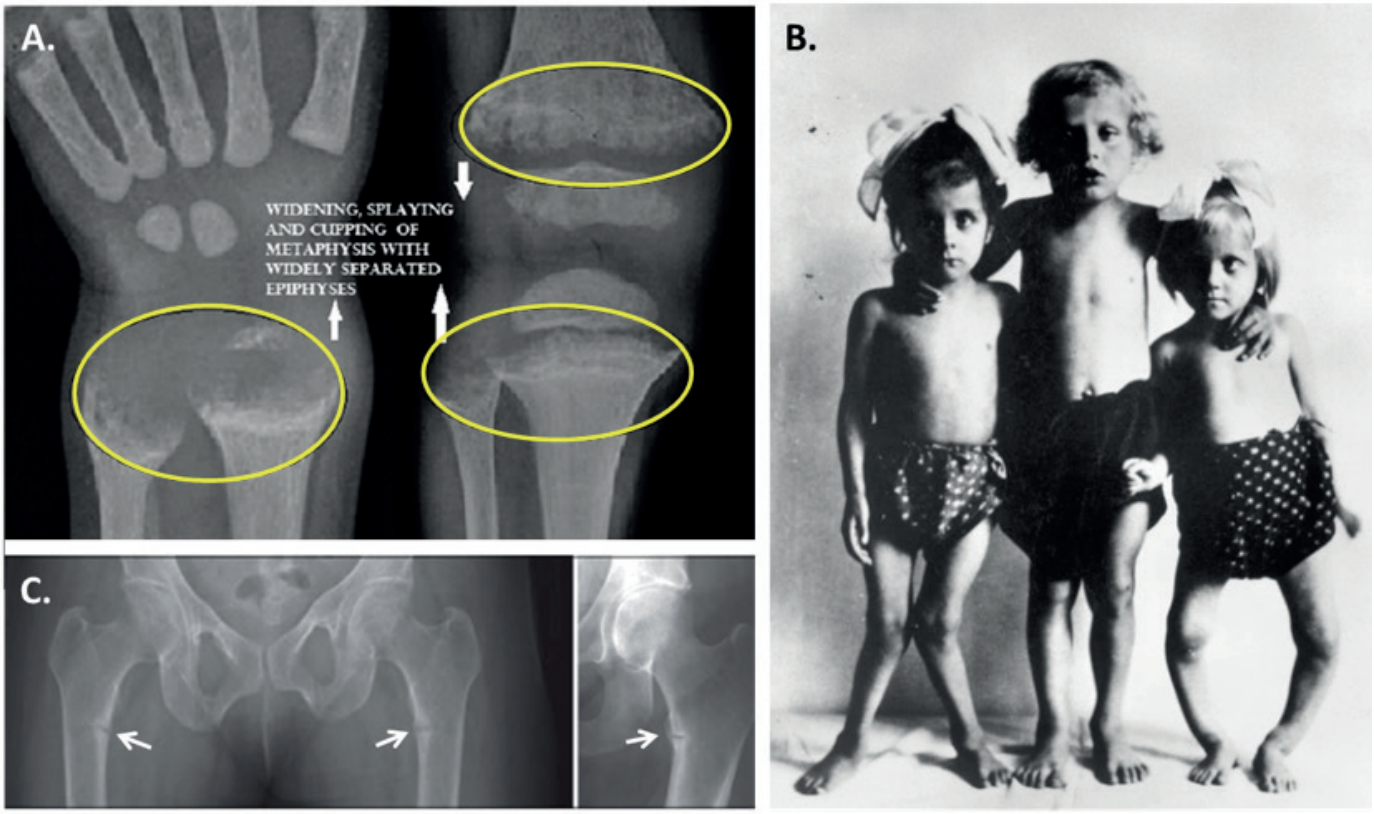

Figure 1.3 Features of rickets and osteomalacia. (A) Radiographs of the distal forearm and knee showing typical rachitic characteristics i.e. widening, cupping and fraying of the metaphysis (circles) (image adapted from [20]. (B.) Photograph taken in Scotland during the early 1900 where vitamin D deficiency secondary to low sun exposure and poor dietary intake was very prevalent (image adapted from [21]. The image shows children with rickets with lower limb bowing deformations and growth impairment. (C.) Pseudofractures at the femoral shaft (arrows) in an adult patient with osteomalacia (image adapted from [23]).

the cortex (Figure 1.3C, image extracted from [23]). Pseudofractures are often bilateral, and although they are most frequently detected in the femoral neck and femoral shaft, they can occur in sites that are rarely associated to fractures such as the scapula [17].

Depending on the nature of the mineral deficiency, rickets and ostemalacia are classified as either calcipenic (calcium deficiency) or phosphopenic (phosphate deficiency), although disorders such as hypophosphatasia, and substances, such as aluminium, that inhibit mineralization can also cause rickets/osteomalacia [18]. Vitamin D insufficiency, typically due to inadequate dietary intake, inadequate sun exposure, or malabsorption, leads to calcium deficiency and constitutes the main etiology of rickets and osteomalacia in children and adults worldwide [24, 25]. Insufficient calcium dietary intake and genetic forms of vitamin D resistance are other causes of calcipenic rickets. In addition, hypocalcemia leads to secondary hyperparathyroidism,that results in bone resportion and increased renal phosphate excretion which exacerbates the rachitic/osteomalacic state [26]. In contrast to vitamin D deficiency, which is typically an acquired disorder, phosphopenic rickets present primarily in the setting of a genetic defect. Phosphopenic rickets are mainly caused by renal phosphate wasting due to primary renal tubulopathies or excessive FGF23 secretion. A list of the main etiologies of rickets/osteomalacia is shown in Table 1.1.

Table 1.1 Etiologies of rickets/osteomalacia

Disorder	Gene/etiology	Inheritance	OMIM#	Phenotype	Treatment	Ref.
Calcipenic rickets/osteomalacia						
Acquired vitamin D decifiency	nutritional, ↓sun exposure, malabsorption, medication	N/A	N/A	Broad spectrum	Vitamin D	[24, 25]
1α-hydroxylase deficiency	Loss-of-function mutations of *CYP27B1*; CKD	AR	264700	Early onset (1st year); severe hypocalcemia,	Calcitriol, calcium	[27]
25-hydroxylase deficiency	Loss-of-function mutations of *CYP2R1*; liver disease, medications	AR	600081	Onset > 2 years	Calcidiol, calcium	[28]
Hereditary resistance to vitamin D	Loss-of-function mutations in *VDR*	AR	277440	Broad spectrum; rachitic onset occurs during 1-2 years; alopecia	↑↑ doses calcitriol and calcium	[29]
Calcium deficiency	nutritional	---	----	Presents around 3-5 years. Common in West/South Africa	Calcium and vitamin D	[30]
Phosphopenic rickets/osteomalacia						
Renal tubular disorders	Acquired, or genetic (several disorders e.g. cystinosis)	Depends on etiology	---	Variable, can include polyuria with hypovolemia, aminoaciduria, calciuria bicarbonaturia with acidosis	Variable, depending on phenotype: Bicarbonate, phosphate	[31]
Tumor-induced osteomalacia	FN1-FGFR1 fusions have been identified in causative tumors	N/A (sporadic)	---	Sudden onset; more frequent in adults. Usually very severe hyphosophatemia	Surgery; phosphate, calcitriol	[32]
Hereditary hypophosphatemic rickets due to FGF23↑	See table 1.2				Phosphate, calcitriol, anti-FGF23 antibodies	See table 1.2
Hereditary hypophosphatemic rickets with hypercalciuria	Loss-of-function mutation of *SLC34A3*: encodes renal sodium-phosphate co-transporter IIC	AR	241530	Differs from other types of hyphosphatemic rickets in that $1,25_2$(OH) is high; nephrolitiasis	Phosphate	[33]
Rickets/osteomalacia secondary to inhibited mineralization						
Hypophosphatasia	Loss-of-function mutations of ALPL (alkaline phosphatase)	AR, AD	241500 146300 241510	Extremely broad spectrum: from perinatal lethality to mild dental abnormalities in adults	Asfosfatse alpha	[34-36]
Aluminium, fluoride, and bisphosphonate (1st generation toxicities)	Aluminium: CKD, antiacids. Etidronate.	----	----	Current rare causes: drug indications and dyalisis technology have changed		[37-39]

The evaluation of a child or adult with clinical signs of rickets/osteomalacia requires a careful history with special attention given to calcium, phosphorus and vitamin D dietary intake, sun exposure, surgeries, medication and family history. Radiographic are especially informative in children, due to the presence of rickets, while in adults, X-rays are normally not as distinctive except in advanced stages when pseudofractures are evident. The most frequent radiographic finding in adults with osteomalacia is decreased bone density [17]. While bone mineral density (BMD), usually assessed by dual-energy X-ray absorptiometry (DEXA), is oftentimes reduced in adults with osteomalacia [40], low BMD is a relatively insensitive measure of the degree of osteomalacia.

Laboratory evaluation can be very useful to determine the etiology of rickets/osteomalacia. A diagnostic algorithm based on blood and urinary biochemistries, partially adapted from [41], is displayed in Figure 1.4. In rare cases, in which clinical, radiographic, and biochemical examinations cannot provide a clear diagnosis, the presence of osteomalacia can be corroborated through the analysis of a bone biopsy [18]. Histological assessment of osteomalacic bone and 2-D histomorphometry are described in sections 3.1.6-3.18.

Importantly, consideration must be given to other disorders that cause weakness, bone pain, insufficiency fractures and altered radiologic features such as primary hyperparathyroidism, osteoporosis, multiple myeloma, Paget's disease, and skeletal dysplasias. Specific treatments are tailored to each patient according to the severity and etiology of the disorder (Table 1.1). The therapeutic approach to FGF23-mediated hypophophatemic rickets is further discussed in the Discussion.

1.4 Skeletal dysplasias

Skeletal dysplasia is the term employed to refer to genetic disorders characterized by abnormal development, growth, and maintenance of the bone and cartilage [42]. Clinically, the most common manifestations are disproportionate short stature and skeletal malformations, although the clinical spectrum is extremely broad and often associated with abnormalities in non-skeletal systems. The severity of these disorders is also very variable and can range from neonatal lethality, to minor disabilities discovered incidentally during adulthood [42]. Although the incidence of each individual disorder is rare (the most common are achondroplasia and osteogensis imperfecta with an approximate frequency of 1/20,000 live births [43,44]), collectively the incidence of skeletal dysplasias is not negligible, with an estimated frequency of 1:5000 live births [45].

The classification of this large group of heterogeneous disorders has proven to be an extremely challenging task. The attempts to create nosology of skeletal dysplasias started in the 1970's and initially relied mostly on radiographic and clinical findings [46]. However, the recent advances in sequencing technologies have facilitated tremendously the elucidation of the molecular etiology of many skeletal dysplasias and currently many of these conditions are now grouped according to the genetic defect and/or altered metabolic/signaling pathway [47]. The discovery of causative genes and defective proteins has had a significant impact in the diagnosis, prognosis, management, and genetic counseling for patients with these conditions,

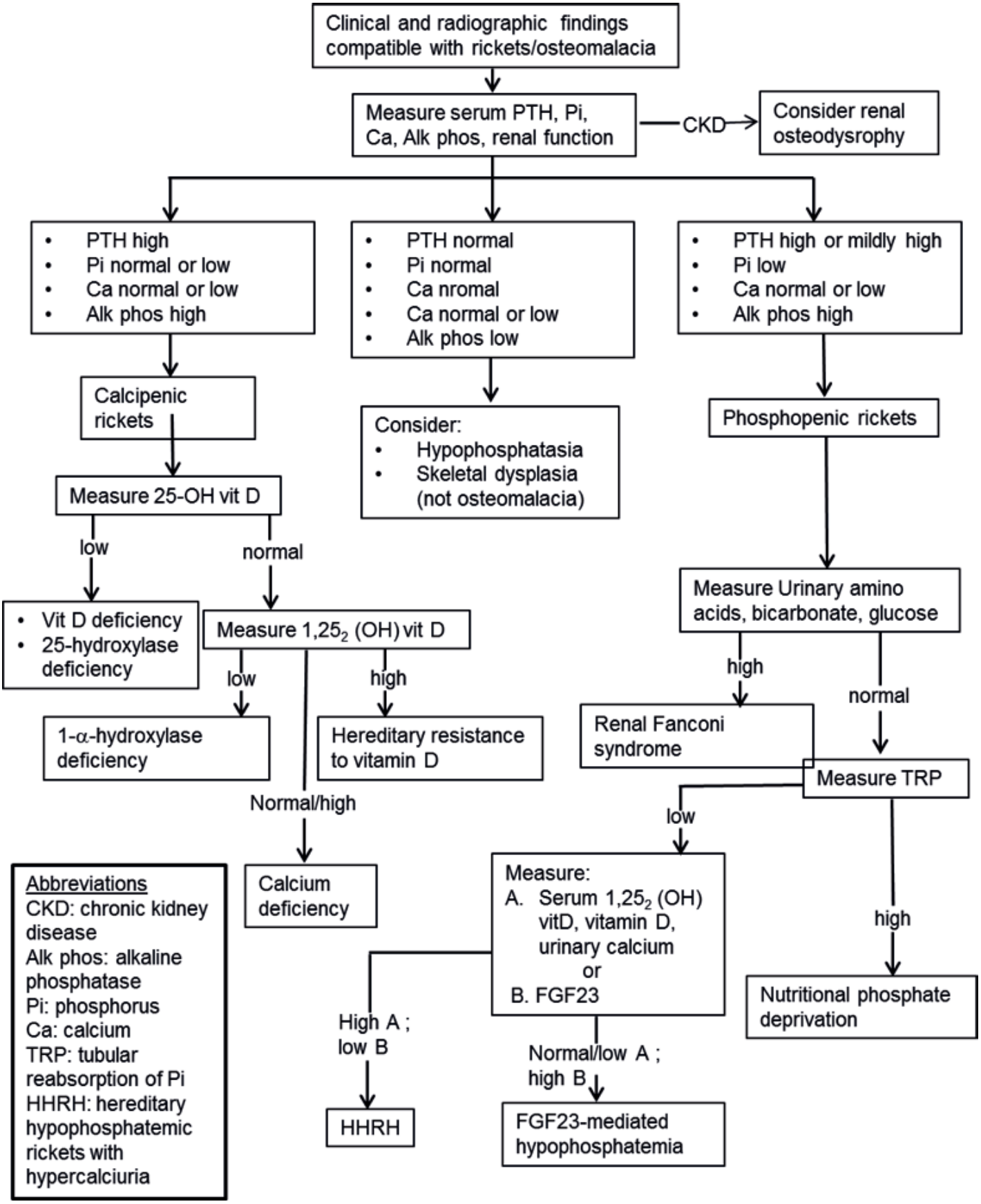

Figure 1.4 Biochemical diagnostic algorithm for rickets/osteomalacia. Algorithm partially adapted from [41].

in addition to the development of new drugs that specifically target the affected pathway [48]. The International Society of Skeletal Dysplasias meets periodically to update the nomenclature and classifications on these disorders in an effort to integrate the advances in the molecular aspects of this field. The last edition of the Nosology and Classification of Genetic Skeletal Disorders was updated in 2015 and listed 436 conditions divided into 42 groups following clinical, radiographic and molecular criteria offering a master list of the genetic disorders of the skeleton [49].

The skeletal dysplasia associated with nevoid syndromes has not been included in the Nosology yet.

1.5 Cutaneous Skeletal Hypophosphatemia Syndrome (CSHS)

1.5.1 CSHS: a mosaic disorder of the skin and bone

Hypophosphatemic rickets and mosaic dysplastic bone lesions are two extra-cutaneous abnormalities that have been reported in association with EN, CMN and PPK [50-53]. Given that these mineral alterations and skeletal findings can occur together with different types of nevoid disorders in a syndromic fashion, we coined the term Cutaneous Skeletal Hypophosphatemia Syndrome (CSHS). Elevated FGF23, a bone-derived hormone, has been detected in all patients with CSHS in whom blood FGF23 has been measured [50,52,54,55]. An in-depth review of the biology of FGF23 is displayed in section 1.7.

While elevations in FGF23 are consistently seen in CSHS, the tissue source of the pathologically elevated FGF23 remains to be determined. Operating under the assumption that skin lesions are the source of the FGF23, removal of skin lesions has been advocated as a potential treatment for the hypophosphatemia of CSHS [56]. However, the efficacy of this approach has not been systematically investigated. In addition, the clinical spectrum and natural history of CSHS remains poorly described due in part to its rarity and diagnostic uncertainties in previously reported cases. Purpose focus of this thesis is to answer these important unknowns.

1.5.2 RAS mutations cause CSHS

Taking advantage of whole exome sequencing approaches, somatic activating mutations in *RAS* genes were identified in 2012 as the predominant molecular etiology of epidermal and melanocytic nevi, both as isolated lesions or as part of syndromic forms [57-60]. In regards to CSHS, a somatic *HRAS* mutation in codon 13 was identified in the nevoid skin from a woman with NS with concomitant hypophosphatemic rickets and skeletal dysplasia [53,57].

To further investigate the molecular etiology of CSHS, our group at the National Institute of Dental and Craniofacial Research (NIDCR) in collaboration with Dr. Keith Choate's group in the Dermatology department at Yale University School of Medicine, analyzed affected tissue in 5 subjects with CSHS (see Annex II) [61]. Exome sequencing of the nevi and blood lead in all cases to the identification of somatic activating mutations of *HRAS* or *NRAS* in the affected skin, which were absent in the blood. Further, sequencing of dysplastic bone specimens in two of the subjects identified the same mutation that they harbored in the nevi.

The identification of activating *RAS* mutations in tissues derived from different germ layers (skin-ectoderm and bone-mesoderm) provided evidence that embryonic mutations in a common progenitor of skin and bone lead to CSHS (Figure 1.5). In addition, these results suggested that other extracutaneous manifestations associated with nevoid syndromes are likely due to the pleiotropic effects of *RAS* mutations acting in different tissues. In line with this, Avitan-Hersh et al. performed genetic testing on a boy with CSHS and a thymoma; sequencing of the nevus and the thymoma revealed an identical *HRAS* mutation that was not present in the blood [62]. Similarly, the presence of a somatic *KRAS* mutation in the nevus and in a cervical lipomatous tumor (mesodermal origin) in a child with another subtype of ENS has been recently reported [63]. Following this logic, the timing and location of the occurrence of the *RAS* mutation during embryonic development will determine the type, extent and distribution of mutated progeny cells in the body, and thus the spectrum of clinical phenotypes that characterize the different subtypes of ENS, including CSHS.

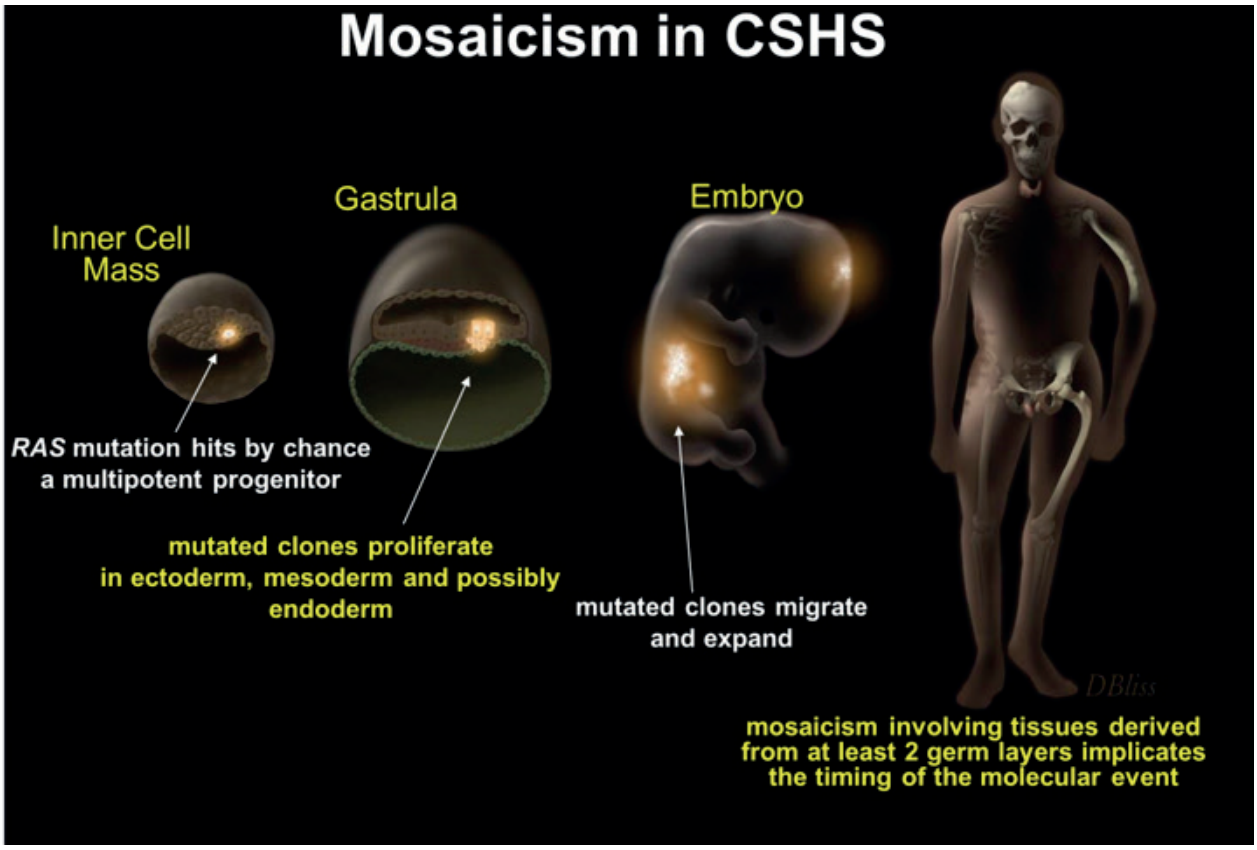

Figure 1.5 Illustration depicting speculative mechanisms of CSHS's embryonal development. Interestingly, this illustration by Donald Bliss (NIH Division of Medical Arts) was created for our lab to represent the stages of embryonal development in McCune Albright syndrome, a disorder that presents several overlapping features with CSHS, and reflects the commonality in the developmental pathophysiology of somatic mosaic disorders, in general.

1.6 RAS proteins

RAS proteins are key signaling molecules involved in many cellular processes including cell growth, differentiation, and survival [64]. They respond to a number of extracellular ligands and activate several signaling pathways, including the well-known mitogen-activated protein kinase (MAPK) and the PI3K/Akt/mTOR pathways [65] (Figure 1.6, image extracted from [65]). RAS proteins are membrane-bound small GTPases (GTP: guanosine triphosphate) that switch to active and inactive conformations when bound to GTP and GDP (guanosine diphosphate), respectively [66]. Unlike other GTPases (e.g. Gs alpha) RAS proteins lack an efficient intrinsic GTP binding and GTPase activities and require external aid to efficiently activate the "on state" (through proteins known as guanine exchange factors), and the "off state" (via GTPase activator proteins like neurofibromin) [66,67] (Figure 1.7A, image extracted from [68]).

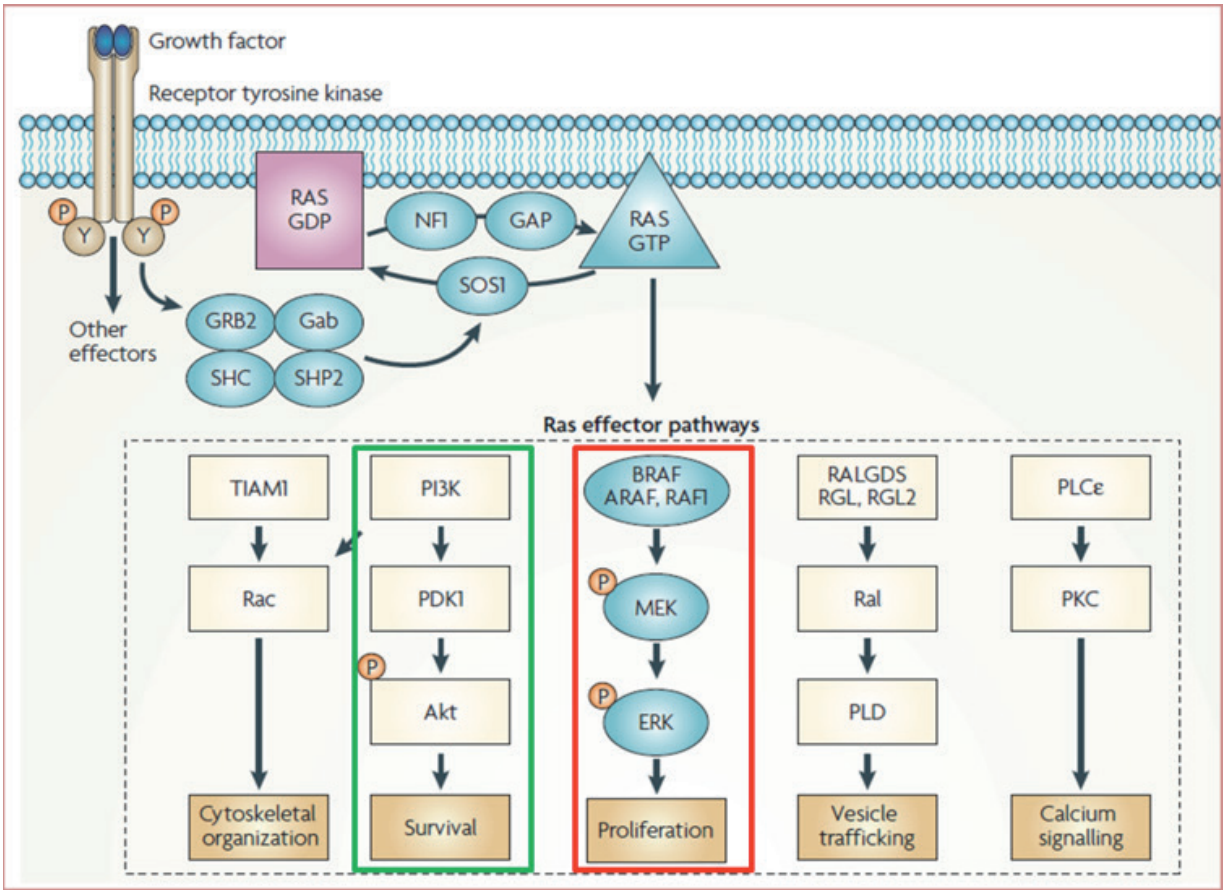

Figure 1.6 RAS-effector pathways. RAS responds to a great number of factors and activates a complex network of signaling pathways. The pathways displayed in this illustration are the most thoroughly studied. The RAS-RAF-MEK-ERK pathway (red rectangle), also known as the mitogen-activated protein kinases (MAPK) pathway, is the best characterized. This cascade culminates with the activation of transcriptional regulators that lead to the expression of proteins involved in cell cycle control. The PI3K-cascade (green rectangle) is also very well known, and has prominent role in cell survival as Akt activation, downstream of PI3K, inactivates proapoptotic proteins. Consistently, RAS hyperactivity as a consequence of activating mutations, can lead to excessive proliferation and illusion of apoptotic signals as observed in many cancers. Image adapted from [65].

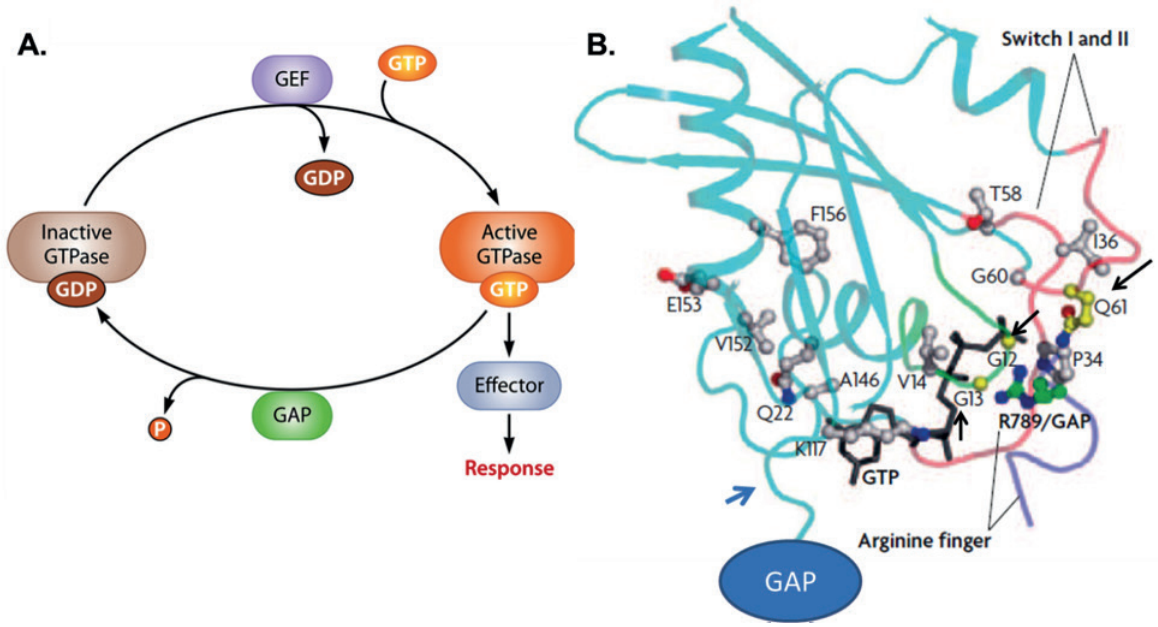

Figure 1.7 RAS regulatory cycle and structure. (A) RAS-related GTPases cycle between an active (GTP-bound) and inactive (GDP-bound) state (image adapted from [68]. GTPAse activator proteins (GAPs) markedly enhance RAS's GTPase activity facilitating RAS inactivation. Guanosine exchange factors (GEFs), on the other hand, stimulate guanine nucleotide dissociation from RAS. Given that in the cytosol there is a 10 fold abundance of GTP vs GDP, the active RAS–GTP conformation is favored from GEF's action. (B) RAS structure (image adapted from [65]. Amino acids that are altered by somatic mutations in human cancers, cutaneous nevi, and CSHS dysplastic bone lesions are represented by the yellow carbons and black arrows (glycine 12, glycine 13 and glutamine 61). White carbons represent the residues affected in germline RASopathies. The loops that are important in binding to effectors, switch I and switch II, are shown as pink ropes. The blue rope and blue arrow points to the arginine finger of GTPase-activating proteins which stimulates GTP hydrolysis.

The most relevant members of the RAS subfamily are HRAS, KRAS, and NRAS [65]. The respective genes are found on different chromosomes, but all three are highly homologous. In fact, the first 85 amino acids are identical. This 100% homologous region includes the all-important GTPase activity domain, to which amino acids 12, 13, and 61 are critical (Figure 1.8, image extracted from [65]). Amino acid substitutions in these codons lead to constitutively active RAS, and are found in approximately 30% of all human cancers [69]. These mutations are the ones that are found in most patients with epidermal and melanocytic nevi and their associated syndromes [57-60]. As previously discussed, it is presumed that these mutations would be lethal if transmitted in a germline fashion and survive only by mosaicism. An exception is Costello Syndrome, an extremely rare disorder frequently due to germline *HRAS* mutations in codon 12 [70]. Interestingly, Costello patients display cutaneous and skeletal abnormalities but not cutaneous nevi or hypophosphatemic rickets. Other developmental disorders due to germline mutations in the RAS-MAPK pathway, commonly known as RASopathies, are Noonan syndrome, Cardio-facial-cutaneous syndrome, LEOPARD syndrome, and neurofibromatosis type 1 [65]. In these other syndromes, mutations are typically located in codons other than 12, 13, or 61 (Figure 1.7B, adapted from [65]), or in other genes involved in the RAS-signaling pathway (e.g. neurofibromin in neurofibromatosis type 1). These mutations are presumed to exert a lower kinase activity than those found in cancer or congenital nevi, facilitating their viability as germline transmission.

At present, it is unclear what is the specific role of one RAS protein vs another in normal cellular function, although certain *RAS* mutations are found with greater frequency in certain

cancers, e.g. *KRAS* in pancreatic cancer, *HRAS* in bladder cancer, and *NRAS* in melanoma [69]. Consistent with the role of *NRAS* in pigmented lesions, *NRAS* mutations are the sole recurrent mutation found in CMN [71], whereas *HRAS* mutations are the predominant cause for EN [57,59]. *KRAS* and *NRAS* mutations have also been identified in EN and associated syndromes, but a clear genotype/phenotype correlation is lacking.

Importantly, the identification of activating *RAS* mutations in CSHS suggested that RAS hyperactivity was associated to increased FGF23 production.

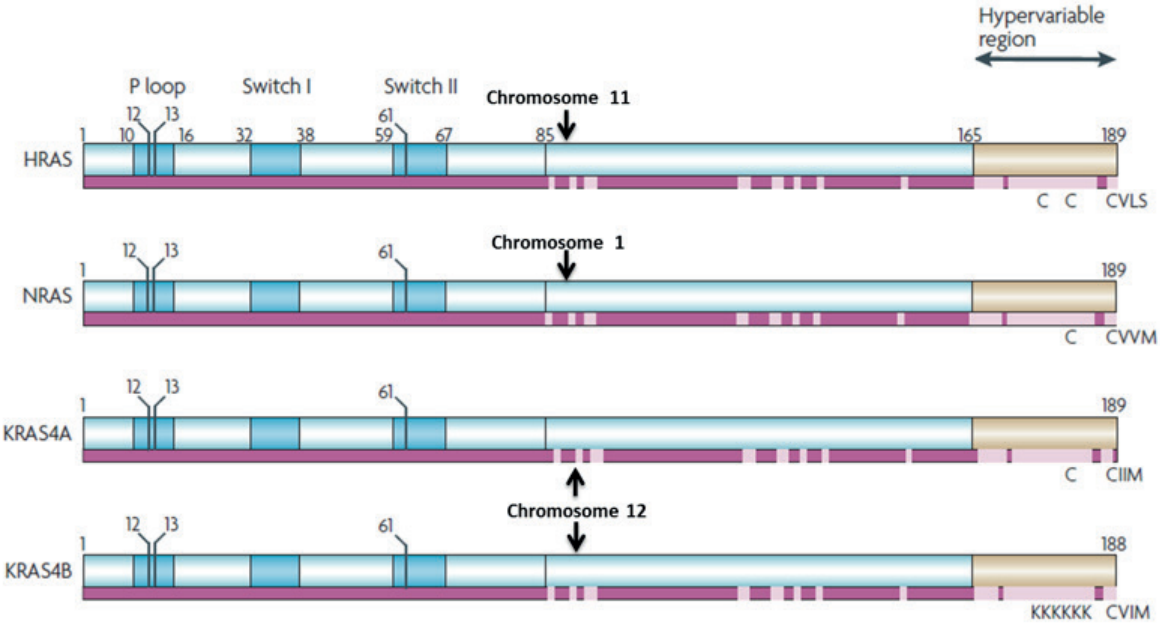

Figure 1.8 Amino acid sequences of the main RAS isoforms. HRAS, NRAS, KRAS4A and 4B (the latter are splice variants) are highly homologous throughout amino acids 1–165. The first 85 amino acids are identical in all four proteins and specify binding to GDP and GTP. This includes the P loop (phosphate-binding loop, amino acids 10–16), which binds GTP, and switch I (amino acids 32–38) and II (amino acids 59–67) which regulate binding to RAS regulators and effectors. The next 80 amino acids (85–165) show ~85–90% sequence identity. The C-terminal hypervariable domain specifies membrane localization through post-translational modifications. Image adapted from [65].

1.7 Fibroblast growth factor-23 (FGF23)

1.7.1 FGF23: a critical regulator of phosphate homeostasis

Phosphate, the most abundant form of phosphorus in the human body, is a crucial component for multiple biological processes including skeletal development and mineralization, energy transfer, intracellular signaling, and nucleic acid composition [72]. Its complex regulation depends predominantly on the interaction of the hormones calcitriol, parathyroid hormone (PTH), and other factors known as "phosphatonins", of which FGF23 is the best characterized (in fact the existence of any other phosphatonin is debatable) [73]. The existence of a circulating phosphaturic factor was initially proposed by Andrea Prader in 1959 [74]; he described the

relatively sudden onset of hypophosphatemic rickets in a girl, which resolved after the surgical resection of a benign mesenchymal tumor and postulated that the tumor secreted a factor that was responsible for the observed alterations in mineral homeostasis. The existence of a circulating phosphaturic factor was demonstrated years later by Meyer et al. in en elegent set of parabiosis experiments in *hyp* mice, the murine model for X-linked hypophosphatemic rickets (XLH) [75], and showed that a "rachitogenic" substance in the circulation of *hyp* mice was able to induce phosphaturia in the wild type (WT) animals when their circulatory systems were connected [76]. Eventually, in the year 2000, genetic testing performed in 4 families affected with autosomal dominant hypophosphatemic rickets (ADHR) identified missense mutations in a newly recognized member of the fibroblast growth factor (FGF) family, FGF23. This discovery suggested that FGF23 played a pivotal role in phosphate homeostasis. Shortly thereafter, abnormally high levels of serum FGF23 were detected in the circulation of other inherited disorders that featured hypophosphatemia (Table 1.2).
Corroborating Prader's hypothesis, elevated FGF23 was also observed in the circulation of patients with the acquired syndrome of tumor-induced osteomalacia (TIO, also known as oncogenic osteomalacia), a paraneoplastic syndrome characterized by acquired, severe hypophosphatemia, and resulting from the secretion of FGF23 from benign mesenchymal tumors, a.k.a., phosphaturic mesenchymal tumors (PMT) [77]. Consistent with the role of FGF23 in phosphate regulation, pathologically low levels of biologically active FGF23 are seen in familial tumoral calcinosis/hyperostosis hyperphosphatemic syndrome (FTC/HHS) (Table 1.2), an inherited disorder characterized by the opposite findings seen in patients with FGF23 excess: increased renal phosphate reabsorption, hyperphosphatemia, low 1,25-dihydroxi vitamin D, and and an elevated calcium x phosphate product [78].

1.7.2 FGF23: gene, protein, and tissue expression profile

FGF23 was initially identified in the year 2000 through positional cloning and related to other members of the FGF family through structural analysis [79]. The human gene, which is located on chromosome 12p13, translates into a 251 amino-acid protein, with a 24-amino acid signal peptide, and is highly conserved in mammals [80]. FGF23's N-terminal domain is homologous to other FGF family members, whereas the C-terminus is unique. The domains are separated by a consensus proteolytic cleavage site putatively recognized by subtilisin-like pro-protein convertases (SPC), which are considered to be responsible for FGF23 degradation [80] (Figure 1.9); cleavage is considered to inactivate FGF23.

While the hypothalamus was the site in which FGF23 gene transcription was originally detected [79], subsequent studies on FD and other skeletal disorders demonstrated that the bone was the physiological source of the hormone [81-83]. Elevated FGF23 and concomitant renal phosphate wasting had been observed in correlation with skeletal disease burden in patients with MAS [84], and subsequently, *in situ* hybridization studies revealed that both FD tissue and normal bone cells were the source of FGF23 [83]. The bone has also been identified by *in vivo* [81] and *in vitro* [82] studies as the tissue with the most significant *FGF23* expression.

Table 1.2 Inherited disorders with altered FGF23 production

Disorder	Gene	Inheritance	OMIM#	Phenotype	Ref.
Inherited disorders of FGF23 excess					
XLH	Loss-of function mutations *PHEX*	X-linked dominant	#307800	Hypophosphatemic rickets; early onset, dental abscesses, enthesopathies	[85]
ADHR	Gain-of-function mutations *FGF23*	Autosomal dominant	#193100	Hypophosphatemic rickets, variable age of rachitic onset; triggered by↓ iron	[86]
ARHR1	Loss-of-function mutations *DMP1*	Autosomal recessive	#241520	Hypophosphatemic rickets, early onset	[87]
ARHR2	Loss-of-function mutations *ENNP1*	Autosomal recessive	#613312	Hypophosphatemic rickets; cardiovascular anomalies, dental abnormalities	[88]
OGD	Gain-of-function mutations *FGFR1*	Autosomal dominant	#166250	Hypophospahtemic rickets, dwarfism, craniosynostoses, lucent bone lesions	[89]
Raine Syndrome	*Loss-of-function mutations FAM20C*	Autosomal recessive	#259775	Osteosclerosis, hypophosphatemia, dental abnormalities	[90]
Inherited disorders of FGF23 deficiency					
FTC/HHS	Loss of function mutations *GALNT3 FGF23 KLOTHO*	Autosomal recessive	#601756 #605380 #604824	Early onset hyperphosphatemia, cortical tibial thickening, ectopic calcifications, dental abnormalites	[91-93]

Abbreviations: FGF23: Fibroblast growth factor 23; XLH: X-linked hypophosphatemic rickets; PHEX: ADHR: autosomal dominant hypophosphatemic rickets; ARHR: autosomal recessivehypophosphatemic rickets; DMP-1: dentin matrix protein 1; ENPP1: ectonucleotide pyrophosphatase/phosphodiesterase 1; OGD: osteoglophonic dysplasia; FGFR1: fibroblast growth factor 1; FAM20C: family with sequence similarity 20 member C; FTC: familial tumoral calcinosis; HHS: hyperostosis hyperphosphatemic syndrome; GALNT3: UDP-N-acetyl-α-D-galactosamine:polypeptide N-acetylga-lactosaminyltransferase 3.

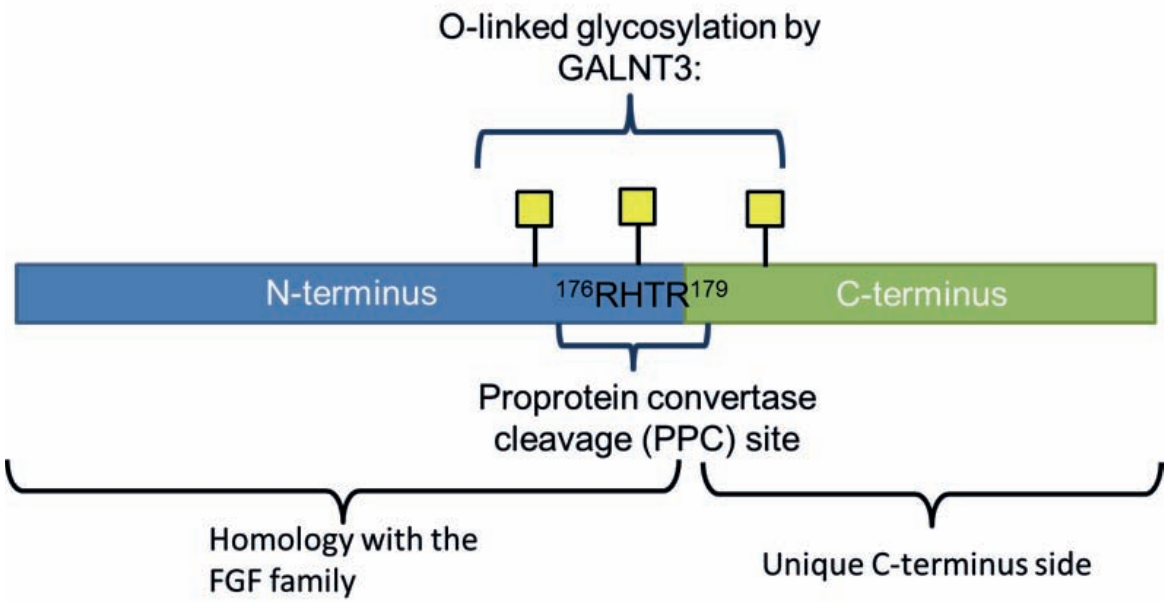

Figure 1.9 FGF23 protein structure. FGF23 is a 251 amino acid protein with a N-terminus that exhibits homology to the FGF family, and a unique C-terminus side. Both sides are separated by a proteolytic cleavage site defined by a R-X-X-R motif in position 179-179. There is evidence that FGF23 undergoes important posttranslational modifications such as o-glycosilation on threonine/serine residues (yellow squares), including the threonine at the cleavage site, by the enzyme N-acetylgalactosaminyltransferase 3 (GALNT3). O-glycosylation appears to confer the protein protection from cleavage and subsequent inactivation. Cleavage appears to be executed by pro-protein convertases, such as furin, which recognize R-X-X-R motifs. Loss-of-function GALNT3C mutations lead to familial tumoral calcinosis, a disorder in which excessive FGF23 inactivation causes hyperphosphatemia and tumoral calcinosis. The opposite takes place when FGF23's cleavage site becomes mutated as occurs in autosomal dominant hypophosphatemic rickets, characterized by FGF23-mediated hypophosphatemia secondary to ineffective FGF23 inactivation.

1.7.3 FGF23: mechanism of action

The kidney is considered FGF23's main tissue target. FGF23 signaling induces transcriptional and translational inhibition of genes expressed in the renal proximal tubule that encode proteins important in phosphate uptake, namely sodium/phosphate co-transporters 2a/2c (NaPi2a, NaPi2c), and 1-α-hydroxylase [80,94]. These proteins are critical for renal phosphate reabsorption and vitamin D conversion to 1,25-dihyroxyvitamin D, respectively. In addition, FGF23 increases renal CYP24A1 expression, leading to higher levels of 25-hydroxyvitamin D 24-hydroxylase, an enzyme that metabolizes 25-hydroxy vitamin D and 1,25-dihydroxyvitamin D [95]. Phosphaturia, due to decreased transcription and translation of NaPi2a, NaPi2c, and impaired phosphate reabsorption in the gut, due to decreased 1,25-dihyroxyvitamin D, occur as a result of these changes, ultimately leading to decreased blood phosphate levels.

FGF23 exerts its renal actions by binding to fibroblast growth factor receptors (FGFR). Studies have shown that in the kidney FGF23 signaling is mediated primarily through FGFR1 (IIIc), and to a lesser extent FGFR4 and FGFR3 [96-98]. FGF23's tissue specficity is facilitated by the presence in the kidney of the FGF23 co-receptor α-Klotho, a molecule that provides FGF23 binding affinity to specific FGFRs [98]. An illustrative image of FGF23's renal actions is shown in Figure 1.10 (image extracted from [99]). Other tissues in which α-Klotho are expressed

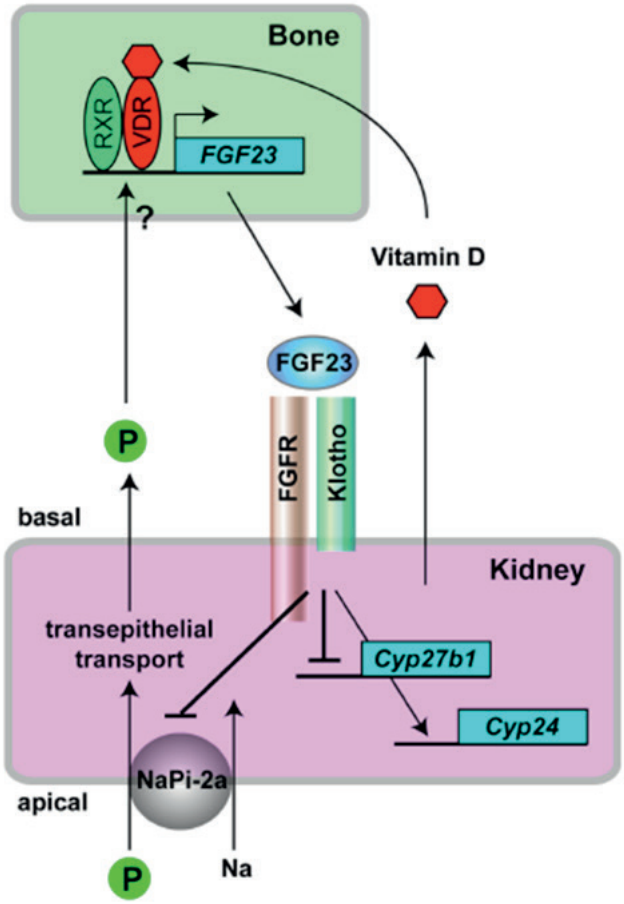

Figure 1.10 FGF23 mechanism of action. FGF23 is secreted from bone cells in response to increases in blood phosphate and 1,25-dihydroxivitamin D3 (vitamin D in this image). The phosphate sensing mechanism is yet to be determined, while 1,25-dihydroxivitamin D3 binds to the vitamin D receptor (VDR) to stimulate FGF23 expression. FGF23 is secreted into the bloodstream and targets the renal proximal tubule where it binds to fibroblast growth factor receptors (FGFR)1, 4 and 3 in the presence of co-receptor α-Klotho. Phosphaturic actions derived from this binding are partially due to the suppression of SCL17A1 and SCL17A3 which encode the sodium-phosphate co-transporters responsible for renal phosphate reabsorption, Napi-2A and 2c respectively. In addition, FGF23 blocks vitamin D actions by upregulating CYP24A1, which encodes the vitamin D-degrading enzyme, 25-hyroxyvitamin D 24-hydroxylase, and by suppressing the expression of CYP27b1, which encodes 1-alpha hydroxylase, the enzyme that converts 25-hydroxyvitamin D into 1,25-dihydroxivitamin D3. Image adapted from [99].

include the parathyroid glands [98], the choroid plexus [100], and the pituitary glands [101]. However, the specific biological functions of FGF23 outside the kidney have not been well defined. *In vivo* [102] and *in vitro* [103] models have suggested a direct inhibitory effect of FGF23 on PTH production, however these findings are not supported in the clinical setting; PTH is not suppressed in disorders of FGF23 excess, such as renal failure and TIO [104]. In addition, to date no pituitary alterations have been associated with disorders of FGF23.

1.7.4 FGF23: regulation

FGF23 regulation is complex and not completely understood. There is evidence supporting phosphate and calcitriol as part of a classic endocrine regulatory feedback loop in FGF23 production. Serum FGF23 positively correlates with dietary phosphorus intake and subsequent increased renal phosphate excretion in humans [105,106]. Phosphate's stimulating effects on FGF23 have also been confirmed in murine and *in vitro* models [107,108]. Nonetheless, the mechanism by which cells sense extracellular phosphate concentration remains to be elucidated. Similarly, the administration of exogenous calcitriol has shown to stimulate FGF23 production [109,110]. The vitamin D receptor (VDR) presumably mediates the effect of calcitriol on FGF23 transcription [95,110]. Less clear are the effects of PTH on FGF23 regulation. Elevated FGF23 is observed in certain disorders of PTH or PTH-related signaling, such as FD

or Jansen's metaphyseal dysplasia, in which PTH downstream signaling pathways (via cyclic adenosine monophosphate) are overactive [83,111]. However, in hyperparathyroidism data have not been concordant across studies [112,113]. Calcium has also been implicated as an independent regulator of FGF23 in studies on hyperparathyroidism [114,115]. Additional studies are needed to clarify the role of calcium in FGF23 regulation.

Iron has also been demonstrated to be involved in the regulation of FGF23 [116]. ADHR provided the first hints to the potential implication of iron in FGF23 regulation, when it was noted that the development of hypophosphatemia often occurs during periods of decreased iron storage (e.g. menarchy) [86]. Ferropenia has been shown to induce FGF23 production in ADHR subjects and normal controls, but in healthy controls hypophosphatemia is prevented by the proteolytic inactivation of FGF23, as demonstrated by increased C-terminal FGF23 fragments in their serum [117]. In contrast, individuals with ADHR have a resistance to appropriate hormonal degradation due to mutations in *FGF23*'s proteolytic cleavage site. These findings have been replicated in both *in vivo* and *in vitro* models [118]. Mechanistically, it has been shown that the hypoxia inducible factor-1-α (HIF1α) pathway is involved in the alterations of FGF23 metabolism in ADHR.

Additional genes implicated in FGF23 regulation are those identified in other monogenic forms of FGF23-mediated hypophosphatemic rickets such as: phosphate regulating endopeptidase homolog X-Linked (*PHEX*), dentin matrix protein 1(*DMP1*), ectonucleotide pyrophosphatase/ phosphodiesterase 1(*ENPP*1), family with sequence similarity 20-member C (*FAM20C*), and fibroblast growth factor 1(FGFR1) (Table 1.2). However, the specific mechanisms by which the proteins they encode are involved in FGF23 production remains unclear. Novel data indicate that FAM20C, a Golgi secretory kinase, may promote FGF23 degradation through phosphorylation [119], and may also play an indirect role through transcriptional control of *DMP1*[120]. In the case of FGFR1, recent studies on bone-like cell lines and murine models have shown that activation of its pathway stimulates *FGF23* expression [121,122]. Correspondingly, overexpression of *Fgf2,* and *Fgfr1* ligand present in the extracellular bone matrix, results in FGF23 induction in mice, implying the presence of an autocrine/paracrine FGF23 regulatory system [123].

FGF23 post-translational modifications, predominantly glycosylation, add an additional layer of complexity to its regulation. O-glycosylation of specific threonine residues by the enzyme UDP-N-acetyl-α-D-galactosamine polypeptide N-acetylga-lactosaminyltransferase (GALNT3) [93], confers the protein protection from cleavage. The consequences of O-glycosylation defects are seen in FTC, a recessive disorder caused in the vast majority of cases by GALNT3 mutations, which lead to uncontrolled FGF23 fragmentation and subsequent hyperphosphatemia [93]. Opposite processing abnormalities to those seen in FTC occur in ADHR, in which mutations in FGF23 at the proprotein cleavage site impair SPC's physiological proteolytic activity. Taken together, *GALNT3* mutations and HIFα-mediated processing, identify and important role for posttranslational modifications of FGF23 in maintainence of functional and intact FGF23.

Of note, FGF23 regulation is also altered in patients with chronic kidney disease (CKD). FGF23 levels start to increase in early CKD stages, prior to phosphate elevation or PTH alterations [124]. In advanced stages, FGF23 appears much higher than in any other disorder. It remains largely unknown what triggers the intial increase in FGF23 and extreme levels attained in renal insufficiency [125].

1.7.5 A role for RAS in the regulation of FGF23

RAS proteins arose as new potential players in FGF23's intricate biology after the identification of somatic *RAS* mutations in the dysplastic bone and skin of subjects with CSHS [61], yet the link between hyperactive RAS and FGF23, and the tissue source responsible for FGF23 overproduction in CSHS remained unclear. The search for the answers of these important and evolving questions in human physiology is part of the main focus of what follows.

2. THESIS JUSTIFICATION, HYPOTHESES, AND OBJECTIVES

2.1 Thesis Justification

It is important to study CSHS for the following reasons:

1. CSHS is a recently described syndrome that has not been adequately characterized. There is a need to define the clinical spectrum and natural history of the disease, so as to: a.) determine the most effective therapeutic options for treating the hypophosphatemia; b.) define the tumorigenic potential of affected tissues; c.) characterize the natural history of the skeletal disease. This knowledge is critical for patients and the physcians caring for them.

2. The study of CSHS offers the opportunity to broaden the existing knowledge on FGF23's physiology. FGF23 is a critical hormone for phosphate and vitamin D homeostasis, yet its regulation remains poorly understood. The identification of *RAS* mutations as the genetic cause of CSHS, a disease characterized by FGF23 excess, points to a role of RAS signaling in FGF23 regulation. However, the tissue source of FGF23 excess in CSHS and RAS' specific involvement in FGF23 production are still unknown and await investigation.

3. CSHS provides an excelllent biological model to investigate the effects of RAS hyperactivity. CSHS is one of the few known multi-systemic mosaic syndromes that arise from potent somatic mutations in genes key in cellular signaling pathways. It is accepted that these mutations are embryonically lethal if inherited through germline transmission and can only survive in the mosaic state. Hence, the opportunity to study the developmental effects of these mutations in different tissues only occurs in the setting of these rare mosaic disorders. While *RAS* mutations have been identified in many acquired neoplasms, in most of those tumors *RAS* is only one of many etiologic mutant genes present. In contrast, in CSHS patients are more likely to harbor solely the initial *RAS* mutation. Therefore, the examination of affected tissues from CSHS patients delivers unique and non-confounding information on the impact of RAS hyperactivity in different organs.

2.2 Thesis Hypotheses

1. We hypothesize that a thorough phenotypic assessment of patients with CSHS, and a careful analysis of all potential reported cases of CSHS, will provide important clinical and pathophysiologic information of this rare syndrome, resulting in a valuable tool for patients and physicians that encounter this rare disorder in their practice.

2. We hypothesize that dysplastic bone is the source of FGF23 overproduction in CSHS. Given that bone is the physiological source of FGF23, and that a mosaic skeletal dysplasia is observed in all CSHS patients, it is likely that mutated bone cells are responsible for FGF23 excess. From this it follows that removal of skin lesions is probably not effective in treating the phosphate wasting in CSHS.

3. We hypothesize that exploring the effects of activating *RAS* mutations in the bone, through the generation of *in vivo* and *in vitro* models, will inform of the physiopathology of dysplastic bone formation in CSHS and the potential effects of RAS hyperactivity on FGF23 production in the bone.

2.3 Thesis Objectives

The main objectives of the following work are:

1. To perform a comprehensive analysis of the clinical spectrum and natural history of CSHS through the study of a cohort of subjects and a comprehensive review of all reported cases of CSHS.

2. To identify the tissue source and physiopathology of FGF23 overproduction in CSHS through the analysis of nevoid skin, and the generation of suitable *in vitro* and *in vivo* models.

3. To investigate the effects of hyperactive RAS on dysplastic bone formation through analysis of bone specimens of CSHS patients and the generation of suitable *in vivo* models.

3. SUBJECTS, MATERIALS, AND METHODS

This section has been divided in two parts: the first displays the subjects and the methods used for the CSHS clinical characterization. The second shows the methods employed in the development of CSHS experimental models.

3.1 Subjects and methods for the clinical characterization of CSHS

3.1.1 Subjects

Four subjects with extensive congenital nevi, mosaic skeletal lesions and FGF23-mediated hypophosphatemic rickets underwent clinical phenotyping including history and physical exam, selected laboratory and imaging studies, photography, and a clinical multidisciplinary assessment at the NIH (National Institutes of Health) Clinical Center (Figure 3.1). They are identified as CSHS101, CSHS104-106. All participated in an NIH Institutional Review Board (IRB)-approved protocol and gave informed consent/assent and are referred in this thesis as the NIH cohort. In the case of CSHS104, the subject died a year and a half after her admission at NIH, but archival tissues, including bone, were obtained from her autopsy for investigation. Clinical records and radiographs of another subject with the same characteristics evaluated in another clinical center, CSHS102, were also reviewed. This subject provided written consent to a study protocol in her medical center.

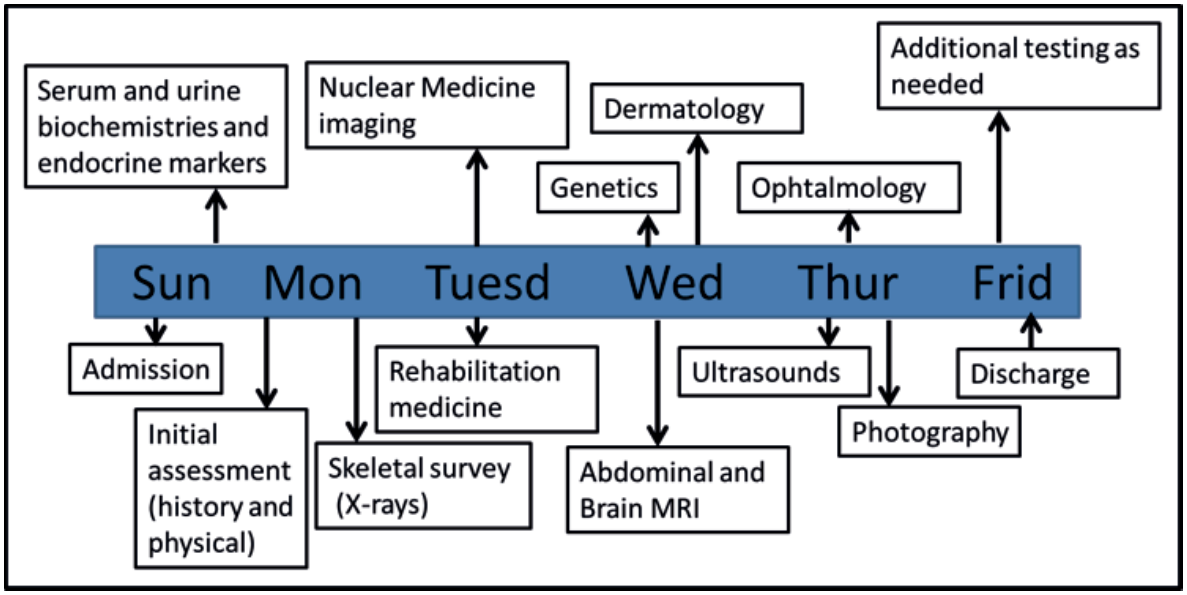

Figure 3.1 Schematic overview of the typical work-up schedule for CSHS subjects examined at the NIH clinical center.

NOTE I: Sequencing of the nevi and the blood was performed on all subjects and revealed activating *HRAS* or *NRAS* mutations in all cases [61,126]. Further, sequencing of dysplastic bone specimens was also performed on CSHS102 and CSHS104 identifying the same mutation found in the nevi. Although this sequencing data has been essential for the experimental design and conclusions drawn in this thesis, they will not be included in the main body of this thesis as most of that data was generated by collaborators at an outside institution (Yale School of Medicine).

NOTE II: The numbers used as subject identifiers in this thesis are identical to the numbers assigned to these patients in the publications associated to this work [61,126,127]. Our lab did not have direct contact or access to the clinical records of subject CSHS103, which is an additional CSHS patient presented in the earliest manuscript [61]. Therefore, CSHS103 has not been included as part of the CSHS cohort of this thesis.

3.1.2 History, Physical exam and multidisciplinary consultations (NIH cohort)

In addition to a detailed history and careful physical examination performed by the medical staff in our section (Section on Skeletal Disorders and Mineral Homeostasis), subjects were also evaluated in collaboration by the Dermatology, Genetics, Ophtalmology, Rehabilitation Medicine, and Dentistry departments in the NIH clinical center. Subject CSHS104 also underwent assessment by Hematology-Oncology due to the identification of bicytopenia in her blood tests (see section 4.1.5).

3.1.3 Imaging Studies

The NIH cohort underwent several imaging tests to determine the distribution, extension and characteristics of affected tissues in CSHS. All tests were performed and informed by the Radiology and Imaging Sciences Department at the NIH clinical center. For CSHS102, only upper and lower extremity radiographs performed elsewhere were available for review.

The following studies were performed:

- Thyroid ultrasound (US) (all subjects), abdominal US (all subjects), pelvic US (CSHS101, 104, 106) and testicular US (CSHS105): performed with a Logiq E9 imaging system (GE Healthcare, Chevy Chase, MD, USA).

- Abdominal and brain magnetic resonance imaging (MRI) (all subjects): T1 and T2 weighted images of the brain and abdomen were obtained in sagittal, axial and coronal views in a 3 or 1.5 Tesla Philips Achieva (Philips Healthcare, Baltimore, MD, USA). Slice widths ranged from 4-10 mm.

- Conventional radiographs (all subjects): Complete skeletal survey (cranial, upper extremities, thorax, spine, pelvis, lower extremities, hand and feet X rays was performed with CARESTREAM DRX-Evolution Plus (Carestream Health, Rochester, NY, USA).

- DEXA (CSHS105): BMD was assessed by DEXA (Hologic, Bedford, MA, USA) in subject CSHS105. Percent coefficient of variation from precision testing of each site was as follows: lumbar spine (1.1%), total body (1.1%), 1/3 distal radius (1.6%), femoral neck (1.8%), and total hip (0.9%). To normalize for the variation in age and gender, Z-scores were calculated using published normative databases for the adolescent [128]. Only subject CSHS105 underwent DEXA because he had undergone this test

prior to admission at the NIH revealing a markedly low BMD. DEXA was not performed in the other subjects as BMD does not appear to correlate well with the degree of osteomalacia [129].

- Octreo-SPECT/CT scan (CSHS101, 104, and 105): An octreotide scan, or octreoscan, is based on the detection of gamma-rays emitted by areas of indium-111(In^{111})-octreotide uptake after its exogenous administration. It is a diagnostic test in nuclear medicine typically employed in the detection of neuroendocrine tumors due to the abundance of somatostatin receptors in their surface [130]. The signal emitted by the In^{111}-octreotide, which is a radiolabeled somatostatin analog, is captured by gamma-cameras and can be transformed into 2-dimensional (scintigraphy) or 3-dimensional (single photon emission computed tomography (SPECT)) images facilitating the localization of these tumors. Because octreo-SPECT has proven useful in the localization of FGF23-secreting PMTs [131], we speculated that it may be useful in identifying FGF23-secreting tissue in CSHS patients. Subjects were administered a weight-based intravenous dose of In^{111}-octreotide or In^{111}-pentreotide (an octreotide conjugate) and were imaged 24 hours after administration with a Precedence 16 Slice SPECT/CT system (Philips Healthcare, Baltimore, MD, USA). Concomitant to the 24-hour SPECT scan, an X-ray computed tomography (CT) incorporated in the same equipment was performed to obtain precise anatomic localization of the radiotracer uptake, and to correct for attenuation (i.e. the loss of signal detection due to soft tissue artifacts).

- 18F-Sodium Fluoride ($(Na^{18}F)$ PET/CT bone scan (CSHS106): Because the octreoscans performed on CSHS101, 104 and 105 did not reveal potential FGF23-secreting tissues (see Result section 4.1.4.5), this technique was abandoned, and in CSHS106, the most recent subject to enroll, we opted instead to use a $Na^{18}F$ Positron Emission Tomography (PET)/CT to study skeletal metabolic activity in CSHS. PET, similarly to SPECT, is a nuclear medicine imaging technique that detects the gamma-rays emitted by a radiotracer introduced into the body. The $Na^{18}F$ radiotracer differs from In^{111}-octreotide in that the $Na^{18}F$ is not taken up by tissues expressing somatostatin receptors but binds instead to the bone to areas with elevated osteogenic activity [132]. For that reason, it is used in the detection of bone metastasisas well as metabolic bone diseases [133]. $Na^{18}F$ also appears to have more advantageous bone kinetics than the classical 99-technetium compounds offering greater special resolution and disease burden quantification [132]. The procedure consisted in the intravenous administration of a weight-based dose of $Na^{18}F$. One hour after the injection, PET acquisition and a non-contrast X-ray CT scan were co-registered in a Biograph mCT (Siemens Healthineers, Erlangen, Germany).

3.1.4 Laboratory tests

Spot urine and blood samples were collected in the NIH cohort after an overnight 12 hour fast the morning following admission. To evaluate the baseline status of the mineral parameters and to avoid the confounding effects of oral treatment for hypophosphatemia, patients were asked to stop phosphate supplements 48 hours prior to admission and calcitriol 4 days before. Drugs

were restarted after the first urine and blood samples were collected. Except for FGF23, all parameters were measured in the NIH clinical center Clinical Pathology Laboratory.

Blood tests

The following blood parameters were assessed:

- Routine cell blood count: blood was collected in ethylenediaminetetraacetic acid (EDTA)-coated tubes and blood cells were counted in a XN-3000-Hematology-Analyzer (Sysmex, Kobe, Japan).

- Routine biochemistries: potassium, sodium, chloride, creatinine, urea, liver function tests. Blood was collected in a lithium heparin-tube and analyzed in the Cobas 6000 Analyzer (Roche Diagnostics, Indianapolis, Indiana, USA).

- Blood Mineral Panel: including calcium, phosphorus, magnesium, alkaline phosphatase and albumin. Sample was collected in a lithium heparin-coated tube and ran in the Cobas 6000 Analyzer.

- Endocrine labs: because CSHS physiopathology appears similar to that of MAS, we ordered a similar endocrine panel to that one used in our routine evaluation of MAS patients [5].
  - PTH: blood was collected in an EDTA-coated tube and measured through an electrochemiluminescence immunoassay on a Cobas e601 analyzer (Roche Diagnostics, Indianapolis, IN, USA).
  - Thyroid stimulating hormone and thyroxine: blood was collected in a lithium-coated heparin tube and analyzed in a Cobas 6000 Analyzer.
  - 25-hydroxyvitamin D and 1,25-dihydroxvitamin D: blood was collected in serum separation tube and measured through a chemiluminescent immunoassay on a Liaison XL analyzer (Diasorin, Stillwater, MN, USA)
  - Growth hormone: blood was collected in a serum separator tube and measured through a chemiluminescent immunometric assay on an Immulite 2000 XPi analyzer (Siemens Healthineers, Malvern, PA, USA).
  - Follicle-stimulating hormone and luteinizing hormone (assessed in subjects CSHS101, 104 and 106): blood was collected in a serum separator tube and measured through a chemiluminescent immunometric assay on a Immulite 2000 XPi analyzer.
  - Estradiol (assessed in subjects CSHS101, 104 and 106): blood was collected in a serum separator tube and measured through an electrochemiluminescence immunoassay on a Cobas e601 analyzer.
  - FGF23 (intact hormone) (measured in the NIH cohort except CSHS104): for FGF23 determination, blood was collected in an EDTA-coated tube. FGF23 was measured in our laboratory. Plasma was separted from the buffy coat and erythrocytes by centrifuging the tubes for 10 minutes at 2000 rpm. Intact FGF23 was measured in the plasma through an enzyme-linked immunosorbent assay (ELISA) as per

manufacturer's instructions (Kainos, Tokyo, Japan). Normal ranges were extracted from the literature [72]. ELISA plates that were run in our laboratory were read with a Wallac 1420 Victor2 Microplate reader (Perkin Elmer, Waltham, MA, USA).

Urine tests

Spot urine was collected in an 8 ml tube without additives. The following urine parameters were measured:

- pH, presence of protein, nitrite, glucose, hemoglobin, leukocyte esterase, nitrites, bacteria, white and red blood cells in the urine: assessed in an Iris iQ200ELITE Analyzer (Beckman Coulter, Brea, CA, USA)
- Calcium, phosphate, creatinine: measured through chemiluminescence in a Dimension EXL with LM Integrated Chemistry System (Siemens Healthineers, Erlangen, Germany).

Tubular reabsorption of phosphate (TRP), which is defined as the fraction of phosphate in the glomerular filtrate that is reabsorbed in the renal tubules, was calculated with the following equation:

TRP (%) = 1-((urinary phosphate/plasma phosphate) x (plasma creatinine/urinary creatinine))

CSHS102's physicians sent us blood and urinary laboratory results including a mineral panel and FGF23. Total FGF23 (intact plus C-terminal fragments) was measured at the Mayo Clinic through an immunometric enzyme assay as previously described [134]. CSHS104 had also FGF23 measured in the Mayo Clinic with the same system.

3.1.5 Punch biopsies

Three mm punch biopsies of nevoid skin in subject CSHS101's abdomen and CSHS105's left forearm were performed in the Dermatology department. Affected skin was divided in 4 parts: one part was sent to Yale School of Medicine for whole exome sequencing [61], 2 parts were frozen for research purposes: one for FGF23 immunofluorescence [61], and the other one for determining FGF23 presence through a tissue ELISA (see section 3.1.9). The fourth part was fixed overnight in paraformaldehyde (PFA) at 4°C and subsequently embedded in paraffin (section 3.1.7).

CSHS104 did not undergo a skin biopsy during her admission at the NIH and unfortunately died a year and half after her admission due to a pericardial effusion of unclear etiology. However, her physicians sent us a series of frozen and formalin-fixed paraffin embedded (FFPE) tissue samples from her autopsy, including cutaneous and bone specimens.
CSHS106 did not undergo a skin biopsy at the NIH as she had recently had one extracted in an outside center for histologic and genetic evaluation [126].

3.1.6 Bone biopsy

A right iliac crest biopsy was performed for clinical purposes in subject CSHS105 at age 17 in an area that appeared dysplastic on imaging. The procedure was done under sedation with a coring device. Prior to the surgery, subject CSHS105 was administered tetracycline and demeclocycline per a standard labeling protocol consisting of: demeclocycline (150 mg four times a day) using a standard regimen of 3 days on antibiotic, 12 days off antibiotic, 3 days on antibiotic, and 4 days off antibiotic with the biopsy on the fifth day. The bone specimen was divided in three similar parts, one was embedded in methylmethacrylate (MMA) for histomorphometric and mineral evaluation (see section 3.1.7 and 3.1.8), another was embedded in paraffin for histological evaluation (see section 3.1.7), and the last part was immersed in sterile media for primary cell extraction and mutation testing (see section 3.1.10).

3.1.7 Histology

A part of the skin biopsies in subjects CSHS101 and CSHS105's were fixed in 4% PFA for 12-18 hours in 4°C. Subsequently the specimens underwent regular paraffin embedding [135].

Next, 5 μm sections of these formalin-fixed, paraffin-embedded (FFPE) skin blocks were obtained with a microtome and were stained with hematoxylin-eosin (H&E) following a standard protocol [135].

One of the bone pieces derived from subject CSHS105's iliac crest biopsy was fixed with 4% PFA for 24 hours at 4°C. Subsequently the sample was decalcified in 0.5 mM EDTA for 4 weeks at 4°C. After verifying that the bone was completely decalcified through X-ray imaging with a MX-20 X-ray radiography system (Faxitron, Tucson, AZ, US), the sample underwent paraffin-embedding, sectioning, and H&E staining as described above. The pattern of the collagen fibers of CSHS105's bone (lamellar vs woven bone) was determined by examining the section under polarized light in a Zeiss Axio Imager Z1 microscope (Zeiss, Oberkochen, Germany).

One of the other pieces of the bone biopsy was fixed in 70% ethanol overnight. Subsequently, it underwent MMA-embedding as previously described [136]. MMA-embedding is the preferred method for processing undecalcified bone because bone and MMA have similar hardness facilitating uniform sectioning. In MMA-processing, like in paraffin embedding, samples are first dehydrated by immersing them in progressively higher concentrations of ethanol. Subsequently, samples are infiltrated with MMA and incubated for 10-15 days to allow for MMA polymerization for the constitution of a block. A harder blade is needed to section MMA-embedded samples. The MMA-embedded bone biopsy was sectioned in 6 μm slices and was stained with Goldner's trichrome as previously described [136]. Goldner's trichrome is suitable for assessing histological features and mineralization status in undecalcified bone as it stains mineralized bone in green and osteoid in red while respecting cellular integrity (Figure 3.2; image extracted from [137]).

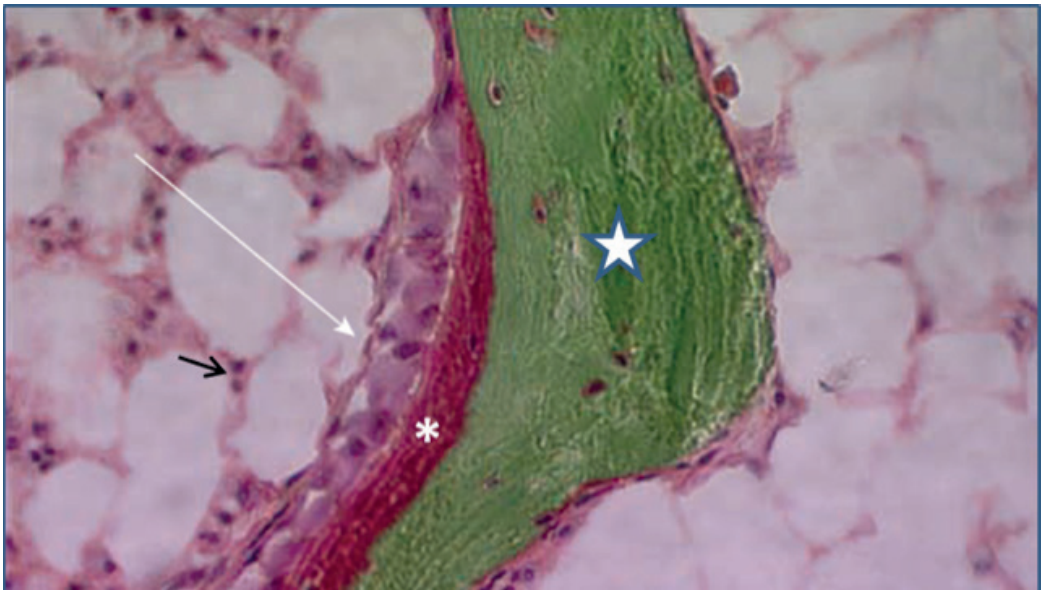

Figure 3.2 Example of a Goldner's trichrome stain. This stain is employed in methyl methacrylate-embedded undecalcified bone specimens to assess for mineralization status as it can distinguish calcified bone, which stains green (star), from unmineralized osteoid, which stains red (asterisk). The arrow, which is part of the original publication this image is adapted from, is pointing to a group of osteoblasts depositing newly formed bone. Cellular nuclei stain in darker blue (black arrow). Image adapted from [137].

In the case of CSHS104, because the bone samples received were decalcified and in FFPE blocks, sections were stained with Masson's trichrome as previously described [135]. Masson's trichrome can be used to assess mineralization in decalcified samples as it can differentiate bone that was mineralized prior to laboratory decalcification (stained in red) vs unmineralized collagen (stained in blue), albeit it is generally considered to be inferior to Goldner's stain for this purpose (Figure 3.3, image extracted from [100]).

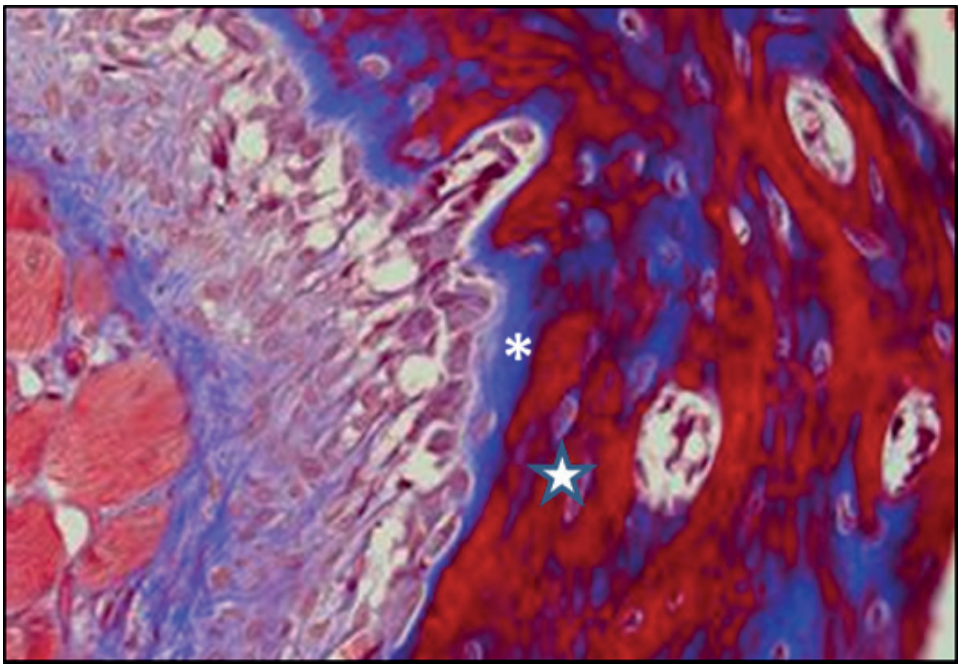

Figure 3.3 Example of a Masson's trichrome stain on decalcified bone. This stain allows to distinguish previously mineralized bone which stains in red (star) from unmineralized collagen which stains in blue (asterisk) in bone that has undergone decalcification. Image adapted from [100].

3.1.8 Bone Histomorphometry

Bone histomorphometry was assessed in CSHS105's MMA-embedded bone. In bone histomorphometry, undecalcified bone sections are examined to obtain quantitative information on structural parameters (e.g. number of trabeculae). Oftentimes, a labeling agent such as tetracycline is given prior to the biopsy. Tetracycline binds to newly formed bone at the bone/ osteoid interface and can be detected under a fluorescent microscope. If a second dose is given 11-14 days after the first dose, the amount of bone formed during that this time can be estimated by measuring the distance between the 2 fluorescent labels allowing for the evaluation of bone remodeling and calculation of bone kinetic indices (e.g. bone formation rate) (Figure 3.4, image extracted from [137]).

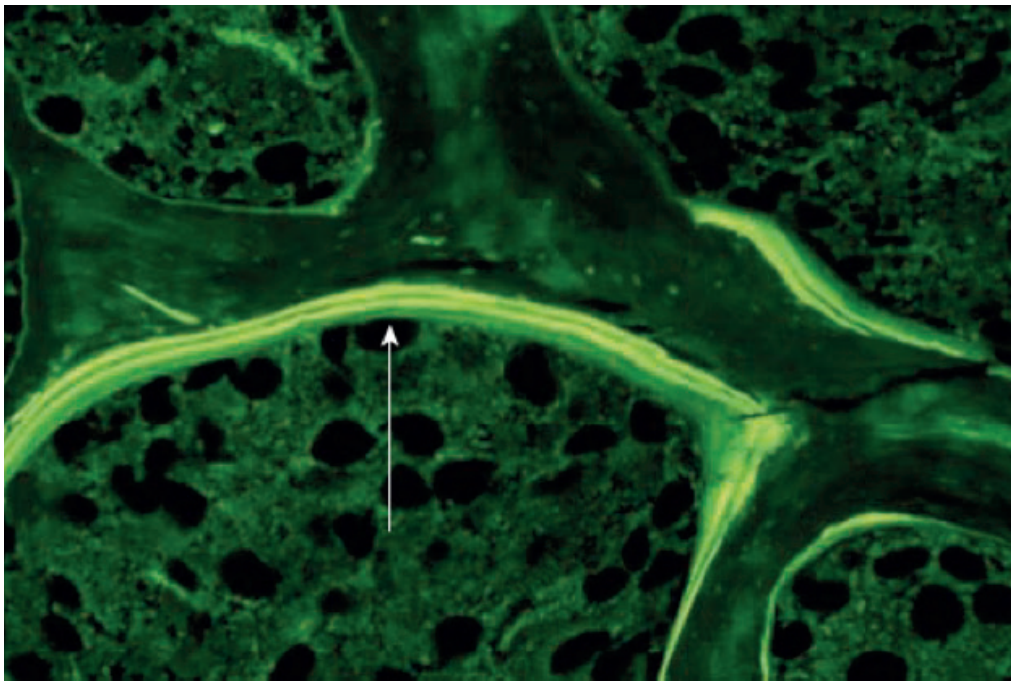

Figure 3.4 Double labeling of the bone with tetracycline. Because tetracycline attaches to sites of active mineralization and has fluorescent properties (arrow), when it is given in timed intervals before a bone biopsy, it allows to determine the rates of mineralization in that bone. Image adapted from [137].

Many parameters can be extrapolated. The following are some of the most frequently used indices:

Structural indices

- Cancellous bone volume: percent of mineralized bone per unit volume of the sample.
- Trabecular width: mean distance across individual trabeculae, given in μm.
- Trabecular number: number of trabecular plates per unit distance.
- Trabecular separation: mean distance between trabeculae, given in μm.
- Cortical width: average width of both inner and outer cortices, given in μm.
- Osteoid volume: percent of a given volume of bone tissue that consists of unmineralized bone (osteoid).

- Osteoid surface: percent of bone surface covered in osteoid.
- Osteoid thickness: mean thicknes of osteoid seams, given in μm.

Kinetic indices

- Mineralizing surface: percent of bone surface that shows a tetracycline label indicating active mineralization. It is calculated as the double-labeled surface plus one half of the single-labeled surface.
- Mineral apposition rate: measurement of the linear rate of new bone deposition. It is the mean distance between the double labels, divided by the time interval between them. Given in μm/day.
- Bone formation rate: amount of new bone formed in unit time per unit of bone surface and given in $\mu m^2/\mu m/day$.

Analysis of microstructural and kinetic indices in CSHS105's bone was performed using OsteoMeasure software (Osteometrics, Atlanta, GA, USA) and outcomes were expressed according to the American Society of Bone and Mineral Research standardized nomenclature [138]. To normalize for age and gender all values were transformed to Z-scores with normative databases derived from prior studies [139-142].

3.1.9 FGF23 tissue ELISA

Investigation of affected skin as a potential source of FGF23 in CSHS was done by measuring FGF23 in the supernatant of ground nevi from subjects CSHS101 and 105 as previously described [143]. Briefly, 100 mg of each nevoid sample was immersed in liquid nitrogen and pulverized with a mortar and pestle. The pulverized tissue was then homogenized with 800 μl of normal saline solution with 8 μl of proteinase inhibitor (EMD Millipore, Gibbstown, NJ, USA) with a glass tissue homogenizer. Samples were then centrifuged for 5 minutes at high speed (13000 rpm) and supernatants were collected for FGF23 analysis. One-hundred milligrams from two frozen PMTs and frozen thyroid tissue from patients that participated in NIH approved protocol, also underwent the same process to serve as positive and negative controls, respectively. An ELISA assay that measures total FGF23 was used for FGF23 quantification (Immutopics).

3.1.10 Mutation analysis in CSHS bone marrow stromal cells

Part of the CSHS105's bone biopsy was used to extract bone marrow stromal cells (BMSCs) to evaluate the presence of the *HRAS* G13R mutation; the mutation identified in his skin biopsy. First, the specimen was transformed into a single cell suspension. Subsequently, colonies of cells were generated in which each colony was derived from a single cell. Genomic DNA was extracted from each colony and underwenat mutation analysis. The isolation of single colony-derived strains is a technique that is particularly useful in the study of mosaic disorders as it allows to determine the mutation load in a given tissue and to study and compare the cellular properties of mutant vs WT cells [144].

3.1.10.1 Generation of hBMSC single cells suspension

Under sterile conditions, the piece from the bone biopsy that had been stored in sterile media, underwent gently scrapping with a scalpel into what we will refer to as "standard" BMSC growth medium consisting of: α-modified minimum essential medium (α-MEM), 2 mM L-glutamine, 100 U/ml penicillin, 100 µg/ml streptomycin sulfate (Invitrogen, Carlsbad, CA, USA), and 10% lot-selected fetal bovine serum (FBS) (Atlanta Biological, Flowery Branch, GA, USA). To obtain a single cell suspension of BMSCs, the marrow preparation was passed serially through a 16-gauge needle and 70 µm cell strainer (BD Biosciences, Franklin Lakes, NJ, USA).

3.1.10.2 Generation of single cell hBMCS colonies

Single cell colony isolation was performed as previously reported [144]. Initially, BMSCs were plated at a density of 2 x 10^3 cells/cm^2 into 150 mm tissue culture-treated petri dishes (BD Biosciences). The cells were cultured in standard growth medium at 37°C for 14 days without any media changes. After 14 days in culture, single colonies of 50 cells or greater were randomly selected and individually isolated. To ensure that the selected colonies were derived from only one cell, only colonies with a round morphology and obvious separation from surrounding colonies were chosen. Colonies were passaged by first attaching a cloning cylinder (Bel-Art Products, Wayne, NJ, USA) to the culture dish using sterile vacuum grease (Baxter Healthcare International, Deerfield, IL, USA) such that the cylinder fully surrounded an individual colony. Trypsin 0.05% with EDTA (Invitrogen) was then used to detach the cells, which were transferred to one well of a 6-well plate (BD Biosciences) with growth medium. Once the cells approached confluence, they were passaged consecutively into 75 cm^2 flasks (BD Biosciences). Once these flasks became confluent, the cells were detached with trypsin 0.05% and EDTA: part of these cells were used for DNA extraction, and part were frozen.

3.1.10.3 DNA isolation and amplification

Genomic DNA was extracted from 15 BMSCs clonal colonies using a DNeasy Tissue Kit according to the manufacturer's instructions (Qiagen, Valencia, CA, USA). DNA quantity and quality was then assessed with a NanoDrop 1000 Spectrophotometer (Thermo Scientific, Rockville, MD, USA). Only DNA with a 260/280 nm ration ≥ 1.7 was used in the polymerase chain reaction (PCR) assay.

DNA was amplified by standard PCR in a GeneAmp PCR System 9700 (Applied Biosystems, Foster City, CA, USA). The reaction was run with Platinum Taq DNA Polymerase High Fidelity (Thermo Scientific) with primers HRAS Exon 2 Forward and Reverse (displayed in Table 3.1). The DNA sequence was amplified by 35 cycles of denaturation at 94°C for 15 seconds, annealing at 55°C for 30 seconds, and extension at 68°C for 25 seconds. The PCR product was cleaned with a QIAquick PCR Purification Kit (Qiagen). Sequencing of this particular *HRAS* exon was

selected because an *HRAS* G13R mutation had been identified previously in the patient's nevi through exome sequencing [61]. To corroborate correct DNA amplification, electrophoresis of the PCR products was performed on a Novex TBE Pre-Cast Gel with 6% acrylamide (Thermo Scientific) following manufacturer's instructions.

Table 3.1 Primers used for PCR, qPCR and Sanger Sequencing

HRAS Exon 2 (PCR) - Forward: AGGTGGGGCAGGAGACCCTGTAG - Reverse: AGCCCTATCCTGGCTGTGTCCTG
HRAS Reverse (Sanger sequencing) - TGGGCTCGCCCGCAGCAGCTGCTGGCACCTGG
pCGN NRAS (PCR) - Forward: CACCATGGCTTCTAGCTATCCTTATG - Reverse: TTACATCACCACACATGGCAATCC
hFGF23 (qPCR) - Forward: CACAGCCACAGCCAGGAACAG - Reverse: GTAATCACCACAAAGCCAGCATCC
hGAPDH (qPCR) - Forward: TCTCTGCTCCTCCTGTTC - Reverse: GACTGCCGACCTTCACCTT
hGAPDH (qPCR) - Forward: TCTCTGCTCCTCCTGTTC - Reverse: GACTGCCGACCTTCACCTT
mFGF23 (qPCR) - Forward: CCATTGCTTGGCTCCAACTG - Reverse: CATCAGGGCACTGTAGATGG
mGAPDH (qPCR) - Forward: CGTGTTCCTACCCCCAATGT - Reverse: TGTCATCATACTTGGCAGGTTTCT
HA-tag (qPCR) - Forward: CTTATGACGTGCCTGACTATG - Reverse: CTGGATTAGCTGGATTGTCAG

3.1.10.4 Sanger sequencing

Sanger sequencing is a widely used DNA sequencing technique. During Sanger sequencing, DNA polymerases copy single-stranded DNA templates by adding dideoxynucleotides to a growing chain. These special nucleotides are labeled with a different color dyes. A chromatogram is generated with these data, allowing for the reading of the sequence of nucleotides in the amplified region (Figure 3.5, image extracted from [61]). Sanger sequencing was performed at the NIDCR gene core on a 3730 DNA Analyzer (Applied Biosystems) on the PCR products with primer *HRAS* Reverse (Table 3.1). Results were processed with the Chromas Lite 2.0 software (Technelysium, South Brisbane, Australia).

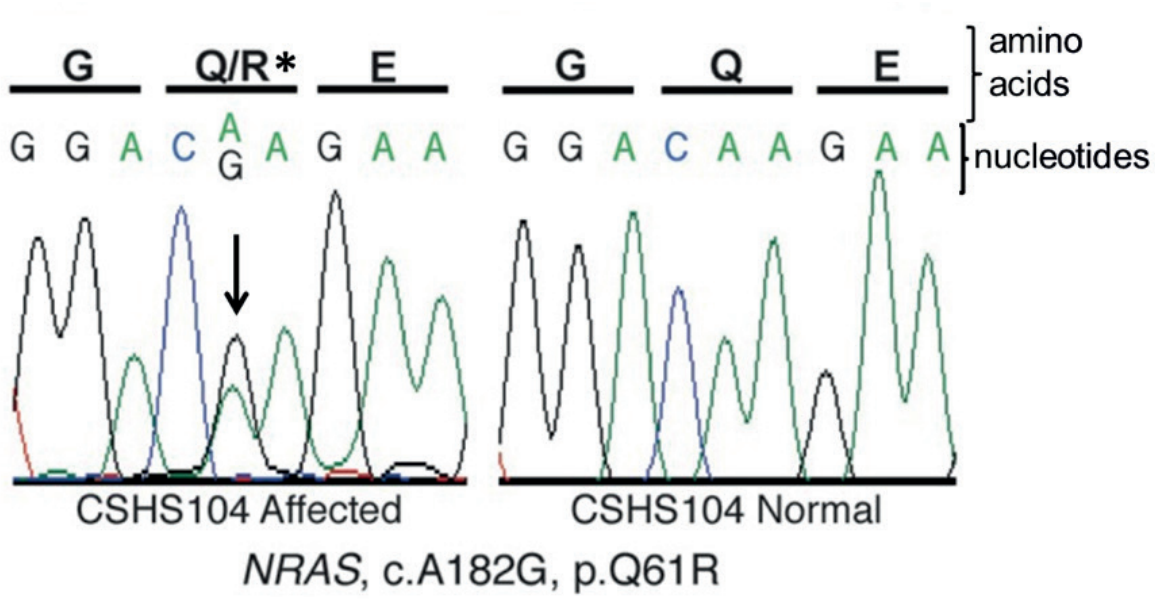

Figure 3.5 Example of a Sanger sequencing chromatogram. Each of the color waves represents a specific nucleotide e.g. G=guanosine=black, A=adenosine=green, C=cytosine=blue, T=thymidine=red (not shown). This image shows two different waves overlapping at one point of the NRAS sequence (arrow), indicating a mutation in one of the DNA strands (heterozygous mutation) that led to a change in the amino acid sequence (asterisk). Image adapted from [61].

3.1.11 Literature Search Strategy

A Medline search was performed to identify all possible published CSHS cases. The following term combinations were used without restrictions: "nevus rickets," "nevus hypophosphatemia," "nevus fibrous dysplasia," "phacomatosis pigmentokeratotica." "Fibrous dysplasia" was used in the search as some papers used this term to describe cases that in retrospect were clearly CSHS. Case reports of subjects with EN, CMN, or PPK (coexistence of EN and speckled lentiginous nevi), were selected when rickets and/or focal dysplastic skeletal lesions were part of the subject's medical history and family history was negative for inherited skeletal disorders. In addition, references were scrutinized in the retrieved reports in an effort to identify additional CSHS cases. The following data was collected from the published reports when available:

- Gender and ethnicity: if not stated in the paper, ethnic background was speculated on the basis of images provided and geographic location of the authors' medical center.
- Cutaneous nevi: skin lesions were classified either as EN (which included both NS and KEN), CMN, or PPK (when the term PPK was not used but the images or description depicted EN and speckled lentiginous nevi (a subtype of melanocytic nevi) it was classified as PPK.
- Biochemical profile
- Presence and age of onset of hypophosphatemia
- Incidence of fractures and skeletal deformities
- Presence and distribution of dysplastic skeletal lesions
- Response of rickets/hypophosphatemia to nevus treatment
- Response of hypophosphatemia/rickets to oral medications
- Natural history of skeletal disease
- Incidence of extra-cutaneous/extra-osseous abnormalities

3.2 Materials and Methods for the development of experimental CSHS models

Here we present the methods for a series of laboratory experiments, including *in vitro* and *in vivo* models that were created in an effort to replicate some aspects of CSHS's physiopathology.

3.2.1 In vitro experiment I: transduction of hBMSCs with mutant NRAS-bearing adenoviruses

3.2.1.1 Background and rationale

This experiment consisted in inserting *RAS* mutations into hBMSCs through adenoviral gene transfer. We speculated that since *RAS* mutations in pluripotent stem cells give rise to CSHS, inserting *RAS* mutations in BMCS, the progenitor skeletal cells, would simulate CSHS pathophysiology and therefore serve as a suitable *in vitro* model to test the effects of RAS hyperactivity on FGF23 production. Since FGF23 is normally produced by osteocytes (mature bone cells embedded in mineral matrix), we tried to differentiate the transduced BMCSs into more mature cells by culturing them in conditions that have been experimentally proven to bring about differentiation along the osteogenic lineage, so-called osteogenic media. In addition, given that PMTs express both endothelial and osteocytic markers (unpublished data), we also cultured a subset of cells on Matrigel® (frequently used for endothelial cell culture) with endothelial media to assess whether "endothelial-like" conditions would aid mutant cells to express and produce higher FGF23 levels. Replicant-deficient adenoviruses were the chosen vectors for gene transfer because unlike other viral vectors, they do not integrate into the host cell genome avoiding the potential disruption of essential genes. Further, they also exhibit a higher transduction efficiency compared to other viral systems and to plasmid transfection, especially in primary cell cultures [146].

NOTE: transduction refers to the process of inserting exogenous DNA into a cell by a viral vector, while transfection refers to the same process but employing non-viral methods (e.g. plasmid transfection).

3.2.1.2 Generation of mutant and WT NRAS adenoviruses

The first step for creating an adenoviral vector consists in selecting the gene of interest that will be expressed in transduced cells. In our case, we selected complementary DNA (cDNA) templates from the following HA-tagged plasmids: pCGN *NRAS* Q61R (which harbors a mutation that has been identified in CSHS), and pCGN *NRAS* WT (control) (Addgene, Cambridge, MA, USA). The HA-tag, which characterizes the pCGN plasmids, is an 8-amino acid sequence that is used very frequently as an epitope tag in expression vectors to facilitate the detection and purification of proteins.

The next step consisted in amplifying the gene of interest and inserting it in a gateway vector for molecular cloning. The primers were designed so that the amplified sequence included the *NRAS* cDNA, the HA-tag, and specific sequences required for directional cloning as per manufacturer's instructions (Invitrogen, see below). The PCR reaction was carried out in a

thermocycler using Phusion High-Fidelity Hot Start DNA Polymerase (New England Biolabs, Ipswhich, MA, USA) with primers pCGN *NRAS* Forward and pCGN *NRAS* Reverse (displayed in Table 3.1). The cDNA sequence was amplified by 35 cycles of denaturation at 94°C for 15 seconds, annealing at 60°C for 30 seconds, and extension at 68°C for 25 seconds. The PCR product was cleaned with a QIAquick PCR Purification Kit. To verify that the correct sequence was amplified, an electrophoresis gel was run and subsequently sent a sample for Sanger sequencing as described in section 3.1.10.3. Primer pCGN *NRAS* F was used for Sanger sequencing.

After verifying the sequence, the PCR products were delivered into the pENTR gateway vector following manufacturer's instructions (Invitrogen). The DNA from the recombination reaction was then used to transform competent STBL2 *E. coli* cells following manufacturer's instructions (Invitrogen). Bacterial transformation is the process by which certain bacteria, known as competent bacteria, take up foreign DNA. This foreign DNA has to have an origin of replication that can be recognized by the bacterial DNA polymerases. Because the plasmids used for bacterial transformation include an antibiotic resistance gene, only bacteria that have been successfully transformed will survive and form a colony when plated on an agar plate treated with that antibiotic (Figure 3.6, image extracted from [147]). Thus, transformed bacteria can be selected and subsequently replicated in large amounts from which plasmid copies can be purified. This comprises the basic strategy behind molecular cloning. In the case of the pENTR vector, transformed bacteria were selected with kanamycin 50 µg/ml/covered agar plates (KD Medical, Columbia, MD, USA).

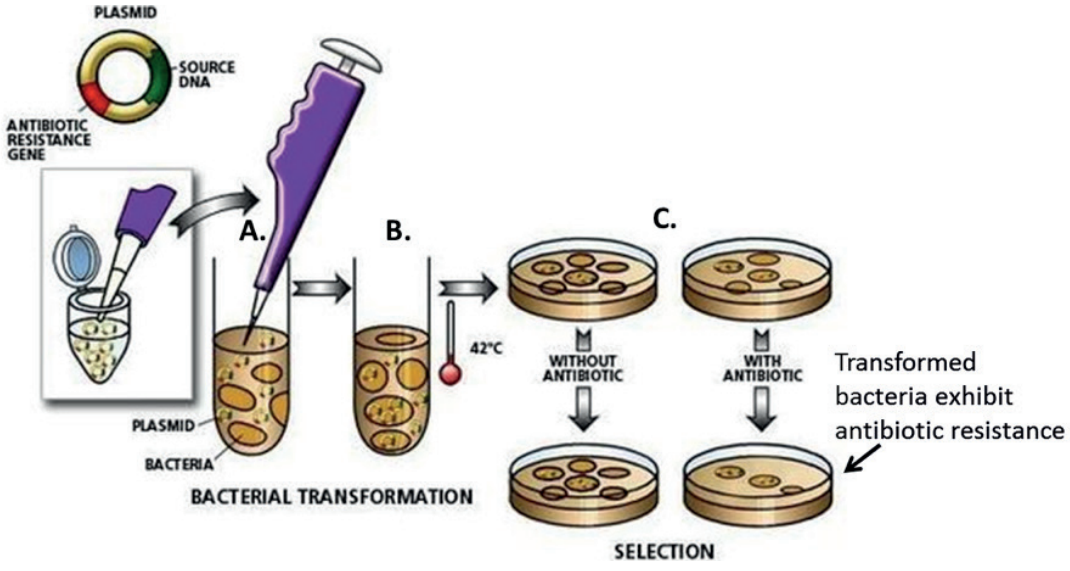

Figure 3.6 Diagram representing bacterial transformation.(A.) Plasmids containing the gene of interest (source DNA) and an antibiotic resistance gene, are mixed with competent bacteria. (B.) When the bacteria are incubated at a certain temperature (in this particular image the temperature is 42°C), small pores are created in the bacterial walls allowing the plasmids to penetrate the cell membrane. Once in the host cell, the plasmid will be replicated by the bacterial polymerases. (C.) To select for the bacteria that have been transformed, bacteria are cultured in agar plates treated with the specific antibiotic for which the plasmid confers resistance. Therefore, only the transformed bacteria will be able to grow in the plates and can subsequently be selected for cloning. Image adapted from [147].

Sequence-verified *NRAS* Q61R-pENTR and *NRAS* WT p-ENTR clones were recombined into the pAd/CMV/V5-DEST vector following manufacturer's instructions (Invitrogen). The pENTR gateaway vector is a plasmid that is used, as its name indicates, as an intermediary to introduce the gene of interest into a suitable plasmid backbone. In our case we were interested in generating an adenoviral vector, so we selected the pAd/CMV/V5-DEST vector, which contains all the necessary genetic information to generate replication-incompetent adenovirus. These viruses can efficiently infect cells delivering the genetic material into the host cell, but lack a part of the necessary genome for viral replication which significantly reduces the potential hazards associated to their handling.

When the pENTR vectors were recombined with the pAd/CMV/V5-DEST vector through a series of enzymatic steps, the pAd/CMV/V5-DEST vector was cloned through bacterial transformation as described above. Ampicillin 100 µg/ml agar plates (KD Medical) were used in this case for bacterial selection. Next, the purified destination clones were linearized with a restriction enzyme Pac I (New England Labs) and transfected into HEK 293A cells (Invitrogen) as per manufacturer's instructions. These cells contain the gene that the replication-incompetent adenovirus are lacking, thus allowing us to produce the virus, in our case Ad-NRAS Q61R and Ad-NRAS WT, and to amplify the viral titer.

3.2.1.3 hBMSC immunofluorescence and fluorescence

BMCSs were transduced with the adenoviruses and subsequently immunofluorescence (IF) directed towards an HA-tag epitope was performed. This was done to confirm the infective properties of the newly generated adenoviruses and to calculate the volume of Ad-NRAS WT and Ad-NRAS Q61R viral stock needed to infect approximately 90% of hBMCSs in 9.5 cm^2 wells (6-well plates) (BD Biosciences).

Human BMSCs were obtained from a bone marrow aspirate from a healthy volunteer under a NIH IRB-approved protocol. The cells were third passage lines when they were used for this experiment. Cells were seeded on 6-well plates (seeding density: 0.3 x 10^6 cells/well) in which sterile round coverslips had been placed previously. "Standard" BMSCs growth medium was used for cell culture (see section 3.1.10.1). When 70% confluence was reached, cells were transduced with the following viral stock volumes (both WT and mutant *NRAS* adenoviruses): 30 µl, 50 µl, 100 µl, 125 µl, 200 µl and 300 µl. Prior transduction, media was aspirated and cells were washed with sterile phosphate buffered solution (PBS). Cells were then treated with viral stock added to serum free media during an overnight incubation. The following day, the virus-containing media was aspirated and replaced by standard growth medium. Positive HA-tag IF controls were created by transfecting 2.5 µl of wt-NRAS pCGN plasmid (Addgene) into other wells with hBMCSs with with Opti-MEM reduced serum media and Lipofectamine 2000 (Thermo Fisher) according to the manufacturer's protocol. Other cells were not treated to serve as negative controls. Forty-eight hours after transduction and transfection, cells were fixed with 4% PFA and the cover slips were transferred into clean 12-well plates (BD Biosciences). IF was then performed on the coverslips following Cell Signaling's IF protocol [148]. The primary antibody was a rabbit HA-tag monoclonal antibody (1:1600 dilution) (Cell Signaling Technology, Danvers, MA, USA), and the secondary was an Alexa Fluor® 488 Conjugate (1:1000 dilution) (Cell

Signaling Technology). Digital images were obtained using a Zeiss Axio Imager Z1 microscope (Zeiss, Oberkochen, Germany), and processed using the AxioVision 4.8 Software (Zeiss). Ad-GFP, replication-deficient adenoviruses harboring a green fluorescent protein (GFP) construct, a kind gift from Dr. Larry Fisher (NIDCR), were used as transduction controls for the hBMCSs adenoviral transduction experiment (section 3.2.1.4). Due to its intrinsic fluorescent properties, viral stock volume was calculated directly under an epifluorescent microscope, Axiovert AX10 (Zeiss) 48 hours after transduction. Images were captured with a monochrome Axiocam Mrm camera (Zeiss), and images were processed with the AxioVision 4.8 software.

This experiment was performed twice.

3.2.1.4 hBMSC transduction

Wild type hBMCS were seeded in 6-well plates (seeding density: 0.3 x 10^6 cells/well). Cells were cultured in either: (A) standard BMSC growth medium, (B) osteogenic medium: standard BMSC growth media plus dexamethasone 10^{-8} M (Sigma-Aldrich, St. Louis, MO, USA), ascorbic acid 10^{-4} M (Wako Chemicals, Cape Charles, VA, USA) and 5 mM β-glycerophosphate (BGP) (Sigma), or (C) endothelial media on Matrigel® -coated plates: media 199 (Thermo Fisher Scientific), 2 mM L-glutamine, 100 U/ml penicillin, 100 µg/ml streptomycin sulfate (Invitrogen), 10% lot-selected FBS (Atlanta Biological), VEGF 50 ng/ml , IGF-1 10 ng/ml, bFGF 10 ng/ml (R&D systems, Minneapolis, MN, USA). For Matrigel® plate coating, Matrigel® basement membrane matrix (BD Biosciences) was thawed overnight at 4°C, and diluted 1:40 in chilled 199 media. Six-well plates were covered with 1.5 ml diluted Matrigel® and left overnight at 4°C. The following day, excess Matrigel® was removed. For each condition, 4 6-well plates were used.

When 70% confluency was reached, cells were treated overnight with serum-free media containing viral stock: Ad-GFP and Ad-*NRAS* Q61R 200 µl stock/well, Ad-*NRAS* WT 300 µl stock/well. The following day the virus-containing media was aspirated and the type of growth media that had been used prior transfection was restarted. Media was changed every 3 days.

This experiment was performed twice.

3.2.1.5 Protein collection and FGF23 measurement

At day 5 and 12 post-transduction, cell lysates and media from cells treated in all conditions were collected for protein measurement. Three wells/condition/time point were collected. Wells were first washed with cold PBS; subsequently, 300 µl of RIPA buffer (Thermo Fisher) with proteinase inhibitor (EMD Millipore) was added. Cells were scraped and collected and were immediately sonicated for 30 seconds. Lysates were centrifuged at 4°C at maximum speed for 15 minutes and supernatants were collected. Human FGF23 protein levels were measured both in the cell lysate supernatant and in the media with an intact FGF23 ELISA kit as per manufacturer's instructions (Immutopics).

3.2.1.6 RNA collection and quantitative real time PCR (qPCR)

At day 5 post-transfection, RNA extraction was performed using RNEasy kit according to the manufacturer's instructions (Qiagen). Three wells/condition/time point were collected and analyzed. RNA quantity and quality was assessed with a NanoDrop 1000 Spectrophotometer (Thermo Scientific). Only samples with a 260/280 nm ratio ≥ 1.8 were used for downstream analysis. RNA integrity was assessed through electrophoresis with a formaldehyde gel as previously described [149].

cDNA was generated with 1 mg of RNA with the iScript cDNA synthesis kit (Bio-Rad Laboratories, Hercules, CA, USA) as per manufacturer's instructions. qPCR was performed using hFGF23 R and F primers (Table 3.1) and iQ SYBR Green Super-mix (Bio-Rad) per manufacturer's protocol. The plate was run in a CFX96 real-time PCR (RT-PCR) detection system (Bio-Rad). cDNA was amplified by 40 cycles of denaturation at 95°C for 10 seconds, annealing at 60°C for 30 seconds. Each sample was run in triplicates. Results from cells that were cultured with the same treatment during the same experiment were averaged. cDNA from a stably transfected HEK cell line expressing FGF23 served as positive control [150]. qPCR results, expressed as critical threshold (C_T) values, were normalized to the levels of human Glyceraldehyde 3-phosphate dehydrogenase (GAPDH) (hGAPDH primers shown in Table 3.1) generating ΔCT values. Levels of relative expression were calculated as $2^{-\Delta CT}$.

This experiment was performed twice.

3.2.2 In vitro experiment II: transduction of IDG-SW3 cells with RAS-bearing adenoviruses

3.2.2.1 Background and rationale

In this experiment, artificial gene transfer was performed with the same *NRAS*-adenoviral vectors on an osteocytic cell line, IDG-SW3, to assess the effects of activating *RAS* mutations on differentiated bone cells. IDG-SW3 cells are reported to express *Fgf23* [151].

3.2.2.2 IDG-SW3 culture

IDG-SW3 cells were a kind gift from Dr. Lynda Bonewald. Cells were first expanded in permissive conditions and subsequently transferred to 6-well collagen-coated plates where osteogenic differentiation was induced as previously described [151]. Briefly, cells were initially plated into T 1.75 flasks (BD Biosciences) at 33°C. Flasks had been previously coated with rat-tail I-collagen per manufacturer's instructions (Invitrogen). The growth media used consisted of: α-MEM, 2 mM L-glutamine, 100 U/ml penicillin, 100 μg/ml streptomycin sulfate (Invitrogen), 10% lot-selected FBS (Atlanta Biological), and interferon (INF)-γ 50 U/ml (Invitrogen). These cells have the peculiarity that they proliferate at 33°C and in the presence of INF-γ. After reaching confluence, cells were trypsinized with 0.05 %Trypsin/EDTA and re-plated in collagen-coated

6-well plates at a density of $4x10^4$ cells/cm^2. Cells were cultured in 37°C degrees with the same media but without INF-γ and adding 50 µg/ml ascorbic acid and 4 mM BGP. In these conditions, IDG-SW3 cells stop proliferating and initiate osteogenic differentiation.

3.2.2.3 IDG-SW3 adenoviral transduction

At days 2, 14, and 28 of osteogenic differentiation, a subset of cells were transduced with 100 µl of the Ad-NRAS Q61R and 150 µl of Ad-NRAS WT viral stock as described in 3.2.1.3 (3 wells/condition/time point). Volumes of viral stock were estimated based on the results of the hBMCS IF experiment (see section 3.2.1.3). Because calcitriol had been reported to increase significantly *Fgf23* expression in IDG-SW3 cells [151], we added calcitriol 1000 pmol/L (Stem Cell technologies, Vancouver, Canada) to 3 untreated wells at day 14 and 3 untreated wells at day 28 to serve as positive controls. Other wells did not receive any treatment (untreated controls).

This experiment was performed 3 times.

3.2.2.4 RNA collection

RNA was extracted from untreated cells at day 2 to serve as negative controls [151]), at day 16 (treated cells at days 2 and 14, and untreated cells at day 16), and at day 30 (treated cells at day 28, and untreated cells at day 30). RNA extraction and conversion to cDNA, and qPCR were performed as previously described in section 3.2.1.6, but using mFGF23 primers for this experiment (Table 3.1). cDNA from a plasmid containing the *mFgf23* sequence, a generous gift from Dr. Beate Lanske, was also used as a positive control for *Fgf23* expression.
To asses for viral transduction efficiency in IDG-SW3 cells, HA-tag expression was measured using HA-tag primers (Table 3.1). RNA extracted from hBMCSs transduced with the Ad-NRAS Q61R (section 3.2.1.6) was used as a positive transduction control.

Gene expression was normalized to mGAPDH (primers displayed in Table 3.1).

3.2.3 In vitro experiment III: investigation of the paracrine effects of mutant hBMSCs on mFgf23 expression in IDG-SW3 cells

3.2.3.1 Background and rationale

In this experiment, we tested the possibility that mutant hBMSCs were not actually the source of FGF23 but that secreted some kind of paracrine factor that increased FGF23 production by non-mutant osteocytes. To do so, we assessed *Fgf23* expression in IDG-SW3 cells that had been treated with media in which mutant CSHS hBMSCs had been cultured in.

3.2.3.2 IDG-SW3 paracrine experiment

IDG-SW3 cells were cultured as described in section 3.2.2.2. At days 14 and 28 of osteogenic differentiation, media was aspirated from a subset of wells (3 wells/condition/time point), and was replaced by growth medium in which *HRAS* G13R or WT (control) BMCSs from subject CSHS105 (see section 3.2.4) had been cultured. This growth medium was collected after 4 days of BMSCs culture to accumulate the largest quantity of paracrine factors possible prior to media change. Calcitriol 1000 pmol/L was added to 3 untreated wells at day 14 and 3 untreated wells at day 28 to serve as positive controls. Other wells did not receive any treatment (untreated controls). After 48 hours of culture with BMSC media, RNA was collected from the IDG-SW3 cells as described in section 3.2.2.4 with primers mFGF23. Gene expression was normalized to mGAPDH. This experiment was performed 3 times.

3.2.4 In vitro experiment IV: FGF23 expression in CSHS hBMSCs

3.2.4.1 Background and rationale

FGF23 expression was assessed in mutant and WT BMCSs colonies from subject's CSHS105 (see section 3.1.10) after 21 days of osteogenic culture to investigate whether mutation-bearing cells induced *FGF23* expression.

3.2.4.2 hBMSC culture

Cells from 3 WT *HRAS* hBMCS clonal colonies were mixed in equal proportion. The same was done with 3 *HRAS* G13R hBMSCs colonies. Subsequently, WT and mutant cells were cultured separately and in combination (1:1 proportion) in 6-well plates either with BMSC osteogenic media or standard media for 21 days (6 wells/condition). The cells were at the third passage when they were used for this experiment and were plated at an initial density of: 0.3 x10^6cells/well. The FBS concentration was reduced to 5% when cells were 100% confluent. Growth media was changed every 4 days.

This experiment was performed twice.

3.2.4.3 RNA collection and qPCR

After 21 days of culture, RNA extraction for assessment of *FGF23* expression was performed as described in section 3.2.1.6. cDNA from a stably transfected HEK cell line expressing FGF23 served as positive control [129]. Target gene expression was normalized to hGAPDH.

3.2.5 hBMSC transplant experiment

3.2.5.1 Background and rationale

BMSCs have the capacity to generate ossicles, i.e. small pieces of organized bone tissue and bone marrow, when transplanted with appropriate carriers such as hydroxyapatite into immunocompromised mice [144, 152]. In addition to replicating normal bone, this procedure has been employed to successfully generate pathologic bone such as FD [144]. In an effort further characterize the histology of CSHS bone, we performed the following transplant experiment with mutant CSHS BMSCs.

3.2.5.2 hBMSC culture

Human BMSCs were obtained from an iliac crest biopsy performed on CSHS105 (section 3.1.6). After performing a single cell suspension (section 3.1.10.1), cells were seeded in two 1.75 T flasks and cultured in standard media. When confluence was attained, cells were passaged to 4 new 1.75 T flasks.

Control hBMSCs were obtained from a bone marrow aspirate from a healthy volunteer, under a NIH IRB-approved protocol that was sex- and age-matched to subject CSHS105. BMSCs obtained from the single cell suspension were cultured in standard growth medium.

Second passage cells were used for both cell populations because in our experience, ossicle formation is enhanced when cells have not undergone more than 4 passages. DNA was extracted and presence of the *HRAS* G13R mutation was assessed in both cell types as described in sections 3.1.10.3-4.

3.2.5.3 In vivo transplantation assay

For each transplant, 2 x 10^6 cells were used; cells were loaded onto CryoTubes with 40 mg of sterile hydroxyapatite/tricalcium phosphate particles (NuVasive, San Diego, C A, USA) and 1 ml of growth medium. To facilitate cellular attachment to the carrier, cells were incubated with the particles for 90 minutes with slow rotation (25 rpm) at 37°C. Subsequently, excess media was aspirated and the mixture was transplanted subcutaneously into the upper and lower back of 8-week-old SCID Hairless Congenic Mouse (Charles River). Incisions were closed with 9 mm steel wound clips (Roboz Surgical Instrument Co., Rockville,MD, USA). Surgeries were performed under 2-5% of isofluorane anesthesia. Fourteen mice were operated; in each mouse, 2 CSHS BMSCs and 2 control BMSC transplants were inserted.

Transplants were harvested 15 weeks after surgery. Animals used in this experiment were housed and handled accordingly to animal study proposals approved by the NIDCR Animal Care and Use Committee.

3.2.5.4 Histology

Half of the harvested transplants were fixed and then decalcified in 0.5 mM EDTA for 4 weeks at 4°C . Subsequently they were embedded in paraffin as described in section 3.1.7. Five μm sections were obtained and stained with standard H&E for both histological survey and for quantification of bone tissue formation in the transplants.

The remaining transplants were embedded in MMA without prior decalcification. MMA sections were stained with Goldner trichrome as described in section 3.1.7.

3.2.6 Generation of transgenic mouse strains as models for CSHS

3.2.6.1 Background and rationale

Genetically modified mice have proven very useful for the study of human diseases including skeletal dysplasias and disorders featuring Fgf23 excess [75, 87]. Thus, we attempted to generate a conditionally *knock-in* mouse model through Cre-Lox recombination technology to investigate the effects of activating *Ras* mutations on the bone as a model for CSHS's skeletal findings.

Cre-Lox recombination is based on the ability of the enzyme Cre recombinase to detect specific DNA sequences called LoxP sites, and to cut double stranded DNA between them [153]. Genetic recombination is then attained through the rejoining of the strands by a DNA ligase. The 2 transgenes that were critical for the generation of the conditional *knock-in* mouse models described in this thesis consisted in a tissue-specific cre-recombinase, and a mutant *Kras* gene inserted in its specific locus attached to an upstream a LoxP- STOP codon- LoxP cassette (LSL). The role of the LSL cassette is to prevent the gene of interest, (in this case, a mutant *Kras*) gene, from being expressed until Cre recombination occurs. To attain tissue specificity, Cre transgenes are typically designed downstream to a specific promoter, or driver, which limits the expression of the enzyme to cells expressing that promoter (Figure 3.7, image extracted from [154]). In addition, certain Cre transgenes are designed so that they can only be expressed in the presence of a particular molecule, such as tamoxifen [153]. These inducible models not only allow us to control the location and timing of transgenic expression, but also to control (albeit roughly) the extent of recombination through the titration of the dose of the inductor substance.

The LSL-KrasG12D mouse strain (NCI Frederick Mouse Repository) was the selected LSL-mutant *Ras* strain for our mouse models because it has been thoroughly validated in many oncogenic murine models, and because *KRAS* G12D has been identified in some cases of epidermal nevus [155].

For our initial mouse model, expression of the mutant *Kras* was limited to immature cells of osteoblast lineage by using the 3.6 kb fragment of the collagen type I α-1 (Col 3.6) promoter as the Cre driver [156]. An inducible system was initially chosen with the objective of creating a partial, and therefore "mosaic" activation of the Kras transgene. The tamoxifen-inducible Col 3.6 cre recombinase strain (Col3.6-CreEr) was purchased from the Jackson Laboratory (Jackson

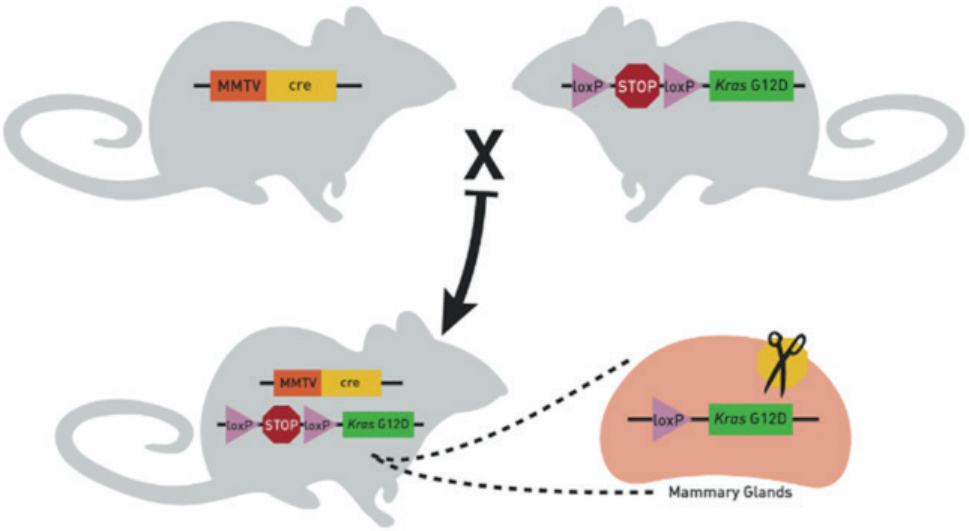

Figure 3.7 Generation of a tissue specific knock-in mouse model through Cre/Lox recombination technology. In this illustration, a transgenic strain harboring the Lox-Stop-Lox Kras G12D targeted transgene is bred to a strain that expresses a Cre recombinase exclusively in mammary tissue through an MMTV (mouse mammary tumor virus) promoter. The stop codon will be excised in the mammary glands in double transgenic offspring, leading to a tissue-specific expression of the Kras oncogene. Image adapted from [154].

Laboratory, Farmington, CT, USA). To monitor for LSL recombination, and additional LSL transgene containing a luciferase (Luc) reporter was employed: ROSA26 LSL-Luc (The Jackson Laboratory) [157]. With this transgene, luciferase is expressed in cells that undergo Cre recombination. The administration of luciferin to this animal leads to the emission of bioluminescence in recombined tissue which can be detected by special sensors.

Two other mouse models were generated employing the paired-related homeobox gene-1(*Prx1*) as the Cre driver. *Prx1* is expressed in the limb bud mesenchyme and in parts of the craniofacial mesenchyme of the mouse embryo [158]. During postnatal life, *Prx1* expression is detected in a subset of limb and calvarial periosteal cells that appear to have both osteogenic and chondrogenic potential [159]. For the second model, we employed a strain harboring a tamoxifen-inducible *Prx1* cre recombinase (Prx1-CreER). This strain was a kind gift from Dr. Shunichi Murakami from Case Western University. The third model was designed with a constitutively activated, therefore non-inducible, *Prx1* promoter (*Prx1*Cre) (The Jackson Laboratory). The luciferase reporter and LSL-KrasG12D transgene were used in all the models.

3.2.6.2 Breeding strategies

The breeding scheme used for the generation of the triple transgenic strains is exemplified in Figure 3.8. Henceforth, mouse model 1 will refer to the strain harboring the following transgenes: Col3.6-CreER $^{+/-}$/ LSL-KrasG12D$^{+/-}$/ROSA26 LSL-Luc$^{+/+}$; mouse model 2 will refer to the strain harboring: Prx1-CreER $^{+/-}$/ LSL-KrasG12D$^{+/-}$/ROSA26 LSL-Luc$^{+/+}$; and mouse model 3 to the strain harboring: Prx1Cre $^{+/-}$/ LSL-KrasG12D$^{+/-}$/ROSA26 LSL-Luc$^{+/+}$.

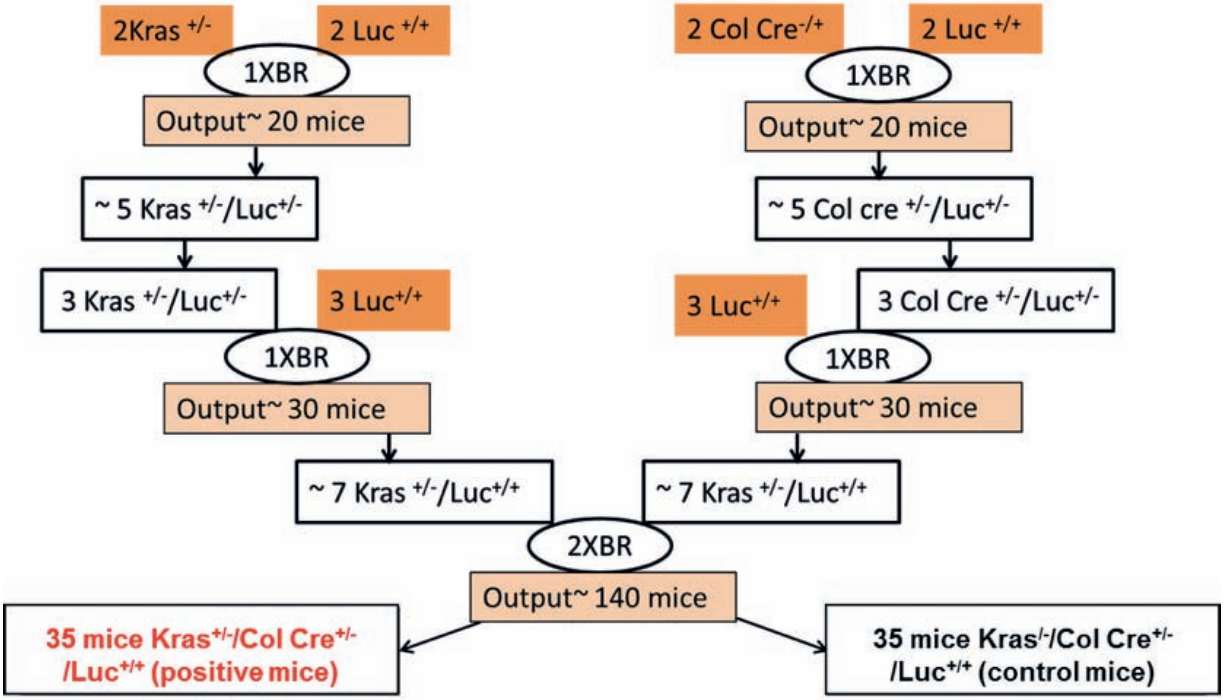

Figure 3.8 Breeding scheme for the generation of mouse model 1. The diagram shows an example of the breeding steps performed to obtain 35 positive experimental and 35 control mice. The numbers displayed are based on the premise that the average number of pups/litter is 10 mice, that 50% of mice will be either male or female, and that genetic inheritance will follow a typical mendelian pattern. The same breeding scheme was applied for mouse models 2 and 3 but replacing the Col3.6-CreEr, for the Prx1-CreER and Prx1Cre transgenes, respectively. The orange boxes point to commercially purchased mice.
Abbreviations: BR: breeding round, Kras$^{+/-}$: mice harboring the LSL-KrasG12D transgene, Luc: mice harboring the ROSA26 LSL-Luc reporter gene, Col Cre$^{+/-}$: mice harboring the Col3.6-CreEr gene.

Animals used in these experiments were housed and handled accordingly to the animal study proposals approved by the NIDCR Animal Care and Use Committee.

NOTE: because we did not detect a positive genotype in any of offspring from mouse model 3 breeding pairs (i.e. no mice harbored both the Prx1Cre and the LSL-KrasG12D transgenes), the following procedures were performed only with mice from mouse models 1 and 2.

3.2.6.3 Weight measurments

Weight was measured in a subset of mice in both mouse models 1 and 2 to assess whether activation of mutant *Kras* had an impact on normal weight gain. Briefly, 5 positive (Cre$^+$, LSL-KrasG12D$^+$) and 5 control mice (Cre$^+$, LSL-KrasG12D-) female mice were weighted prior tamoxifen induction, and thereafter at 4, 12, 18 and 24 weeks post-tamoxifen. All animals were treated with the highest dose of tamoxifen (i.e. 2 mg/day for 5 days (section 3.2.6.5)). To decrease inter-litter variability, only 2 litters of mice were used for this purpose.

3.2.6.4 Genotyping

Mouse DNA was extracted from ear biopsies with REDExtract-N-Amp™ Tissue PCR Kit (Sigma-Aldrich) per manufacturer's instructions. Genomic DNA (1 µl) was diluted in 20 µl PCR reaction of GoTaq Green Master Mix (Promega). The DNA sequence was amplified by 35 cycles of denaturation at 94°C for 15 seconds, annealing at 60°C for 30 seconds, and extension at 72°C for 25 seconds. Primers used for genotyping are displayed in Table 3.2.

Table 3.2 Primers for genotyping transgenic mice and transgene recombination assessment

LSL-KrasG12D - Forward: AGCTAGCCACCATGGCTTGAGTAAGTCTGCA - Reverse: CCTTTACAAGCGCACGCAGACTGTAGA
WT Kras - Forward: GTCGACAAGCTCATGCGGGTG - Reverse: CCTTTACAAGCGCACGCAGACTGTAGA
ROSA26 LSL-Luciferase - Forward: CCAGGGATTTCAGTCGATGT - Reverse: AATCTGACGCAGGCAGTTCT
WT Luciferase (absence of the ROSA26 LSL-Luciferase trangene) - Forward: CGTGATCTGCAACTCCAGTC - Reverse: GGAGCGGAGAAATGGATATG
Cre Recombinase (includes all cre drivers) - Forward: GGACATGTTCAGGGATCGCCAGGCG - Reverse: GCATAACCAGTGAAACAGCATTGCTG
LSL-KrasG12D transgene recombination assessment primers (PCR + Sanger sequencing) - Forward: GTCTTTCCCCAGCACAGTGC - Reverse: CTCTTGCCTACGCCACCAGCTC

3.2.6.5 Inducible Cre Activation

Tamoxifen (Sigma) diluted in Mygliol (Cremer Oleo, Hamburg, Germany), a lipidic vehicle solution, was administered intraperitoneally for 3 consecutive days (0.1 mg/day) to 3-week old mice, both in positive and control mice. Due to the lack of observable effects, the dose was progressively increased up to 2 mg/day for 5 consecutive days.

3.2.6.6 In vivo imaging of luciferase activity

Forty-eight hours after the last tamoxifen dose, VivoGlo™ luciferin (Promega, Madison, WI, USA) (50 mg/kg) dissolved in a sterile saline solution, was injected into the mice. Ten minutes after luciferin administration, mice were anesthesized with 2-5% isofluorane and subsequently placed in a light-tight chamber equipped with a charge-coupled device IVIS imaging camera (Xenogen Biosciences, Cranbury, NJ, USA). Photons were collected for a period of 2 minutes and images were obtained using LIVING IMAGE software (Xenogen Biosciences).

3.2.6.7 Verification of LSL-KrasG12D recombination in the bone

To further confirm *Kras* transgene recombination after tamoxifen induction, bone DNA was examined. Briefly, femurs from 4 positive and 2 control mice were harvested 1 week after tamoxifen injections, were disposed of bone marrow, and subsequently snap-frozen in liquid nitrogen. Femurs were then ground using a mortar and pestle and DNA was subsequently extracted from the pulverized tissue with REDExtract-N-Amp™ Tissue PCR Kit (Sigma-Aldrich) per manufacturer's instructions. The DNA sequence was amplified by 35 cycles of denaturation at 94°C for 15 seconds, annealing at 58°C for 30 seconds, and extension at 68°C for 25 seconds with primers LSL-KrasG12D for transgene recombination assessment (Table 3.2). The PCR product was sequenced by the Sanger sequencing using the same set of primers.

3.2.6.8 X-ray imaging

Whole mouse X-rays were taken prior to tamoxifen injection, two weeks after, and on a monthly basis thereafter with the IVIS ILUMINA XR (Xenogen) at 30 seconds, 30-KeV exposure settings. Femurs were harvested from mice that had been treated with the highest dose of tamoxifen at 1, 3, and 6 months post-tamoxifen induction (5 mice/genotype/time point), and were subject to X-ray imaging in a Faxitron MX-20 X-ray specimen radiography system and Oncology Portal Pack for Localization film (Carestream) at 40 seconds, 30-KeV exposure settings.

3.2.6.9 Histology

Femurs from positive and control mice that had been treated with the highest dose of tamoxifen at 1, 3, and 6 months post-tamoxifen (5 mice/genotype/time point). Bones were fixed with fresh 4% PFA overnight at 4°C, and were subsequently decalcified in 0.5 mM EDTA for 3 weeks at 4°C. Complete decalcification was examined through x-ray imaging. Decalcified samples were embedded in paraffin, sectioned in 5 μm slices, and stained with H&E. To assess for mineralization status, the upper limbs of the same mice were embedded in MMA. Six micrometer sections derived from the MMA blocks were stained with Goldner's trichrome. Histologic procedures employed here were the same as the ones described in section 3.1.7.

3.2.6.10 RNA extraction and assessment of mFgf23 expression in the bone

Levels of *Fgf23* expression in bone were compared between positive and prior to tamoxifen injections (3 weeks of age), and at 1, 3, and 6 months post-tamoxifen (4 mice/genotype/

time point). As previously described in section 3.2.6.7, femurs were harvested, disposed of bone marrow, and immediately snap-frozen in liquid nitrogen. Two femurs at a time (from the same mouse) were gound with a mortar and pestle and subsequently transferred to a glass homogenizer with 4 mL of Trizol® (Thermofisher). RNA was extracted following Trizol's® protocol. RNA quantity, quality and integrity were assessed as described in section 3.2.1.6.

cDNA generation and qPCR were performed as described in section 3.2.1.6 using primers mFgf23 and normalizing the results to *mGAPDH*. cDNA from the plasmid containing the *mFgf23* sequence (section 3.2.2.4) served as a positive control, and cDNA from IDG-SW3 cells collected at 2 days of osteogenic differentiation served as negative control (section 3.2.2.4).

3.2.6.11 Blood collection and laboratory testing

Blood was analyzed in female positive and control mice in mouse model 1 and 2 before tamoxifen induction, and at 1, 3, and 6 months after induction (the highest tamoxifen dose was employed). Four mice were used per time point. Blood collection was performed in anesthesized animal through total eye ennucleation. Anesthesia consisted of an intramuscular dose of Ketamine (100 mg/ml)/ Xylazine (20 mg/ml)/ Acepromazine (10 mg/ml) (1:1:4 proportion; 0.08 ml/30 g body weight). Blood was collected by placing an Eppendorf tube under the orbit (BD Biosciences). Blood was then spun at 2000 rpm for 10 min. Serum was collected and sent for analysis to the department of Laboratory medicine at the NIH clinical center. The following parameters were ordered: calcium, phosphorus, albumin, alkaline phosphatase, conventional ionogram, and renal function. Samples were ran in a Cobas 6000 Analyzer.

3.2.7 Statistical analyses

Statistical analyses were performed and graphs were prepared with GraphPad Prism 7. Data are presented as the mean ± standard deviation. Gene expression comparisons were made with samples in which RNA had been collected at the same time point. Only *in vitro* experiments that were performed 3 times underwent statistical analysis. Data distribution was analyzed by a Shapiro-Wilk normality test. Comparison between 2 groups was performed using t-Student test (normal distribution) or Mann-Whittney's U test (non-normal distribution). Comparison between 3 or more groups was performed using one-way ANOVA (normal distribution) or Kruskal-Wallis test (non-normal distribution). Significance is considered at $p < 0.05$.

4. RESULTS

4.1 Clinical characterization of the CSHS cohort

4.1.1 Demographic information

Average age at the initial admission at the NIH (plus the age of CSHS102 in the first clinical records provided to us), was 9.7 years (range 4-17, SD ± 6.3). All subjects were female except CSHS105.
Ethnic background was varied: CSHS101, 102 and 105 were Caucasian, CSHS104 was African American, and CSHS106 was Hispanic.
Demographic information and clinical findings (except biochemical data) from CSHS101,102, 104-106 are summarized in Table 4.1.

4.1.2 Height and weight

Height and weight were severely impaired in CSHS104 and 106 (both under p3). In CSHS101, height was between p5-10 and weight between p25-50 which indicated a growth alteration as her estimated mid-parental height was 175 cm (p95). CSHS105 attained expected mid-parental height (178cm, p75) and was overweight (90kg, p97). Records indicated that CSHS102 height was impaired p<3 with weight around p10-15.

4.1.3 Cutaneous nevi

Dermatological findings in the cohort included EN (CSHS101,102,105), PPK (CSHS106), and giant CMN (CSHS104). Representative photographs are displayed in (Figure 4.1 A-E). Histological images are shown in (Figure. 4.2).

4.1.4 Feautures of mineral abnormalities and skeletal dysplasia

4.1.4.1 Biochemical profile

Blood and urine biochemistries were consistent with FGF23-mediated hypophosphatemia in all the subjects. These included elevated FGF23, renal phosphate wasting (as defined by a TRP < 85%), elevated alkaline phosphatase, and normocalcemia in the absence of evidence for intrinsic tubular dysfunction or kidney disease. PTH values were sometimes elevated in the setting of vitamin D deficiency. 1,25-dihydroxyvitamin D values were variable. A mineral panel of the CSHS cohort is displayed in Table 4.2. The remaining endocrine labs including thyroid profile, growth horme, gonadotropins and estradiol were within the reference range for age and sex (data not shown).

4.1.4.2 Symptomatic onset

Hypophosphatemic symptoms had a variable age of presentation ranging from 16 months in CSHS104 to 12 years in CSHS105 (Table 4.1). The most common initial symptoms and manifestations attributed to hypophosphatemia were bone pain, widening of wrists and ankles, bone deformities (especially bowing of lower extremities), and impaired mobility.

Table 4.1 Demographic information and main clinical findings of the CSHS cohort

Subject	Sex	Ethnicity	Nevi Type	Mutation [61,126]	Age of rachitic onset (years)	Height/ Weight (percentile)	Pathologic Fractures	Scol.	Other skeletal deformities	Laterality of skin vs bone lesions	Response To oral Phosphate And calcitriol	Spontaneous improvement of mineral alterations	Extra-osseous/ Extra-cutaneous manifestations
CSHS101	F	Caucasian	EN	*NRAS* Q61R	2	p5/ p25	Yes	No	Wind swept deformity in lower extremities	Unilateral nevi; ipsilateral skeletal dysplasia	Healed rickets	No (f/u until age 9)	Brainstem lipoma; Thyroid nodule; Splenic hemangiomas
CSHS102	F	Caucasian	EN	*HRAS* G13R	1.5	<p3/ p10	Yes	Yes	Coxa vara; Lower extremities bowing and deformities secondary to fractures	Unilateral nevi; ipsilateral skeletal dysplasia	Limited effect during childhood; improved labs and ↓ fracture in adolescence	Yes. Decrease of fracture rate, age 12 (f/u until age 14)	Subaortic valve stenosis
CSHS104	F	African American	GCMN	*NRAS* Q61R	1.3	<p3/ <p3	Yes	No	Upper and lower extremity bowing	Bilateral nevi; bilateral skeletal dysplasia	Initiation of ambulation; Improved labs	No (deceased at age 4 due to pericardial effusion)	CNS melanosis; Ocular dermoid; Pericardial effusion
CSHS105	M	Caucasian	EN	*HRAS* G13R	12	p75/ p97	Yes	Yes	Pronounced leg-length discrepancy	Unilateral nevi; bilateral skeletal dysplasia	pain ↓ weakness	Yes. Resolution of mineral abnormalities at age 17 (f/u until age 19)	Colpocephaly Body asymmetry
CSHS106	F	Hispanic	PPK	*HRAS* G13R	5	<p3/ <p3	Yes	Yes	Bowing of lower extremities; leg-length discrepancy	Bilateral nevi; bilateral skeletal dysplasia	Improved labs	No (f/u until age 14)	Body asymmetry

F: female; M: male; EN: Epidermal Nevus; GCMN: congenital melanocytic nevus; PPK: phacomatosis pigmentokeratotika; p: percentile; Scol: scoliosisf/u: follow-up; CNS: central nervous system

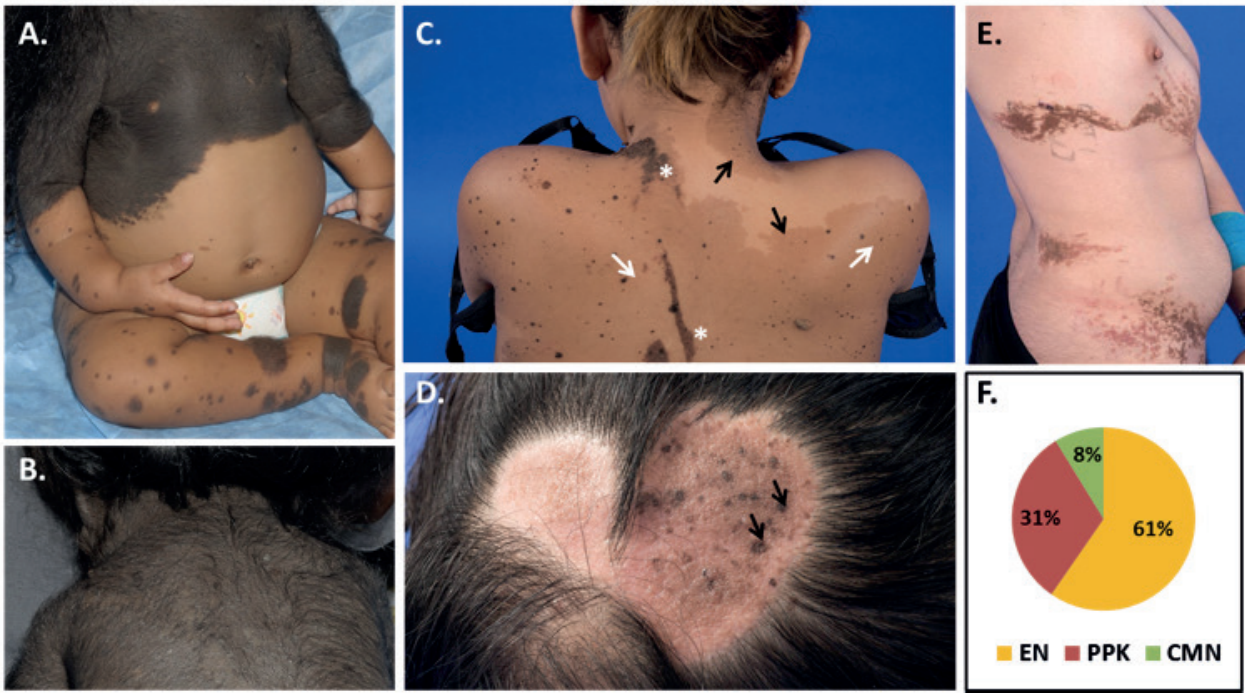

Figure 4.1 Cutaneous nevi observed in the CSHS cohort and published reports. (A) Giant congenital melanocytic nevus (CMN) in CSHS104. These extensive lesions are composed by nevomelanocytes (neural crest origin) distributed along the dermis and hypodermis. (B) Hair follicles may be enlarged and infiltrated by these cells giving the observed hairy appearance. (C) Phacomatosis Pigmentokeratotica (PPK) in CSHS106. Concomitant speckled lentiginous nevi (white arrows), a subtype of melanocytic nevi (neural crest origin), and nevus sebaceous (NS) (asterisk), a subtype of epidermal nevus (epidermal origin) are observed in PPK. Superimposed café-au-lait macules are frequently present in these patients (black arrow). (D) Representative plaque of NS in CSHS106. The scalp is a typical site for NS, where it usually appears like a round waxy alopecic patch. Small speckled lentiginous nevi (arrows) are also observed within the NS in this girl. (E) Epidermal Nevus (EN) in CSHS 105. EN is characterized by hyperplasia of elements of epidermal origin, e.g. sebaceous glands or keratinocytes (as occurs in NS and keratinocytic epidermal nevus respectively). Large epidermal nevi, as the one in this image, are typically distributed in the body following the lines of Blaschko. (F) Distribution of nevi types in 51 CSHS patients identified in published reports.

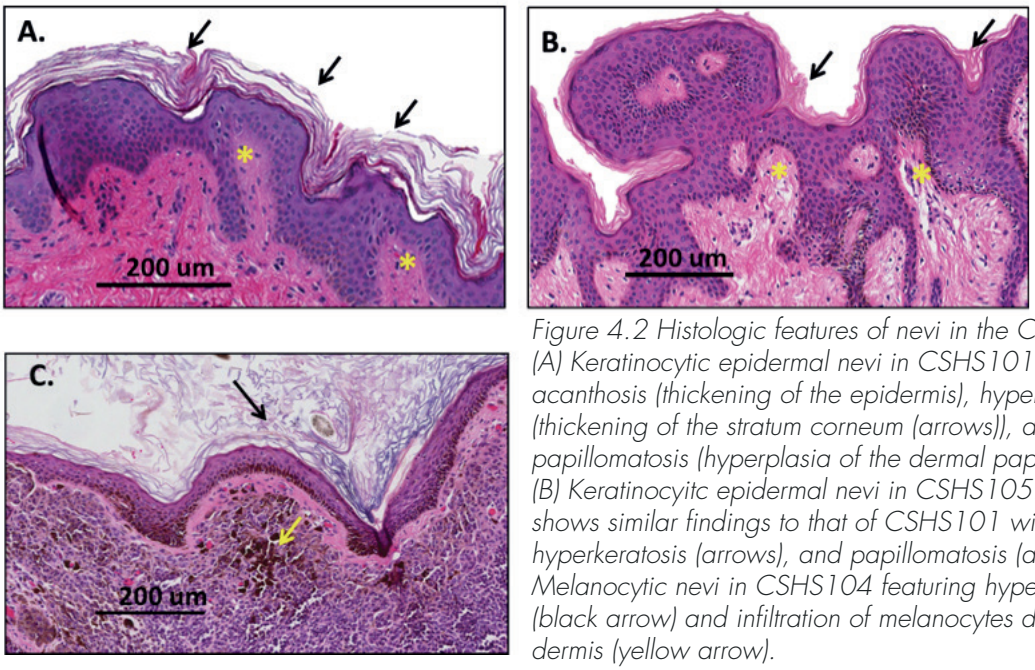

Figure 4.2 Histologic features of nevi in the CSHS cohort. (A) Keratinocytic epidermal nevi in CSHS101. Image shows acanthosis (thickening of the epidermis), hyperkeratosis (thickening of the stratum corneum (arrows)), and papillomatosis (hyperplasia of the dermal papillae (asterisks)). (B) Keratinocyitc epidermal nevi in CSHS105. The image shows similar findings to that of CSHS101 with acanthosis, hyperkeratosis (arrows), and papillomatosis (asterisks). (C) Melanocytic nevi in CSHS104 featuring hyperkeratosis (black arrow) and infiltration of melanocytes deep in the dermis (yellow arrow).

Table 4.2 CSHS cohort mineral panel

Subject, age (years)	Blood Phosphate*	Blood FGF23**	Alkaline phosphatase	25-OH-Vitamin D	1,25-OH_2-Vitamin D	TRP	Blood calcium	PTH
CSHS101, 6	2.6 mg/dl (4-5.4)	445 pg/ml (10-50)	308 U/L (96-297)	29 ng/ml (33-100)	8 pg/ml (24-86)↓	TRP 72%	2.4 mmol/L (2.15-2.55)	15.9 pg/ml (15-65)
CSHS102, 12	2.3 mg/dl (3.3-5.4)	279 RU/ml (<150)	366 U/L (70-280)	24ng/ml (33-100)	NR	LOW	9.7 mg/dl (8.8-10.8)	47 pg/ml (8.5-72.5)
CSHS104, 3	1.5 mg/dl (3.9-6.5)	795 RU/ml (<150)	1085 U/L (108-317)	17 ng/ml (10-80)	10 pg/ml (24-86)	TRP 80%	2.1 mmol/L (2.15-2.55)	67 pg/ml (15-65)
CSHS105, 16	2.6 mg/dl (2.8-4.6)	74 pg/ml (10-50)	283 U/L (52-171)	27 ng/ml (33-100)	69 pg/ml (24-86)	TRP 84%	2.2 mmol/L (2.15-2.55)	47 pg/ml (15-65)
CSHS106, 13	1.3 mg/dl (3.3-5.4)	176 pg/ml (10-50)	1186 U/L (50-162)	19 ng/ml (33-100)	37 pg/ml (24-86)	TRP 79%	2.3 mmol/L (2.15-2.55)	52 pg/ml (15-65)

*Phosphate reference ranges are adjusted for age and sex. Alkaline phosphatase reference ranges are adjusted for age.
** FGF23 was measured with an intact FGF23 assay in CSHS101, 105 and 106 and an a total FGF23 assay, which measures FGF23's intact and the C-terminal fragments, in CSHS102 and 104. These assays have different reference ranges.

4.1.4.3 Fractures and skeletal deformities

All subjects had a history of fractures. CSHS104 and 106 experienced multiple low impact fractures in areas with evidence of dysplasia. CSHS101 and 105 had a history of high-impact fractures in areas without dysplasia. However, in the case of CSHS105, pseudofractures were identified in imaging studies (Figure 4.3). CSHS102, 105 and 106 had scoliosis, which was especially severe in the case of CSHS106 (Figure 4.3). All subjects had some kind of skeletal deformity such as limb bowing and leg-length discrepancy secondary to rickets/osteomalacia and/or skeletal dysplasia (Table 4.1).

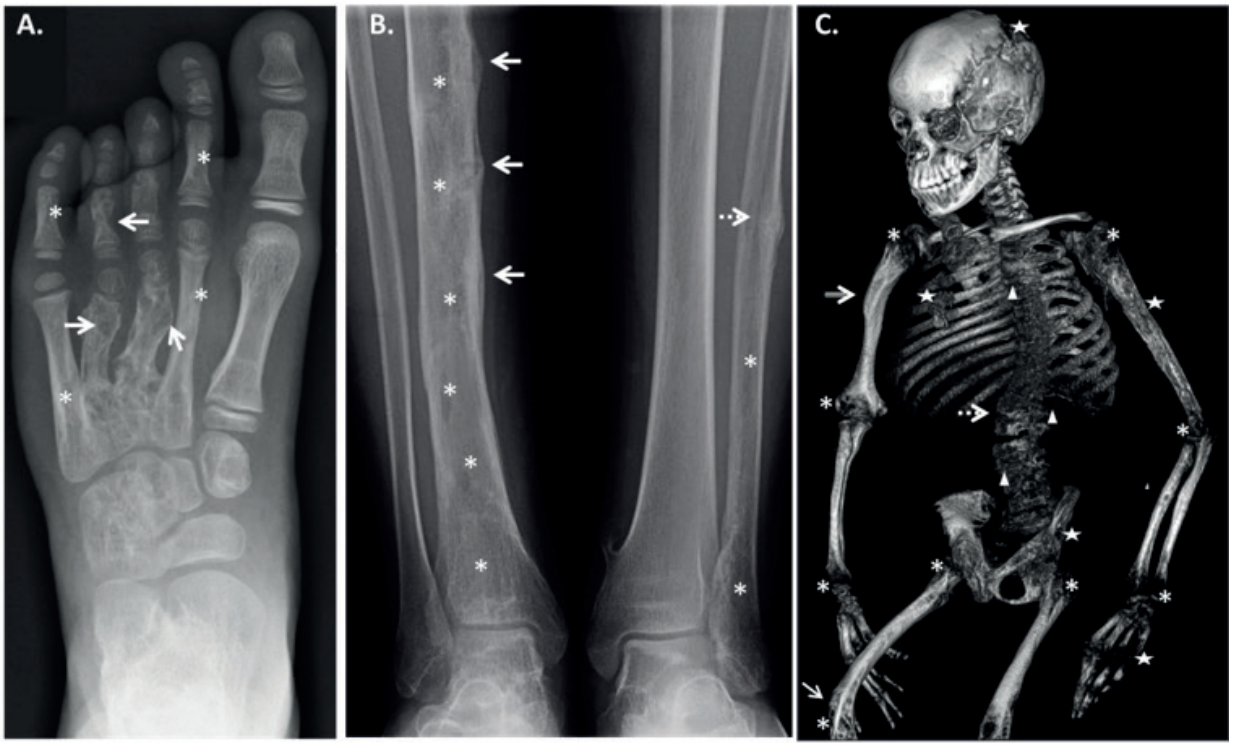

Figure 4.3 Representative X-ray imaging of the CSHS cohort. (A) CSHS101 left foot radiograph showing dysplastic lesions in phalanges and metacarpals of digits 2-5. In contrast, the bones of the first digit are spared from dysplasia consistent with the syndrome's mosaic nature. Dysplastic bone lesions are characterized by areas of mixed lytic/sclerotic areas. In this radiograph the lytic component is more prominent in digits 3 and 4 (arrows), while the sclerotic component is more noticeable in digits 2 and 5 (asterisks). (B) Radiograph of mid and lower shafts of tibiae and fibulae in subject CSHS105. The right tibia shows cortical stress pseudofractures with periosteal reaction along the mid shaft (arrows) in addition it to irregular lucent changes indicative of dysplasia (asterisks). A healing stress fracture is also observed in the mid left fibula (spotted arrow) with lucent changes in its mid and distal shaft (asterisks). The left tibia appears normal and unaffected suggesting that dysplastic bones are more prone to fracture under the same systemic abnormalities than non-dysplastic bones. (C) Skeletal 3-D CT reconstruction of CSHS106 skeleton showing severe rickets (asterisks) and lower limb bowing (arrow) secondary to osteomalacia. Patchy areas with lytic lesions are seen throughout the skeleton (stars) in addition to areas of sclerosis (compound arrow). This was the only patient in the cohort in which vertebral dysplasia was identified (triangles). Scoliosis, a frequent manifestation in CSHS, was severe in this patient (spotted arrow).

4.1.4.4 X-ray imaging

Radiographs and CT scans demonstrated a broad skeletal phenotype that included dysplastic foci of mixed lytic and sclerotic bone, cortical irregularities, and classic rachitic features (Figure 4.3). Fractures and pseduofractures were observed in CSHS102, 104 and 105 and were detected more frequently in areas of skeletal dysplasia

4.1.4.5 Nuclear medicine imaging

The octreoscans performed on subjects CSHS101, 104 and 105 did not reveal any well-defined uptake suggestive of a phosphaturic mesenchymal tumor or any other neuroendocrine tumor (Figure 4.4). The Na18F bone scan performed on CSHS106 revealed variable degrees of radiotracer uptake in areas of radiographically visible osteomalacia and skeletal dysplasia (Figure 4.4).

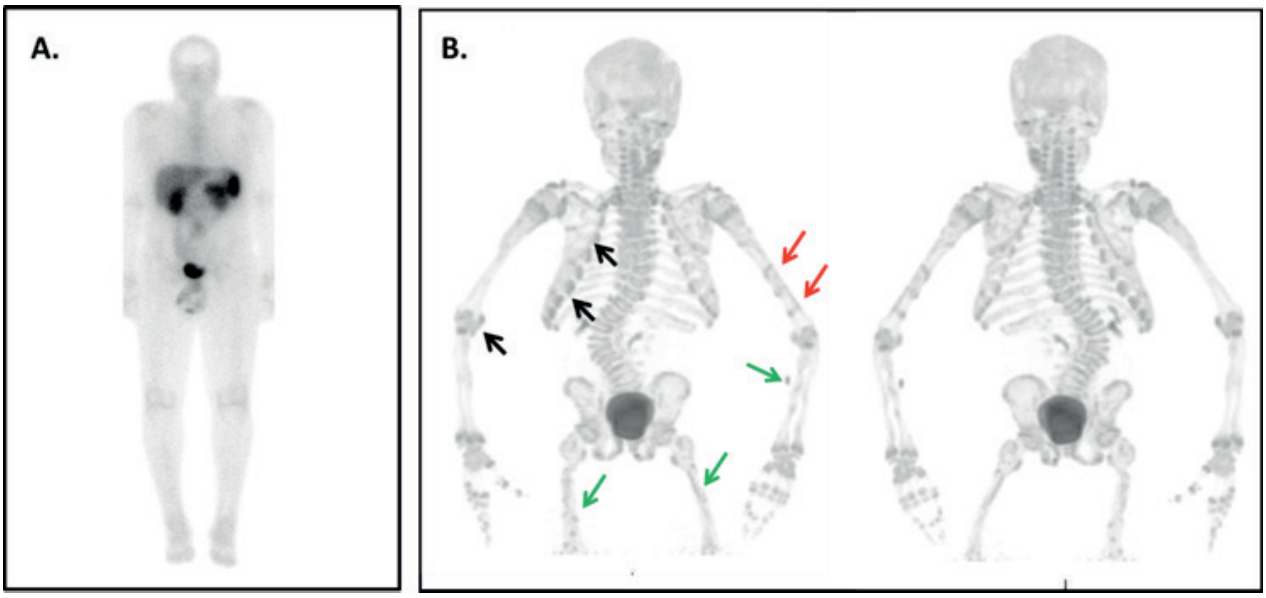

Figure 4.4 Nuclear imaging in the CSHS cohort. (A) Octreoscan in CSHS105. No pathological uptake was observed in this patient nor in subjects CSHS101 and 104. (B) 18F-Sodium Fluoride scan in CSHS106 in front (right) and back views (left). The bone scan reveals areas of variable uptake indicating rickets (black arrows), fractures (red arrows) and skeletal dysplasia (green arrows).

4.1.4.6 Distribution of skeletal lesions

The location and laterality of dysplastic skeletal lesions were compared with coexistent skin lesions. CSHS101 and 102 had unilateral nevi with ipsilateral bone lesions, CSHS105 had unilateral nevi with bilateral dysplasia, and CSHS104 and 106 had bilateral nevi and bilateral dysplasia. In this small cohort there was no association between the sidedness of skin or bone lesions. Both the appendicular and axial skeletons were affected in all subjects in the cohort. The pelvis and skull were the most commonly involved areas of the axial skeleton. Vertebral involvement was identified only in CSHS106.

4.1.4.7 Bone histology

Histologic examination of a rib specimen from subject CSHS104, in which mutation presence had been verified [61], revealed fibroblast-like spindle-shaped cells surrounded by a relatively dense collagen matrix. In addition, Masson's trichrome stain demonstrated extensive osteoid accumulation (figure 4.5). Severe osteoid accumulation was also observed in the plastic-embedded bone specimen from the iliac crest in subject CSHS105, although H&E staining of the same specimen did not demonstrate evidence of other abnormal findings (Figure. 4.6).

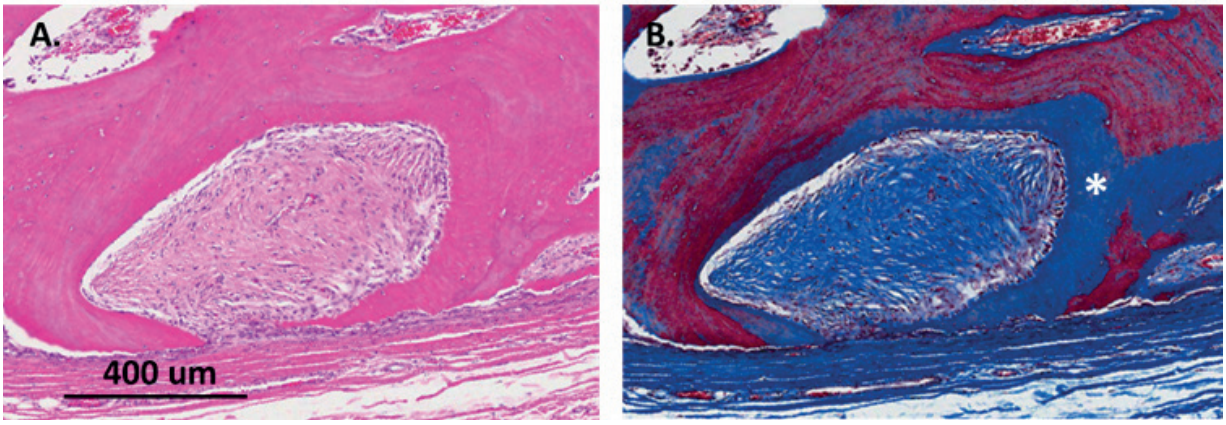

Figure 4.5 Histopathology of CSHS104 bone. (A) H&E of a rib. Islands of fibrous cells arising from the periosteum, such as the one observed in the image, were frequently encountered in the bone of this patient. Because the mutation had been verified in this area we speculated that perhaps this could be the histopathology of the skeletal dysplasia in CSHS. (B) Masson trichrome of the same section shows abundance of unmineralized collagen (blue) in the bone (asterisks) vs previously mineralized tissue (red) reflecting osteomalacia.

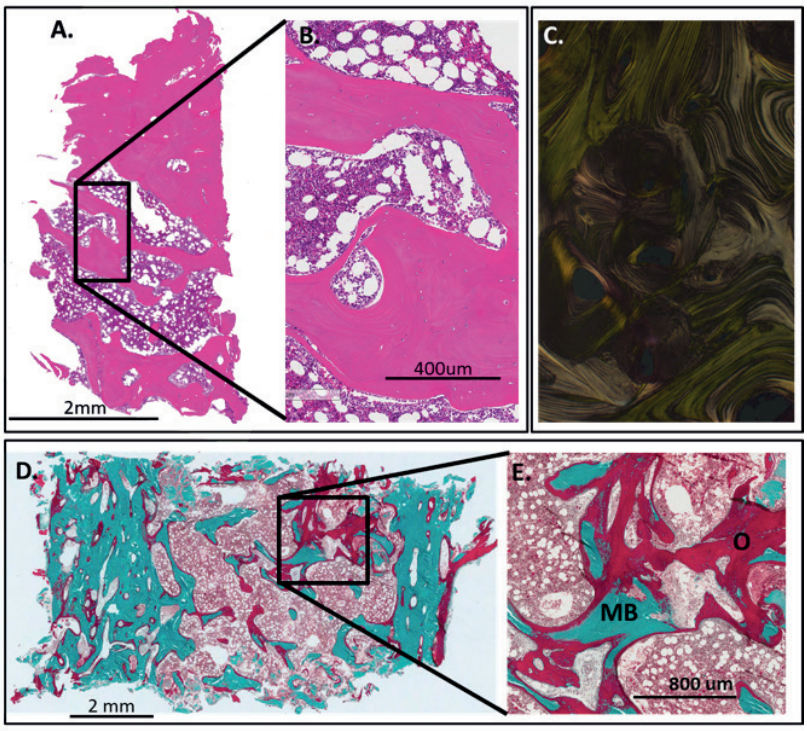

Figure 4.6 Histopathology of CSHS105 bone. An iliac crest biopsy was performed in an area that appeared dysplastic on imaging in this subject and in which mutation presence had been verified. (A-B). H&E of the iliac crest does not exhibit any noticeable histopathological abnormality. (C) Polarized light shows normal lamellar distribution of the collagen fibrils of sample shown in A-B. (D-E) Goldner trichrome stain of an undecalcified sample of the biopsy show areas with excessive accumulation of osteoid indicative of severe osteomalacia. O (red)= osteoid; MB (green): mineralized bone

4.1.4.8 Bone histomorphometry

Histomorphometric analysis corroborated the presence severe osteomalacia in a mutation-bearing region of subject CSHS105's iliac crest. Further, other indices showed minor alterations such as slightly increased trabecular thickness, trabecular number, mineralizing surface, or decrease in cortical thickness and trabecular separation (Table 4.3)

Table 4.3. 2-D histomorphometry in CSHS105's iliac crest biopsy

2-D Histomorphometric indices (units)	Results	Normal reference (mean ± SD)
osteoid volume/bone volume (%)	59	(1.48 ± 0.93)
total osteoid surface (%)	69.4	(12.1 ± 4.64)
bone volume/total volume (%)	27	(23.2 ± 4.37)
trabecular thickness (μm)	125	(133 ± 22)
trabecular separation (μm)	338	(570 ± 99)
trabecular number (trabeculae/mm)	2.16	(1.75 ± 0.23)
cortical thickness (μm)	783	(1202 ± 314)
eroded surface (%)	2.44	(4.09 ± 2.33)
mineralizing surface (%)	19	(9.7 ± 4.9)
bone formation rate ($\mu m^3/\mu m^2$/year)	49	(35.8 ± 8.9)

4.1.4.8 Tissue ELISA

FGF23 was not detected in the supernatant derived from subjects CSHS101 and 105's pulverized nevi or from thyroid tissue (negative control). In contrast, FGF23 levels were elevated in the supernatant from the 2 PMTs (positive controls) (Figure 4.7).

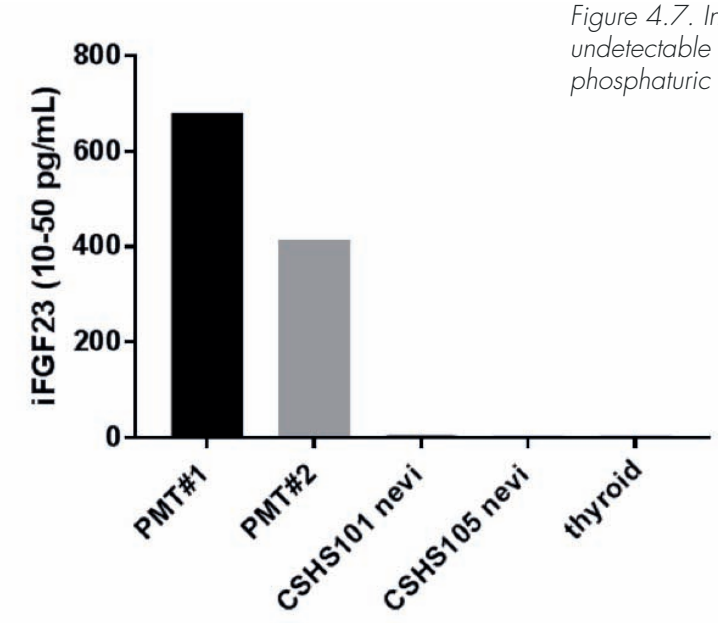

Figure 4.7. Intact FGF23 tissue ELISA. FGF23 was undetectable in the supernatants of CSHS nevi. PMT: phosphaturic mesenchymal tumor.

4.1.4.9 Mutation analysis in CSHS105 bone

Fifteen BMSC clonal colonies were isolated from the initial single cell suspension and were used for genetic evaluation. Sequencing of the colonies confirmed the presence of the *HRAS* G13R mutation in approximately 5 out of the 15 colonies (Figure 4.8).

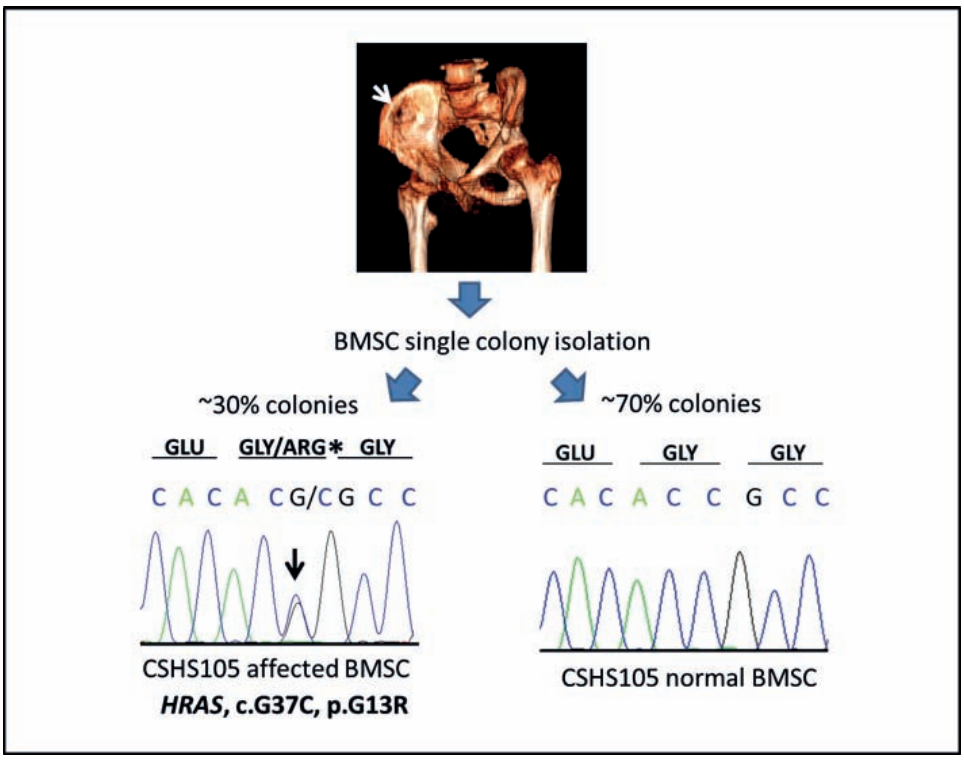

Figure 4.8 Mutation analyses in CSHS105 bone. An iliac crest biopsy was performed in subject CSHS105 at age 17 in an area that appeared dysplastic on CT imaging (white arrow). Bone marrow stromal cells (BMSCs) single colony isolation was performed on a piece of the biopsy. Sanger sequencing of colonies showed that approximately 30% of the BMSC colonies from this bone specimen had a HRAS G37C nucleotide substitution in one of the DNA strands (black arrow) leading a HRAS G13R mutation (asterisk), the same mutation that the subject harbored in his nevi. In contrast, the remaining colonies were unaffected (right chromatogram). NOTE: The sequences read in a 3'– 5' direction

4.1.4.10 Response to treatments for hypophosphatemia

Oral phosphate and calcitriol were prescribed to all subjects in an effort to treat hypophosphatemia and related symptoms. Doses varied accordingly to the severity of hypophosphatemia and symptoms e.g. subject CSHS104, who had not been able to ambulate by age 3 due to muscle weakness secondary to very severe hypophosphatemia, was treated with oral phosphate 130 mg/kg and calcitriol 0.2 mcg/kg. In contrast, in subject CSHS105, who had not experienced symptoms of hypophosphatemia until age 12 and showed much milder mineral abnormalities, very low doses of oral medication, i.e. calcitriol 0.003 mcg/kg and phosphate 5 mg/kg, were enough to alleviate bone pain and weakness. When the subjects were adherent to the prescribed doses, all experienced significant symptomatic and/or biochemical improvement, e.g. healed rickets in CSHS101, decreased pain and weakness in CSHS105, initiation of ambulation in CSHS104, and improved biochemical parameters in CSHS106. In CSHS102, mineral abnormalities appeared less responsive to treatment during childhood, but improved dramatically during adolescence.

Nevi removal has been postulated as a potential therapy for hypophosphatemia. Because of that, subjects CSHS101 and 102 had been subject to extensive CO2 laser ablation and surgical excision, respectively, prior to the NIH admission. However, these interventions did not modify phosphate homeostasis or hypophosphatemic symptoms.

4.1.4.11 Skeletal disease course

Resolution of biochemical abnormalities, alleviation of hypophosphatemia-related symptoms, and increase in BMD occurred in CSHS105 at age 17 (Figure 4.9). Similarly, CSHS102 experienced a decrease in fracture rate with improved response to medication at age 12. The findings in these two subjects were suggestive of age-related regression of skeletal/mineral homeostasis abnormalities in CSHS.

4.1.5 Extra-osseous/extra-cutaneous manifestations

Findings, including benign tumors, were found in non-osseous /non-cutaneous tissues in all the subjects from the cohort. Dental abnormalities were not observed. These findings are listed in Table 4.1, and representative images displayed in Figure 4.10. Except for CSHS104's pericardial effusion, none of these manifestations were symptomatic and were only identified because they were readily apparent (e.g. ocular dermoid in CSHS104, and hemibody asymmetry in CSHS105 and 106), or because they were detected through the imaging techniques described in section 3.1.3.

No hematological abnormalities were found except in CSHS104 in whom anemia and thrombocytopenia of undetermined etiology were detected (table 4.4). Hematologic evaluation was performed for this reason. Their differential diagnosis included: hemoglobinopathy, poor bone marrow environment secondary to severe rickets, heavy metal toxicities, and severe iron deficiency. The latter was discarded after the iron studies were ordered and retrieved normal results (data not shown). A hemoglobinapthy screen, a bone marrow aspirate, and a lead level were recommended for diagnostic purposes but were not performed during her admission.

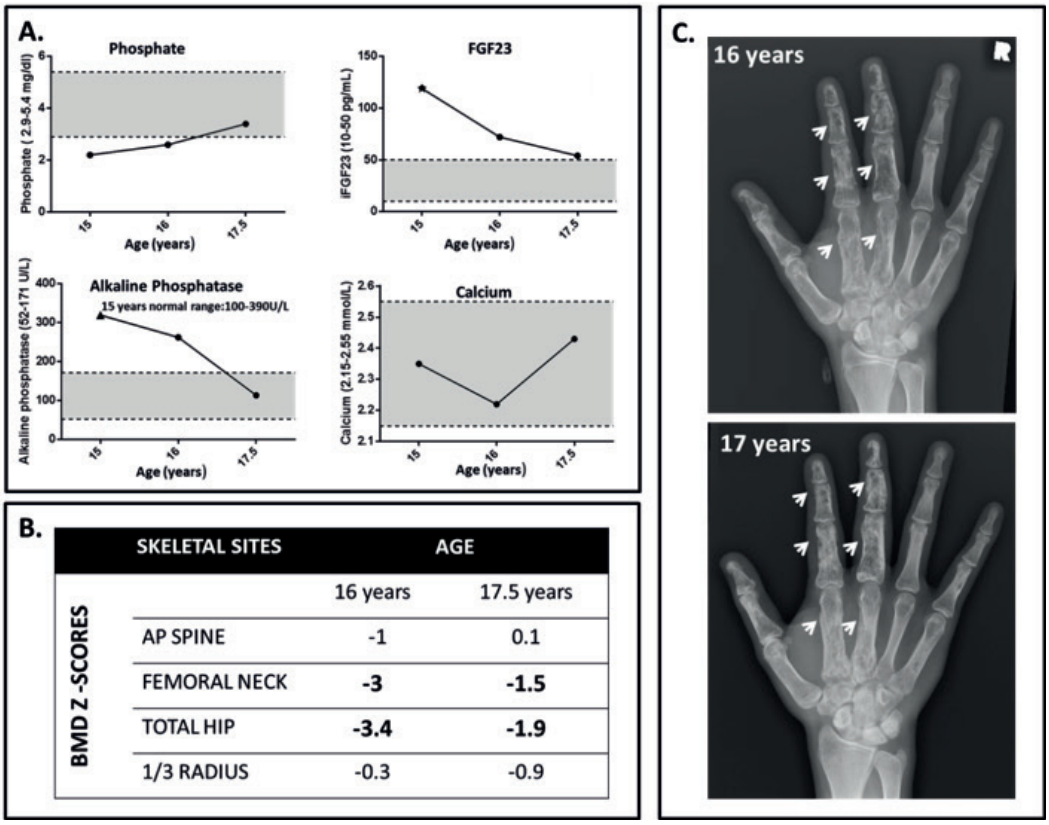

Figure 4.9 Changes in mineral metabolism and radiographic findings in CSHS105 following treatment with phosphate and calcitriol. (A) Fasting biochemistries, measured when off medication for at least 48 hours, had normalized by age 17.5 years. Shaded areas denote normal ranges for a 17 year-old. (B) Bone mineral density (BMD) Z-scores by DXA increased from baseline at age 16 to age 17.5 (C) Dysplastic skeletal lesions appeared more radio dense at age 17 vs age 16 (arrows), consistent with an increase in mineral deposition in the dysplastic bone.

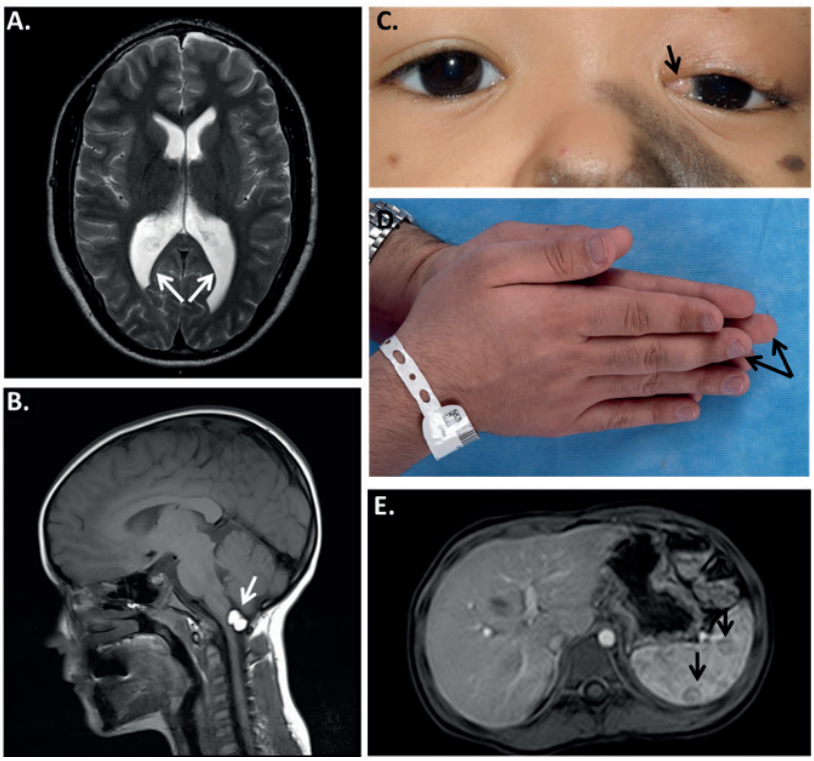

Fig 4.10. Examples of extra-osseous/extra-cutaneous manifestations in the CSHS cohort. (A) Enlarged posterior horns of the lateral ventricles in CSHS105 (arrows). (B) Intracranial lipoma in CSHS101 (arrow). (C) Limbal dermoid in CSHS104 (arrow). (D) Hemibody asymmetry in CSHS105. (E). Splenic hemangiomas in CSHS101 (arrows).

Table 4.4 CSHS104 hematological profile

Hematological parameter	Value (normality ranges)
Red blood count	2.98 (3.84-4.92 M/uL)↓
Hemoglobin	7.7 (10.2-12.7 g/dL)↓
Mean corpuscular volume	83.6 (72.3-85 fL)
Red cell distribution width	22.1 (11.7/14.4%)↑
Platelets	38 (189-394 K/uL)↓
White blood count	4.69 (4.86-13.2 K/uL)

Positive antiplatelet antibodies were identified, which could explain the thrombocytopenia. A bone marrow aspirate was eventually performed but did not reveal abnormalities. Significant splenomegaly with fibrosis and extramedullary hematopoiesis were detected in her autopsy (a year and a half after her admission at the NIH) but the etiology these abnormalities was never elucidated.

4.2 Literature review

4.2.1 Literature search results

The literature search retrieved 39 reports that described 44 subjects with findings compatible with CSHS [50-56, 61, 62, 160-189]. Seven additional reports were identified from references of the reports retrieved [190-196]. This resulted in a total of 46 reports with 51 subjects, which were included in the literature review.

4.2.2 Demographic information

Sixty-one percent of the subjects were male. Ethnic backgrounds were diverse (Table 4.5).

4.2.3 Cutaneous nevi

A similar spectrum of cutaneous findings to those observed in the CSHS cohort was identified in the literature review, with EN affecting 31/51 subjects (61%) [51, 53-55, 61, 62, 161, 162, 167-178, 182, 183, 186-189, 192, 193]; PPK 16/51 (31%), [51, 52, 56, 160, 163, 164, 166, 179, 180, 184-186, 190, 191, 194, 195], and giant CMN 4/51 (8%) [50, 162, 165, 181] (Figure 4.1 F).

Table 4.5 Sex and Ethnicity in CSHS published reports

Sex		
Male	31/51 (61%)	
Female	20/51 (39%)	
Ethnicity		References
Caucasian	22/51 (43%)	[51-53, 56, 160, 161, 167, 168, 170, 171, 173, 175, 177, 178, 182, 187-193]
Asian	8/51 (16%)	[54, 167, 172, 174, 181, 184, 194, 195]
South Asian	5/51 (10%)	[50, 55, 165, 169, 179]
Middle Eastern	5/51 (10%)	[51, 62, 164, 180, 185]
Latin American	4/51 (8%)	[163, 186]
Black	2/51 (4%)	[61, 167]
Unclear	5/51 (10%)	[161, 164, 167, 177]

4.2.4 Mineral abnormalities and skeletal dysplasia

4.2.4.1 Biochemical profile

Published reports in which biochemistries were provided showed results consistent to that of our cohort, except for the 7 patients in whom phosphate was within the normal range (see section 4.2.4.2) (Table 4.6). FGF23 levels were measured and resulted elevated in the 6 subjects from the literature in whom it was assessed [50, 52, 54, 55, 61, 62].

4.2.4.2 Co-existance of hypophosphatemia and skeletal dysplasia

The presence of both low blood phosphate and focal bone lesions was observed in 26/51 subjects described in the literature [50-53, 55, 61, 62, 160, 162, 164, 166, 167, 170, 172, 173, 175-177, 182-184, 188, 191, 195]. In 18 of the 25 remaining reports, hypophosphatemia and/or rickets was reported without mention of skeletal dysplasia, and/or radiographs were either not provided, or did not demonstrate dysplasia [51, 54, 56, 162, 163, 165, 168, 169, 171, 174, 179-181, 185, 186, 194]. Seven of fifty-one reports described dysplastic lesions on radiographs, but serum phosphate was either not reported [187, 189, 190, 192, 193], or was within the normal age-related normal range at the time of the report [161, 178].

4.2.4.3 Symptomatic onset

The mean age of onset of symptoms related to hypophosphatemia in the published reports was 4 years (median 2.7 years, SD 3.6, range 1-14 years). The most common initial symptoms were similar to our cohort and included bone pain, limb-length discrepancy, bone deformities, and impaired mobility. Four subjects [56, 167, 171, 175] had no evidence of rickets or hypophosphatemia in early childhood, but developed these conditions later in childhood, suggesting that systemic mineral abnormalities are not necessarily congenital in CSHS.

4.2.4.4 Fractures and deformities

Fractures and deformities were common in CSHS reports. Fractures were reported in 29/51 subjects (57%) in the literature [51-54, 56, 61, 62, 160-164, 167, 168, 170, 172-175, 177, 182, 183, 188-190, 193-195], and occurred most frequently in areas of dysplastic bone. Limb deformities, predominantly bowing, were reported in 36/51 (70%)[50-53, 55, 56, 61, 160, 162, 163, 165-170, 172, 173, 175, 177-181, 184-186, 188, 189, 193-195]. Scoliosis was described in 21/51 (41%) [50, 53, 56, 61, 160, 162-164, 166-168, 170, 172, 175, 178, 179, 181, 186, 187, 190, 193, 194]

4.2.4.5 Skeletal imaging

Literature reports of dysplastic bone lesions were similar to those in our cohort, and were often described as "radiolucent," "sclerotic," "cyst-like," "lytic," and/or "fibrous dysplasia-like." Bone mineral density has not been reported in any of the subjects from the literature.

Table 4.6 Mineral panel in CSHS published reports

	Subject (CSHS# or author, age (years), sex)	Blood phosphate	Blood FGF23*	Alkaline phosphatase	25-OH-Vitamin D	1,25-OH_2-Vitamin D	TRP or TmP/GFR	Blood calcium	PTH	Primary renal tubulopathy	Ref.
Subjects from the literature in whom FGF23 was assessed	Narazaki et al. 5/F	2.1mg/dL (3.8-5.8)	123 pg/ml (10-50)	1935 U/L (330-880)	16 pg/ml	32 pg/ml (20-40)	TmP/GFR 1.9 mg/dl (4.7-5.6)	9.9 mg/dL	61 pg/mL (15-65)	NR	[174]
	Sethi et al. 5/M	2.1 mg/dl (3.5-5.5)	1265 pg/ml (10-50)	NR	55nMol/L (>50)	NR	TmP/GFR 1.5mg/dl (2.9-4.6 mg/dl)	10.9mg/dl (9-11)	338 pg/ml (10-60)	No	[55]
	Lim et al. CSHS103 15/F	1.5mg/dl (3.3-5.4)	524 RU/ml (<150)	651 U/L (30-120)	LOW	NR	LOW	9.3 mg/dl (9-10.5)	90 pg/ml (10-60)	No	[61]
	Hoffman et al. 16/M	1.9 mg/dl (3.5-5.2)	530 RU/ml (<150)	534 U/L	36 (10-55ng/ml)	48 pg/ml (21-65)	TmP/GFR 1.6 mg/dl (3.2±0.3)	9.8 (8.5-10.2)	45 pg/ml (10-65)	No	[54]
	Aggarwal et al. 10/M	2.1 mg/dl (2.1-4.5)	171RU/ml (<150)	2685 U/L (240-840)	69ng/ml	NR	TRP 73%	8.7 (8.1-10.4)	127.7 pg/ml	No	[50]
	Avitan-Hersh et al. 14/M	1.9 mg/dl (3.6-5)	69pg/ml (10-50)	NR	7ng/ml (>30)	21 pg/ml (25-76)	TRP 96%	9.8 (8.5-10.6)	62ng/L(15-65)	No	[62]
	Heike et al. 19/M	2.2 mg/dl (4.3-5.7)	215 RU/ml (<150)	1103 U/L (133-347)	12 (13-67ng/ml)	19 (27-71 pg/ml)	TmP/GFR 1.5 mg/dl (2.5-4.2)	9.4 (9.4-10.6)	51 (11-47 pg/ml)	No	[52]

Abbreviations: NR: Not reported, TRP: renal tubular reabsorption of phosphate; TmP/GFR: Tubular maximum Phosphate Reabsorption per Glomerular Filtration Rate.
Normal ranges for serum phosphate in our cohort are adjusted to the age of the subject.
Serum FGF23 values are displayed as intact (pg/ml) or total value (intact plus C-terminal fragments) RU/ml.
Normal ranges for biochemical parameters in subjects from the literature are displayed as reported.

Table 4.6 Mineral panel in CSHS published reports

	Subject (CSHS# or author, age (years), sex)	Serum phosphate	Serum FGF23*	Alkaline phosphatase	25-OH-Vitamin D	1,25-OH_2-Vitamin D	TRP or TmP/GFR	Serum calcium	PTH	Primary renal tubulopathy	Ref.
Subjects from the literature in whom FGF23 was assessed	Moreira et al. 1/F	1.9mg/dl (3-6.5)	NR	1192 U/L (54-280)	normal	NR	LOW	normal	normal	No	[173]
	Kishida et al. 7/F	2.1 mg/dl (4.5-6.5)	NR	270 U/l (<116)	NR	NR	LOW	9.8 mg/dl (8.5-10.5)	normal	No	[170]
	Chou et al. 6/M	1.5 mg/dl (3.7-5.6)	NR	1041 U/L (145-420)	8.94 ng/ml (9.7-41.7)	NR	TRP 80%	9.5 mg/dl (8.8-10.8)	94.6 pg/ml (10-65)	No	[162]
	Chou et al. 22/M	1.5 mg/dl (2.9-5.4)	NR	437 U/L (70-230)	NR	NR	TRP 91%	9.7mg/dl	35.3 (10-65)	No	[162]
	Olivares et al. 2.5/F	0.4mmol/L (0.9-1.75)	NR	350 U/L (37-200)	70 nmol/L (37-200)	21.6 pmol/L (35-105)	TRP 42%	9.2 mg/dl (8.8-10.8)	NR	No	[175]
	Ivker et al. 1/F	0.87 mmol/L (1.54-2.62)	NR	420 (U/L) 50-136)	normal	36 nmol/L (36-144)	TRP 68.5%	normal	28 ng/L (51-217)	NR	[168]
	Oranje et al. 4/M	0.7 mmol/L (1-1.8)	NR	453 U/L (80-225)	100umol/L (31-129)	46 nmol/L (40-140)	TRP 86%	normal	2.2 pmol/L (0.8-15)	No	[177]
	Tokatli et al. 5/M	1.7 mg/dl	NR	25 U/L	NR	NR	NR	10.6 mg/dl	NR	NR	[185]
	Stosiek et al. 20/M	2.4 mg/dl (low-normal)	NR	304 U/L (high)	21.4 ng/ml (N)	11pg/ml (10-16)	TRP 87%	9.2 mg/dl	5.3 pmol/L (normal)	NR	[183]
	O'Neill et al. 3/F	1.1 mmol/L	NR	600 U/L	NR	NR	NR	8.4 mg/dl	NR	NR	[176]
	Skokby et al. 1/M	0.54 mmol/L (1.24-1.84)	NR	1472 U/L (250-1000)	NR	91 pmol/L (24-158)	TRP 37%	normal	normal	No	[182]
	Carey et al. 7/M	2.6 mg/dl	NR	832 IU/L	34.4 ng/ml (15-80)	4.3 pg/ml (21-74)	TmP/GFR 1.58 mg/dl (4-5.9)	9.3 mg/dl	0.9 ng/ml (0.4-1.5)	No	[51]
	Carey et al. 23/F	1.2 mg/dl	NR	306 IU/L	18 ng/ml (15-80)	8.7 pg/ml (19-50)	TmP/GFR 0.64 mg/dl (2.5-4.2)	8.8 mg/dl	0.8 ng/nl (0.4-1.5)	No	[51]

Abbreviations: NR: Not reported, TRP: renal tubular reabsorption of phosphate; TmP/GFR: Tubular maximum Phosphate Reabsorption per Glomerular Filtration Rate.
Normal ranges for serum phosphate in our cohort are adjusted to the age of the subject.
Serum FGF23 values are displayed as intact (pg/ml) or total value (intact plus C-terminal fragments) RU/ml.
Normal ranges for biochemical parameters in subjects from the literature are displayed as reported.

Table 4.6 Mineral panel in CSHS published reports

	Subject (CSHS# or author, age (years), sex)	Serum phosphate	Serum FGF23*	Alkaline phosphatase	25-OH-Vitamin D	1,25-OH_2-Vitamin D	TRP or TmP/GFR	Serum calcium	PTH	Primary renal tubulopathy	Ref.
Subjects from the literature in whom FGF23 was assessed	Sugarman et al. 12/F	2.5 mg/dl (3-5.5)	NR	210 U/L (30-130)	NR	NR	NR	8.9 mg/dl (9-11)	NR	moderate aminoaciduria	[195]
	Moorjani et al. 8/F	2.5 mg/dl	NR	350 IU/L	NR	NR	NR	9.5 mg/dl	NR	trace of amino acids	[172]
	Aschinberg et al. 12/M	1.3 mg/dl (2.5-5)	NR	313 IU/L (20-124)	NR	NR	TRP 35%	9.6 mg/dl (9-11.5)	523 pg/ml (275-675)	No	[56]
	Hosalkar et al. 7/M	1.1 mg/dl (2.5-5)	NR	340 IU (20-124)	18 ng/ml (15-80)	6 pg/ml (20-75)	TRP 40%	8.9 mg/dl (9-11.5)	0.8ng/ml (0.4-1.5)	NR	[67]
	Hosalkar et al. 6/M	1.3 mg/dl (2.5-5)	NR	330 IU (20-124)	12 ng/ml (15-80)	9 pg/ml (20-75)	TRP 35%	8.8 mg/dl (9-11.5)	0.9ng/ml (0.4-1.5)	NR	[67]
	Hosalkar et al. 3/M	1.8mg/dl (2.5-5)	NR	210 IU (20-124)	14 ng/ml (15-80)	11 pg/ml (20-75)	TRP 46%	9.1 mg/dl (9-11.5)	0.5ng/ml (0.4-1.5)	NR	[67]
	Rustin et al. 35/M	Low/ normalized	NR	NR	NR	NR	NR	normal	normal	NR	[88]
	Sukkhojaiwaratkul et al. 4/F	0.6mmol/L (1.2-1.8)	NR	2877 (169-372 U/L)	61nmol/L (>50)	NR	TRP 75%	9.2mg/dl	12.5pmol/l (3.7-15.9)	NR	[84]
	Shahgholi et al. newborn/F	1.9mg/dl (3.5-6)	NR	3300 U/L (45-300)	normal	NR	NR	normal	NR	NR	[80]
	de Morais et al. 9/F	LOW	NR	1630 U/L (175-420)	normal	NR	NR	normal	normal	NR	[63]
	Feldelmann et al. 19/F	0.43 mmol/L (1.11-1.5)	NR	107 U/L (30-90)	86ng/ml (5-70)	26 pg/nl (15-20)	TRP 51%	normal	0.15ng/ml (<0.5)	normal	[64]
	Shieh et al. 9/M	1.3mg/dl	NR	NR	NR	NR	67%	normal	0.78ng/ml (0.22-0.66)	NR	[81]

Abbreviations: NR: Not reported, TRP: renal tubular reabsorption of phosphate; TmP/GFR: Tubular maximum Phosphate Reabsorption per Glomerular Filtration Rate.
Normal ranges for serum phosphate in our cohort are adjusted to the age of the subject.
Serum FGF23 values are displayed as intact (pg/ml) or total value (intact plus C-terminal fragments) RU/ml.
Normal ranges for biochemical parameters in subjects from the literature are displayed as reported.

Table 4.6 Mineral panel in CSHS published reports

	Subject (CSHS# or author, age (years), sex)	Serum phosphate	Serum FGF23*	Alkaline phosphatase	25-OH-Vitamin D	1,25-OH_2-Vitamin D	TRP or TmP/GFR	Serum calcium	PTH	Primary renal tubulopathy	Ref.
Subjects from the literature in whom FGF23 was assessed	Zutt et al. 15-52/F	low/normalized	NR	high/normalized	NR	NRA	low/ normalized	normal	NR	normal	[53]
	Saraswat et al. 22/M	2.4mg/dl (2.5-4)	NR	46 U/dl (5-14)	NR	NR	phosphaturia	7.8mg/dl (8-11)	normal	NR	[179]
	Bouthors 52/M	0.67mmol/l	NR	normal	NR	NR	76%	normal	normal	NR	[160]
	Gathwala et al. 6/M	2.6mg/dl	NR	1976 U/L	normal	NR	phosphate urinary excretion 700mg/d (100-300)	8.7mg/dl	normal	normal	[165]
	John et al. 7/M	1.8mg/dl	NR	982 U/L	NR	NR	TmP/GFR 0.5mg/dl	9.6mg/dl	NR	normal	[169]
	Klein et al. 2/M	2.5mg/dl	NR		32.6 ng/ml (normal)	21.6pg/ml (normal)	79%	normal	35pg/ml (normal)	NR	[171
	Sanmanechai et al. 7/M	0.77mmol/L (1.19-1.8)	NR	630U/L (145-420)			64%	2.22mmol/L (2.2-2.7)	8.38pmol/l (0.95-6.84)	normal	[194]
Subjects with no reported mineral anomalies or no labs reported	Cabanillas et al. 26/M	normal	normal	normal	NR	normal	NR	normal	normal	NR	[161]
	Pierini et al. 9/M	4.9mg/dl normal	NR	NR	NR	NR	NR	9.5mg/dl (normal)	NR	NR	[178]
	Kaplan et a. 14/F	NR	NR	NR	NR	NR	NR	normal	normal	NR	[192]
	Grun 13/M	normal	NR	NR	NR	NR	NR	normal	NR	NR	[191]
	Camacho et al. 18//M	NR	NR	544 U/L (30-115)	NR	NR	NR	NR	NR	NR	[190]
	Bouwes 19/F	NR	NR	NR	NR	NR	NR	NR	NR	NR	[189]
	Vidaurri et al. x 3patients	NR	NR	NR	NR	NR	NR	NR	NR	NR	[186]
	Yu e tal. 9/M	NR	NR	NR	NR	NR	NR	NR	NR	NR	[187]

Abbreviations: NR: Not reported, TRP: renal tubular reabsorption of phosphate; TmP/GFR: Tubular maximum Phosphate Reabsorption per Glomerular Filtration Rate.
Normal ranges for serum phosphate in our cohort are adjusted to the age of the subject.
Serum FGF23 values are displayed as intact (pg/ml) or total value (intact plus C-terminal fragments) RU/ml.
Normal ranges for biochemical parameters in subjects from the literature are displayed as reported.

4.2.4.6 Distribution of skeletal lesions

In respect to the location and laterality of dysplastic bone and skin lesions in patients with unilateral skin lesions (n= 15), skeletal lesions were ipsilateral in 10/15 (67%) [51, 52, 161, 164, 166, 175, 182, 183, 187, 191], and bilateral in 5/15 (33%) [61, 62, 177, 188, 190, 195]. Bilateral nevi and bilateral skeletal lesions were reported in 5 patients [55, 160, 172, 192, 193], while bilateral skin lesions with unilateral skeletal dysplasia were described in 2 patients [178, 184].

Skeletal dysplasia was reported in all skeletal compartments. Both the appendicular and axial skeleton were affected in 16 patients from the literature [52, 61, 62, 160, 161, 164, 176-178, 183, 188, 190-193, 195, 196]. Dysplasia limited to the appendicular skeleton was described in 9 patients [51, 55, 162, 167, 172, 175, 182, 184, 187], while one report described dysplastic lesions exclusively in the axial skeleton [166]. The pelvis and the skull were the most commonly involved areas of the axial skeleton, whereas vertebral involvement was identified only in 2 patients from the literature [62, 190]. Therefore, a clear correlation between laterality of bone and skin lesions does not appear to exist, i.e. they appear to be developmentally independent events.

4.2.4.7 Bone histology

Bone biopsy specimens from 4 subjects were examined. Osteomalacia without any evidence of dysplasia was identified in 2 cases in which the biopsy was taken from areas that appeared dysplastic in imaging [62, 190], and in another case in which skeletal dysplasia was not radiographically detected [51] . Histomorphometry was not examined in any of these biopsies. "Hemangiomas" were described in the fourth biopsy in which osteomalacia assessment was not performed [183].

4.2.4.8 Response to treatments for hypophosphatemia

Treatment approaches and efficacy differed among the reported patients from the literature. Of the 26 patients treated with a combination of phosphate supplements and calcitriol (or other active vitamin D analogs), 19/26 (73%), experienced significant clinical improvement; e.g., resumed ambulation, decreased pain, healing of radiographic rickets [51, 55, 162, 164, 165, 167, 169, 173, 175, 177, 182, 184, 185, 194]. In 4/26 (15%) [52, 54, 168, 170], the initial response was not optimal but improved over time. In 2/26 (8%) efficacy appeared limited [162, 163]. Of the 11 patients treated with non-active vitamin D (ergo- or cholecalciferol) [50, 51, 56, 160, 166, 172, 176, 179, 181, 185], symptomatic improvement was reported in only 2/11(18%) [166, 176]. However, some of these patients underwent nevi removal in addition to phosphate and active vitamin D replacement. In an effort to avoid the potential confounding effect of nevi removal on the efficacy of oral medication, response to medication was also analyzed in patients who did not undergo nevi removal. In these patients, oral medication had an independent positive effect on symptoms and blood phosphate levels [51, 55, 162, 164, 165, 169, 170, 175-177, 182, 184, 186].

Twenty of fifty-one patients from the literature underwent surgical excision, dermabrasion, or CO_2 laser ablation of the nevi in an effort to correct the hypophosphatemia. Serum phosphate and hypophosphatemic symptoms were unchanged in 7/20 (35%) [162, 164, 170, 175, 177, 183], and improved in 12/20 (60%) [52-54, 166-168, 174, 179, 185, 194]. However, attribution of improvement in blood phosphate levels to skin lesion removal was confounded by the fact that phosphate and calcitriol/vitamin D were either not discontinued, and even initiated at the time of nevi removal. In two patients, a direct association between nevi removal and a subsequent increase in serum phosphate was suggested [56, 168].

4.2.4.9 Skeletal disease course

Evidence of clinical improvement in mineral metabolism (e.g., drug dose reduction, fracture cessation, resolution of hypophosphatemia) was reported in 10 patients from the literature, most of whom were over 17 years-old (Table 4.7). However, hypophosphatemia and/or osteomalacic manifestations persisted in 5 young adults (≤23 years) [51, 52, 164, 183, 190] and 1 older adult [160]. Of note, skeletal dysplasia remained apparent on imaging despite clinical improvement.

4.2.5 Extra-osseous/extra-cutaneous manifestations

A detailed list of extra-skeletal/extra-cutaneous abnormalities in the subjects from the literature is displayed in (Table 4.8). Neurological abnormalities were reported in 21/51 (41%) of the patients from the literature. Intellectual disability, developmental delay, ventricular enlargement and EEG abnormalities were the most frequent findings. Ophthalmological disorders, predominantly colobomas and ocular dermoids, were identified in 12/51 patients (24%). Body asymmetry was described (or observed in the images provided) in 12/51 patients (24%). Angiomatous malformations, and/or cardiac problems were also reported in 4/51 patients from the literature (8%). Precocious puberty occurred in 4/51 (8%) of the patients. Benign neoplasms were frequent, whereas malignant transformation was less common, albeit reported (5 malignant vs. 16 benign tumors) (Table 4.9). Interestingly, osteosarcoma has not been reported to date in association with CSHS.

Table 4.7 Reported CSHS cases of resolved/improved mineral abnormalities

Age at clinical improvement (years)	Indicator of decreased skeletal disease activity	Age at latest follow-up (years)	References
4	Improvement of rickets and hypophosphatemia at age 4	39	[166]
10	Insufficiency fracture cessation since age 10	19	[189]
12	Resolution of hypophosphatemia	13	[56]
17	Resolution of hypophosphatemia at age 17	35	[188]
17	Improved biochemical abnormalities. Increased BMD	17	[54]
18	Improved response to oral treatment after age 18	18	[170]
22	Insufficiency fracture cessation since age 22	32	[193]
22	Improved biochemical profile in adulthood	22	[179]
N/A	Insufficiency fracture cessation	26	[161]
27	Resolution of hypophosphatemia. Vitamin D stopped at age 27. Phosphorus status normal at age 52	52	[53]

Table 4.8 Extra-osseous/extra-cutaneous abnormalities in CSHS published reports

Affected system	Number of subjects	Manifestations
Neurological abnormalities	21	• Intellectual disability/delayed milestones (10 subjects): [51, 54, 164, 177, 186, 190, 194, 195, 197] • Bilateral/unilateral ventricular enlargement (7 subjects): [167, 175, 177, 182, 187, 190, 195] • Epilepsy/EEG abnormalities (5 subjects): [51, 177, 193, 195, 197] • Brainstem lipomas: (2 subjects): [161, 187] • Macrocephaly: (3 subjects): [178, 187, 192] • Brain atrophy (2 subjects):[175, 195] • Spastic hemiplegia (2 subjects): [193, 195] • Microcephaly (1 subject): [197] • Arachnoid cyst (2 subjects): [50, 175] • Partial third cranial nerve palsy (1 subject): [168]. • Hypoplastic right occipital bone (1 subject): [175]. • Dyslexia (1 subject): [187] • Nistagmus (1 subject): [161] • Hyperreflexia (1 subject):[161] • Interdigitation of gyri (1 subject): [169] • Brainstem tumor (non-lipoma) (1subject):[181]
Ophtalmological abnormalities	12	• Coloboma (5 subjects): [178, 187, 189, 192, 197] • Limbal dermoid (4 subjects): [176, 178, 187, 195] • Strabismus: (3 subjects): [53, 182, 197] • Corneal opacity: (3 subjects): [53, 187, 189] • Dermoid cyst of the eyelid: (1 subject): [163] • Scleral pigmented spots (1 subjects): [163]. • Ophtalmoplegia: (1 subject): [53] • Microcornea: (1 subject): [189] • Antimongoloid slant: (1 subject): [177] • Ptosis (1 subject): [177] • Corneal calcification (1 subject): [167]
Hemibody assymetry	12	• Hemihypertrophy nevi side (4 subjects): [179, 180, 191, 192] • Hemihypoplasia nevi side: (5 subjects): [52, 53, 171, 182, 193] • Asymmetrical facies (2 subjects): [177]: side non-specified plus asymmetric dentition, [62]: tongue asymmetry (side non-specified)

Affected system	Number of subjects	Manifestations
Cardiovascular abnormalities	4	• Pericardial effusion (1 subjects): [176] (due to pulmonary hemangiomatosis). • Aortic coarctation (1 subjects): [178] Heart valve abnormalities (1 subject): [167] (mild aortic regurgitation due to calcification of aortic valve), • Flat angioma (face)(1 subject): [191] • Lymphedema (1 subject):[178]
Precocious puberty	4	• Central precocious puberty (3 subjects): [168, 180, 187] • Not specified central/perif (1 subject): [53]
Thyroid abnormalities	1	• Thyroid medullary carcinoma (1 subject): [188]: diagnosed at 15years, no family history)
Hyper IgE	2	[54, 55]
Hematological abnormalities	1	Severe anemia (unknown etiology) (1 subject): [196]
Basal cell carcinoma	2	• Diagnose over 50 years: [53, 160]
Hyperparathyroidism	1	[55]
Congenital rhabdomyosarcoma	1	[180]
Testicular abnormalities	1	[178]
Giant cell granuloma of the maxilla	1	[192]
Pheocromocytoma	1	Detected incidentally at 54 [160]
Thymoma	1	*HRAS* mutation confirmed in timoma [62] Manifestations
Bladder leiomyoma	1	[186]
NO extra-osseous/ extra-cutaneous findings reported	15*	• [50, 51, 56, 162, 165-167, 170, 173, 183, 184, 186] • *Not reportedbut hemihypoplasia is evident in images: [171]

Table 4.9 Tumors identified in CSHS published reports

Benign neoplasms	Malignant neoplasms
• Pheocromcytoma [160] • Thymoma [62] • Giant cell granuloma [192] • Bladder leiomyoma [186] • CNS lipoma (x 2) [161,187] • Ocular dermoids (x 5) [176, 178, 187, 192, 195] • Syringocystoadenoma papilliferum (x 3) [53, 170, 175] • Benign vascular tumors - Pulmonary hemangiomas [176] - Facial flat angioma [191]	• Congenital rhabdomyosarcoma [180] • Malignant CNS tumor (histology not revealed [181] • Medullary carcinoma of the thyroid [188] • Basal cell carcinoma (x 2): [53, 160]

4.3 In vivo experiment I

4.3.1 hBMSC transduction: immunofluorescence and fluorescence

Efficient viral transduction with the WT and Q61R *NRAS* adenoviruses was confirmed in BMSC through HA-tag IF (Figure 4.11). BMSCs transduced with 200 µl of Q61R NRAS adenoviral stock and 300 µl of WT *NRAS* adenoviral stock appeared to transduce approximately 90% of BMCS. GFP adenoviral transduction appeared to have a similar rate of transduction with 200 µl.

4.3.2 hBMSC transduction: FGF23 protein measurment and gene expression

FGF23 protein production and gene expression were negative in all cells (figure 4.12). Due to increased apoptotic appearance in BMCS after approximately 10 days post-transduction, the experiment was terminated at day 12. Only mRNA collected in day 5 was used to assess *FGF23* expression. Statistical analysis was not performed as the experiment was only performed twice. We did not pursue additional experiments due to the robustly negative findings in the first 2 experiments.

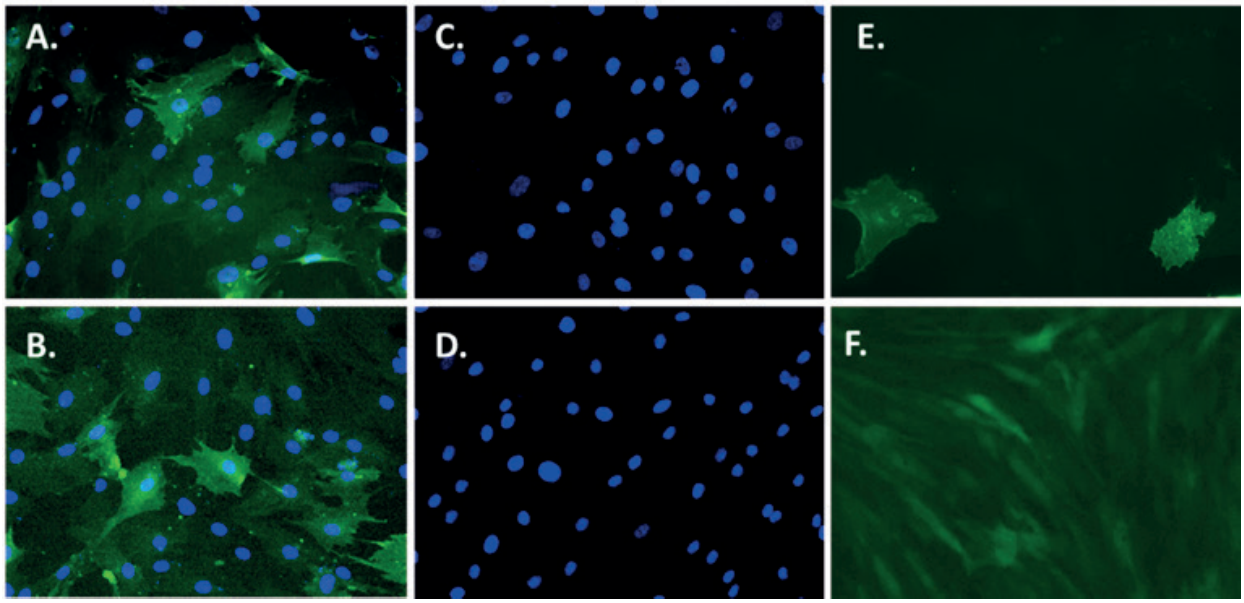

Figure 4.11 Immunoflourescence (IF) and fluorescence imaging after adenoviral transduction/plasmid transfection. (A-B) HA-tag IF on human bone marrow stromal cells (BMSC) transduced with (A) 200 µl of HA-tagged Ad-NRAS Q61R and (B) 300 µl of Ad-NRAS WT (B) adenoviral stocks. These volumes were the used for the subsequent BMCS transduction experiment. (C) HA-tag IF on BMCS that were not transduced (negative control). (D). HA-tag IF on transduced BMCSs in which the primary antibody was not added (technical negative control). (E) BMSCs transfected with a HA-tagged WT NRAS plasmid. Transfection of primary cultures is usually quite inefficient but since successful transfection had been achieved previously with this technique, it was selected as a positive control. Note: These cells were not stained with DAPI. (F) Fluorescence (not IF) in BMSC transduced with a GFP adenovirus showing efficient transduction.

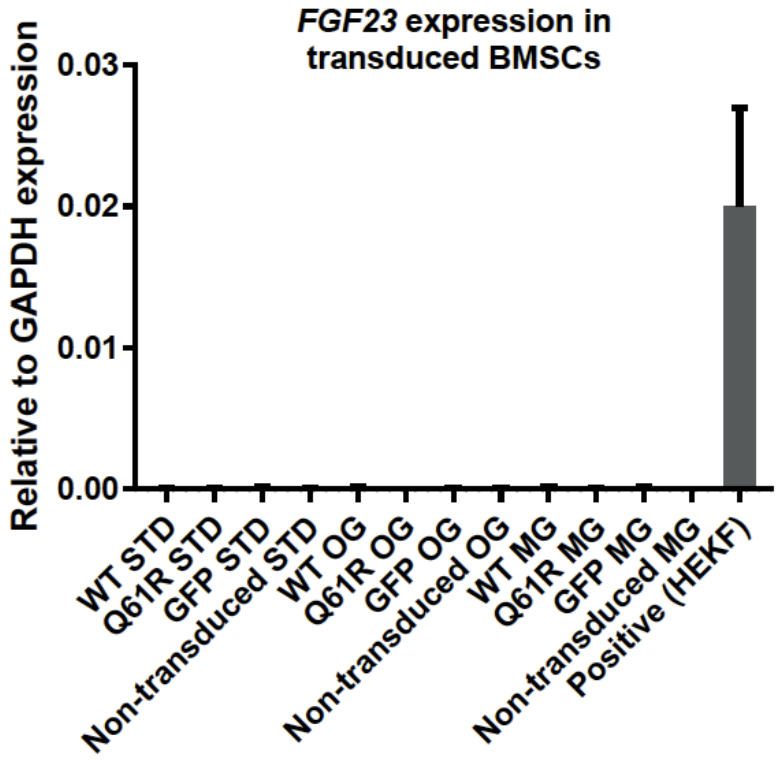

Figure 4.12 FGF23 expression in transduced BMCS.
FGF23 expression was negative in hBMSCs transduced with the Ad-NRAS Q61R adenovirus, the Ad-NRAS WT adenovirus, the GFP adenovirus and in non-transduced BMCS. Culture conditions, standard growth media, osteogenic media and endothelial media on Matrigel-coated plates (MG) did not have an effect on FGF23 expression. cDNA from a stably transfected HEK cell line expressing FGF23 served as a positive control. Results are presented as mean ± SD. Statistical analysis was not performed due to negative FGF23 expression in all hBMSCs.
Abbreviations: WT: Ad-NRAS WT adenovirus, Q61R: Ad-NRAS Q61R adenovirus, GFP: GFP adenovirus, STD: cells cultured in standard BMSC media, OG: cells cultured in osteogenic media, MG: cells cultured in endothelial media on Matrigel-coated plates.

4.4 In vivo experiment II

4.4.1 Adenoviral transduction in IDG-SW3 cells

HA-tag expression was positive with both constructs in transduced IDG-SW3 cells (figure 4.13 A). Viral transcripts were barely positive on day 16 in those cells transduced at day 2. This was not unexpected given the transient nature of adenoviral expression. Still, early adenoviral transduction was pursued in an attempt to assess whether increased activity of the MAPK pathway during earlier phases of IDG-SW3 differentiation would affect *Fgf23 expression*.

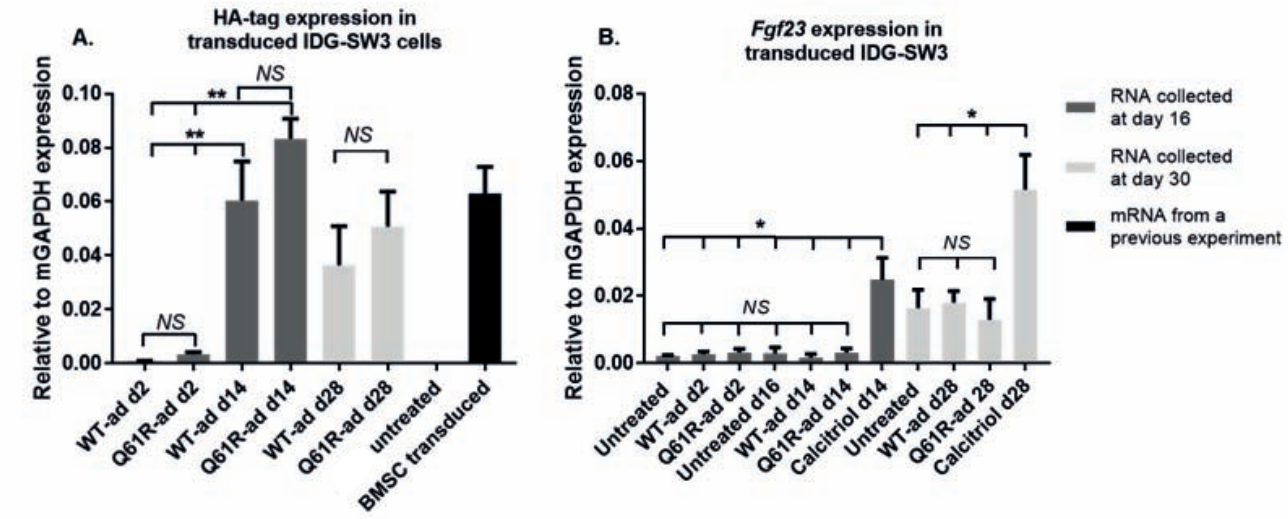

Figure 4.13 HA-tag and Fgf23 expression in transduced IDG-SW3 cells.
(A) HA-tag expression in cells transduced with the Ad-NRAS Q61R and Ad-NRAS WT adenoviruses at days 2, 14 and 28 after osteogenic differentiation.
(B) Fgf23 expression in IDG-SW3 cells after being transduced with the Ad-NRAS Q61R and Ad-NRAS WT adenoviruses at days 2, 14 and 28. Data is presented as the mean results from the 3 experiments ± standard deviation.
*Abbreviations: d: day in which a treatment was applied, WT-ad: Ad-NRAS WT transduction, Q61R-ad: Ad-NRAS Q61R transduction, NS: non-significant, *: p<0.05, **: p<0.01*
NOTE: colors shown in legend apply to graphs A and B.

4.4.2 Fgf23 expression in transduced IDG-SW3 cells

Fgf23 expression was not increased with the insertion of the *NRAS* constructs (figure 4.13 B). The positive controls, cells treated with calcitriol, did exhibit a significant increase in *Fgf23* expression. The plasmid containing mFgf23 provided a very positive signal (Ct: 17), but qPCR results are not exhibited in the figure due to the impossibility of normalizing the product to an internal control.

4.5 In vitro experiment III

4.5.1 Fgf23 expression in IDG-SW3 cells treated with CSHS hBMSCs culture media

The addition of media in which mutant CSHS BMSCs had been cultured to IDG-SW3 cells had no significant effect on *Fgf23* expression (figure 4.14).

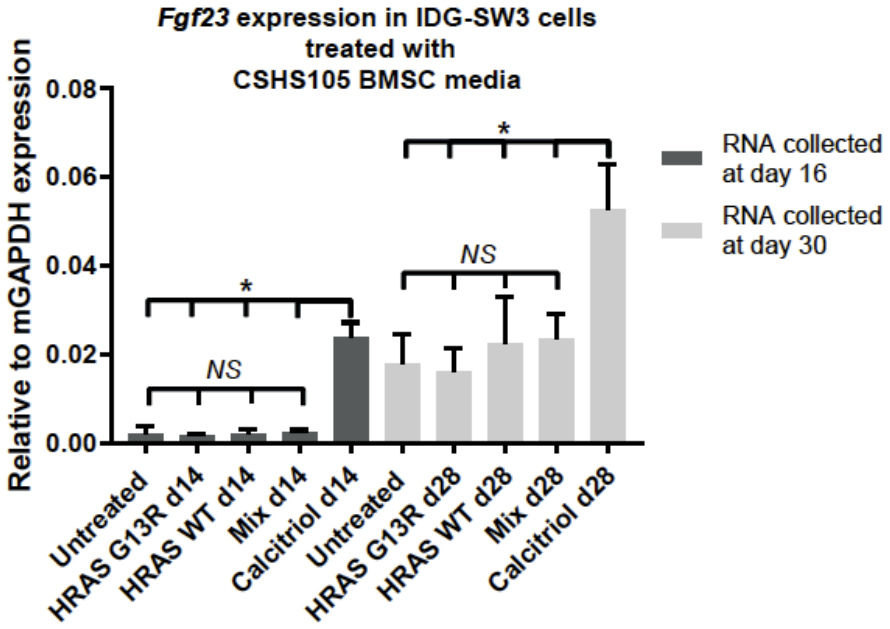

Figure 4.14 Fgf23 expression in IDG-SW3 cells that had been treated with culture media from subject's CSHS105 bone marrow stromal cells (BMSCs) including cells with the HRAS G13R mutation, WT HRAS and a combination of both. cDNA from IDG-SW3 cells treated with calcitriol on day 28 served as a positive control. Data is presented as the mean results from the 3 experiments ± standard deviation.
*Abbreviations: d: day in which a treatment was applied, HRAS G13R: IDG-SW3 cells treated with media from BMSCs harboring HRAS G13R mutation, HRAS WT: IDG-SW3 cells treated with media from BMSCs with WT HRAS, Mix: IDG-SW3 cells treated with media from both HRAS G13R and WT HRAS BMCS, calcitriol: IDG-SW3 cells treated with calcitriol Untreated: untreated IDG-SW3 cells NS: non-significant, *: p<0.05*

4.6 In vitro experiment IV

4.6.1 FGF23 expression in mutant vs WT CSHS hBMSCs

FGF23 expression was absent in both mutant and WT cells in spite of being cultured for 21 days in osteogenic conditions (figure 4.15). Statistical analyses were not performed as the experiment was only performed twice.

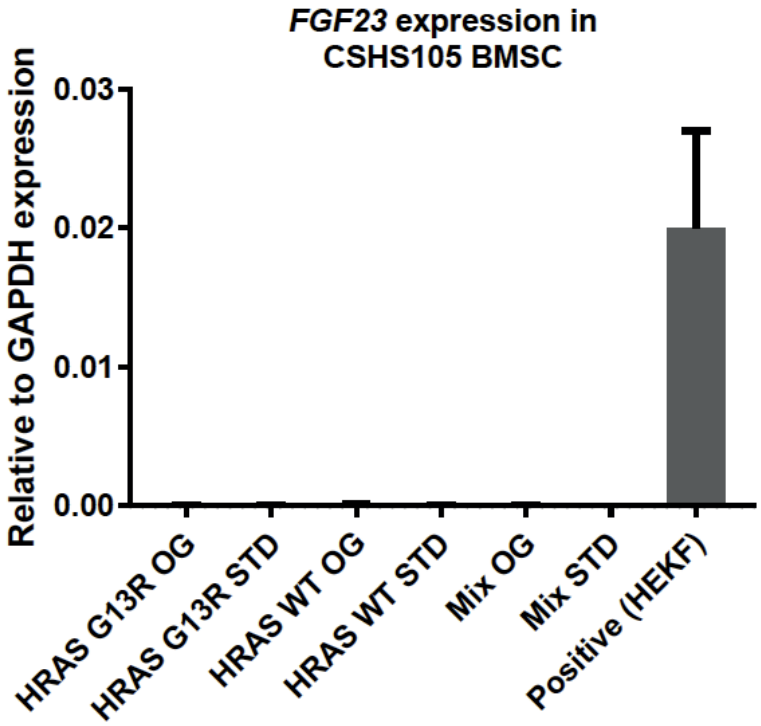

Fig 4.15 FGF23 expression in subject CSHS105's BMSC.
RNA was collected from BMCS with and without the HRAS G13R mutation and a mix of both. Cells had been for 21 days in culture in osteogenic or standard conditions. cDNA from a stably transfected HEK cell line expressing FGF23 served as a positive control.
Abbreviations: HRAS G13R: BMSCs harboring HRAS G13R mutation, HRAS WT: BMSCs without the HRAS mutation, Mix: a 1:1 combination of WT and HRAS G13R BMCS, OG: cells cultured in osteogenic media, STD: cells cultured in "standard" media.

4.7 hBMSC transplant experiment

4.7.1 Histologic features of hBMSC transplants

Histological analyses showed ossicles with very poor bone formation with both the WT and mutant BMSCs (figure 4.16). Therefore, it was not possible to draw firm conclusions or to actually characterize the histology of CSHS bone. The few areas in which bone formation was detected in the mutant transplants did not reveal any dysplastic features or differences in the mineralization pattern compared to the WT transplants.

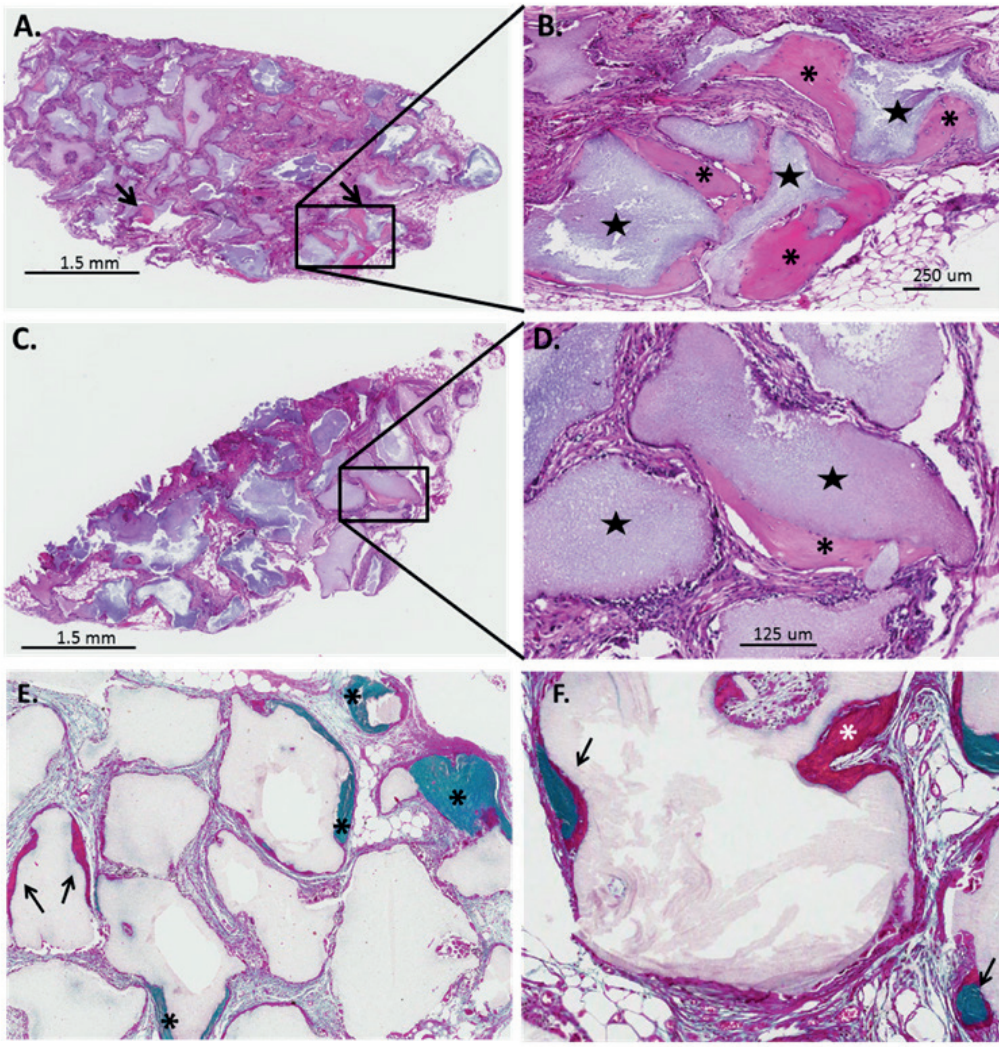

Figure 4.16. Bone marrow stromal cell (BMSC) transplant histology. (A) H&E stain of a CSHS BMSC transplant. Bone formation was scarce with the mutant cells (arrows). (B) A magnified image of (A) shows bone islets with no apparent dysplastic features (asterisks). Stars point to hydroxyapatite particles. (C) WT BMSC transplant. Some bone formation was present in most of the transplants but to a lesser extent than in the CSHS BMCS transplants. In this image bone formation was only detected in one area (box). (D) Magnified view of (C) displaying normal bone histology (asterisks). Stars point to hydroxyapatite particles. (E-F) Goldner trichrome stain on BMSC transplants (E) CSHS BMSC transplant showing areas of mineralized bone (asterisks, green) and non-mineralized osteoid (red, arrows). (F) WT BMSC transplants also displayed areas of osteoid (white asterisk) overlapping with mineralized bone (green) (arrows). The co-existance of mineralized and non-mineralized bone was observed in all the other transplants as well, which is a normal finding in BMSC transplants.

4.8 Transgenic mouse strains as a model for CSHS

4.8.1 Breeding and Genotype

Breeding from the inducible systems (models 1 and 2) yielded a normal number of pups and an anticipated inheritance pattern. In contrast, positive double transgenic offspring were not detected in 10 litters derived from the breeding couples in mouse model 3, i.e., mice harboring both Prx1cre and LSL-KrasG12D. This suggests that the systematic activation of the *Kras* transgene in cells expressing *Prx*-1 during embryogenesis is probably lethal. In consequence, the results that will be shown henceforth derive from the inducible models (models 1 and 2).

4.8.2 Weight

No significant differences were detected in weight at any time point between positive and negative controls in both mouse models 1 and 2 (figure 4.17).

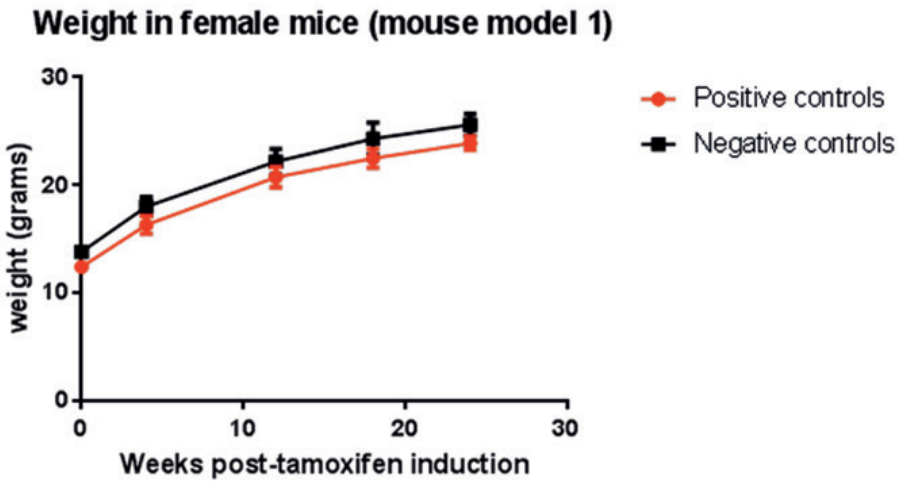

Figure 4.17. Weight comparisons between positive and negative female controls in mouse model 1. Transgenic activation of the KrasG12D transgene after tamoxifen induction did not have an effect on weight gain. Results are presented as mean ± standard deviation. T-tests were performed to compare weight between positive and negative controls at each time point. Weight comparisons in mouse model 2 did not display any significant differences either.

4.8.3 Cre monitoring through in vivo imaging of luciferase activity and verification of LSL-KrasG12D recombination in the bone

Luciferin administration in Cre recombinase positive mice exhibited a bioluminescent pattern that was consistent with the driver's tissue distribution (figure 4.18). Excision of the LSL cassette from the LSL-KrasG12D transgene was confirmed in DNA from bone after tamoxifen induction corroborating transgene recombination (data not shown).

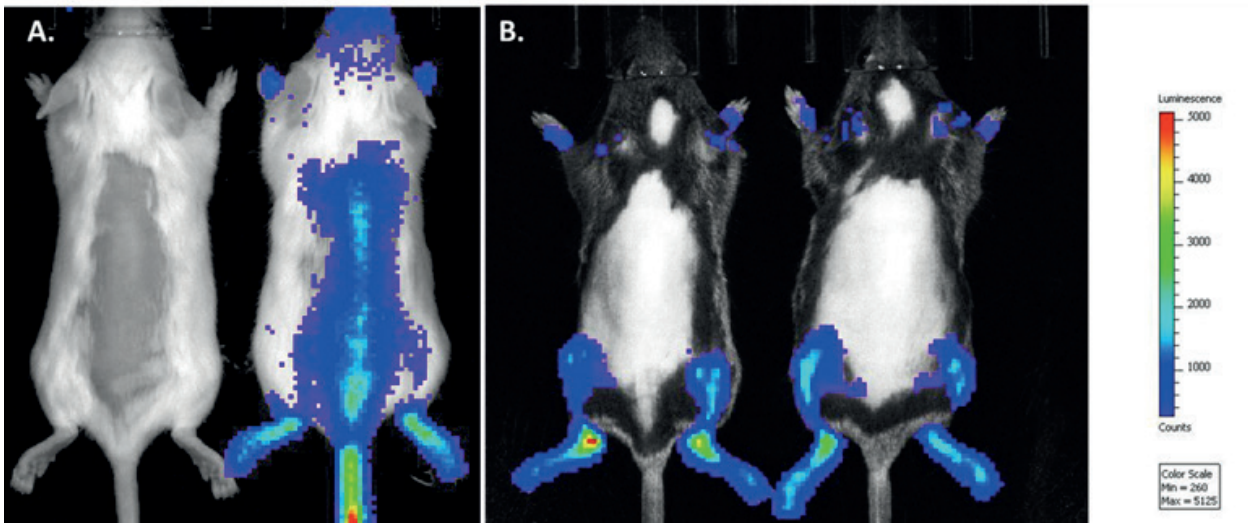

Figure 4.18. Bioluminescence in mouse models 1 and 2.
(A) Bioluminescence assessed in mouse model 1 (Col 3.6-Cre). On the left a negative Cre mouse with no signal vs a positive mouse on the right 48 hours after the last tamoxifen injection. Photonic emission is observed in the spine, limbs, tail and head of the positive control indicating skeletal cre specificity which is expected for the Col 3.6 driver. Detection of bioluminescence is facilitated in superficial bones (e.g. spine, tail etc) vs bones localized in deeper planes (e.g femur, humerus) due to light absorption by surrounding tissues. (B) Bioluminescence assessed in mouse model 2 drived by the Prx1-CreER. On the left a positive mouse and on the right a control (Cre+/Kras-) 48 hours after the last tamoxifen injection. Photonic emission is observed only in the limbs and in the ears indicating appropriate Prx1 expression. Sensitivity to tamoxifen was also assessed in both models by performing the same tests to positive controls prior to tamoxifen injections in which bioluminescence was negative (data not shown). NOTE: hair had been removed in the back and partially in the cranium to decrease light absorption by the hair.

4.8.4 X-ray imaging

Whole body X-rays did not display any abnormality or difference between positive and control mice at any time point. Increased magnification with high definition X-rays did not reveal any alterations either (figure 4.19).

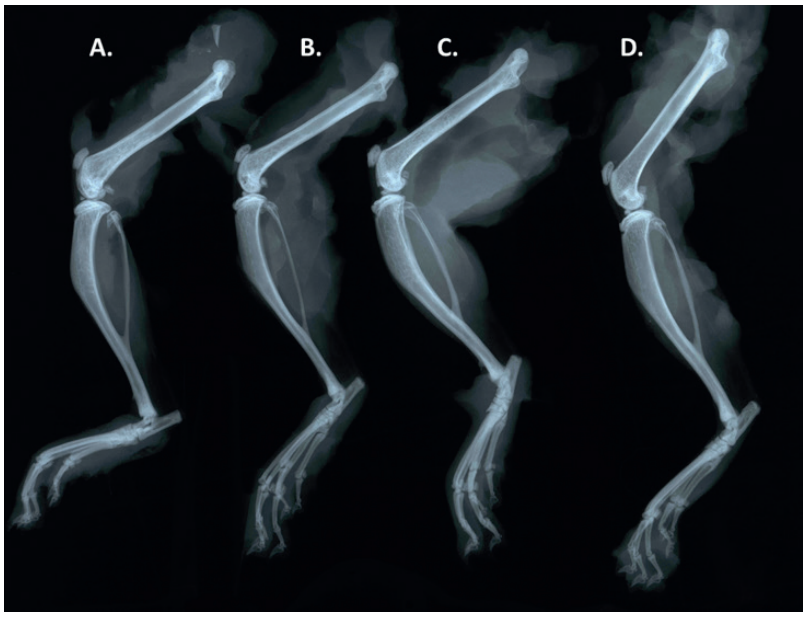

Figure 4.19. Lower limb radiographs in positive and control mice (mouse model 2)
Limbs A. and B. correspond to 7 week sibling female mice (1 months post-tamoxifen induction). Limbs C and D correspond to 15 week sibling female mice (3 months post-tamoxifen induction). Limbs A and C are positive mice (LSL-KrasG12D+/ Prx1-CreER+) whereas B and D are control mice (LSL-KrasG12D+/ Prx1-CreER+). Despite demonstrating transgenic recombination after tamoxifen induction, there was no observable abnormality in the bone of the mutant mice. These results are superimposable to mouse model 1.

4.8.5 Histology

Standard H&E sections of the lower limbs (Figure 4.20) and sections from non-demineralized, plastic embedded the upper limbs (Figure 4.21) did not reveal any abnormal histological feature or differences in mineralization between positive and negative controls at any time point.

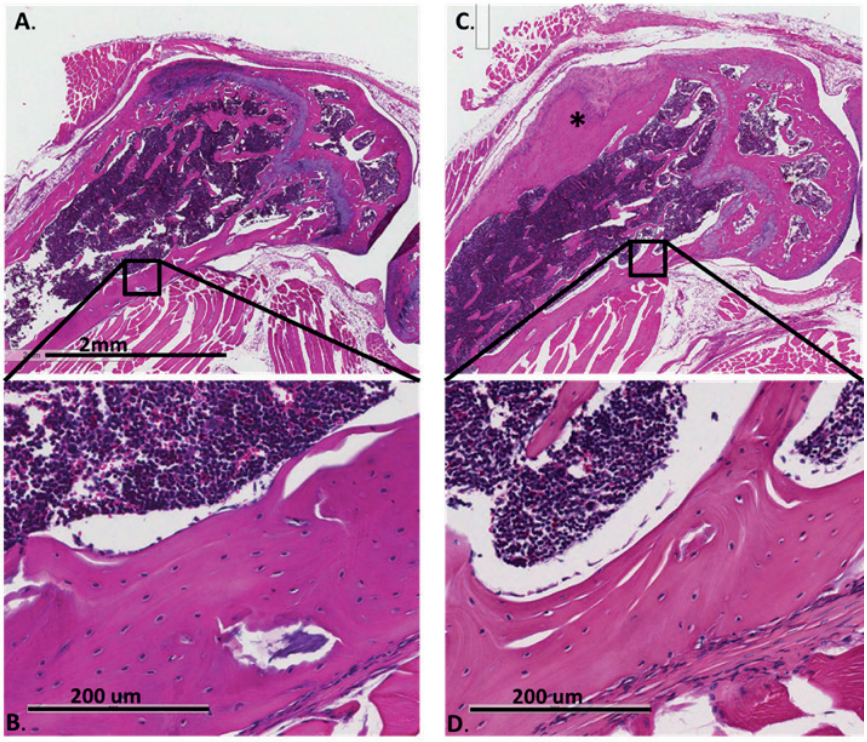

Figure 4.20. H&E staining in femoral sections from mouse model 1 (Col3.6-CreER) (A) Lower power (2X) and (B) higher power (20X) views of H&E staining of the femoral head in a 3-month negative control. (C) Lower power (2X) H&E staining of the femoral head in a 3-month positive mice. Histologically the femur does not reveal any alterations. Certain morphological differences are observed when compared to the control (asterisk) because images correspond to sections in slightly different plains. (D) Higher power (20X) view of C. Bone is distributed in a normal lamellar fashion as occurs in B. These results are superimposable to those found in mouse model 2.

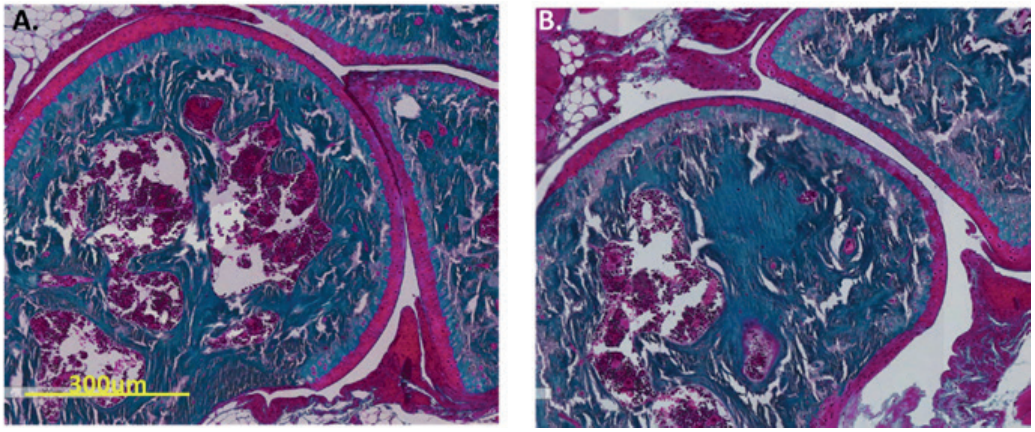

Figure 4.21. Goldner trichrome staining of plastic-embedded elbow sections from mouse model 1. (A) Elbow section from a 3 month control showing normal mineral distribution. (B) Elbow section from a 3-month positive mouse exhibiting normal mineral distribution as well.

4.8.6 Fgf23 expression in the bone

No statistical significances were detected in *Fgf23* expression between positive and negative controls at any time point in either model (figure 4.22).

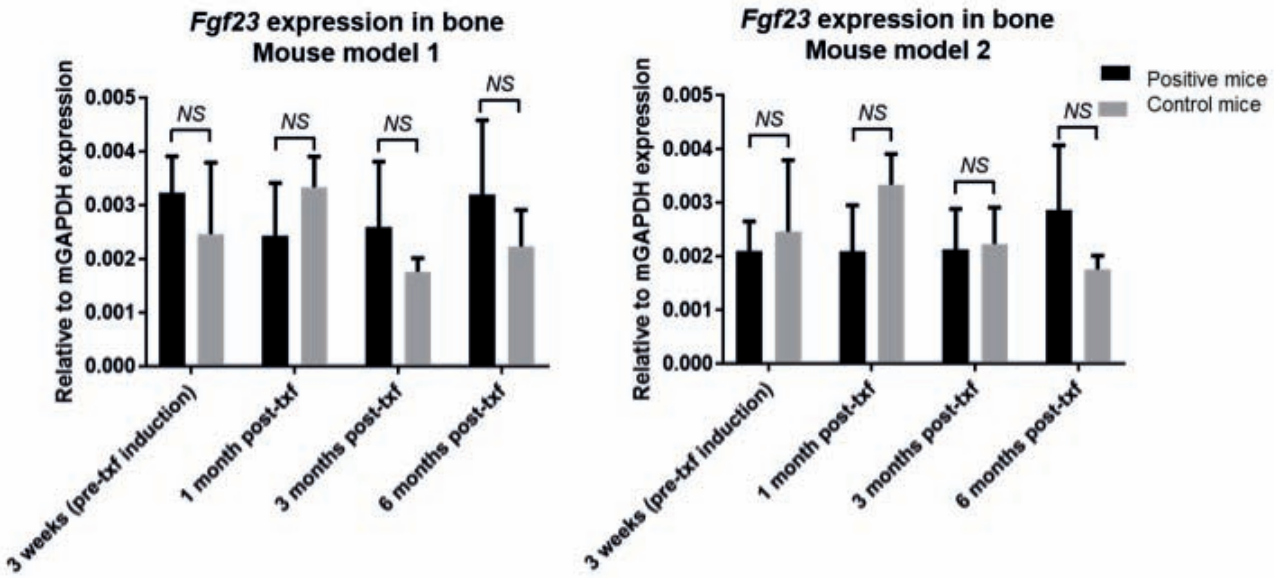

Figure 4.22. Fgf23 expression in bone from mice in models 1 and 2. RNA was extracted from flushed-marrow femurs at different time points relative to tamoxifen induction. Fgf23 expression was compared between same-aged positive and control mice. The positive technical control for Fgf23 expression, a plasmid containing mFgf23 sequence, provided a very positive signal (Ct:17), but qPCR results are not exhibited in the figure due to the impossibility of normalizing the product to an internal control. Although not shown in the figure, mFgf23 expression was absent in the negative technical control (IDG-SW3 cells day 2) (Ct>40). NS: non-significant; txf: tamoxifen

4.8.7 Biochemical profile

Blood phosphorus and the other biochemical parameters did not show any significant difference between the positive and negative controls at any time point (Table 4.10). Due to the absence of mineral alterations in the basic mineral panel, we did not pursue placing the animals in metabolic cages to measure phosphorus or calcium in the urine, nor measuring blood Fgf23.

Table 4.10 Mineral panel in female mice 1 month post-tamoxifen induction.

Biochemical parameter	Negative control (Cre-/-/Kras-/-)	Col 3.6+/-/LSL-KrasG12D+/-
Calcium mg/dL	9.6 ± 0.5	9.2 ± 0.5
Phosphorus mg/dL	9.9 ± 0.5	9 ± 0.3
Albumin g/dL	3.5 ± 0.14	3.4± 0.2
Creatinine mg/dL	0.5 ± 0.08	0.6 ± 0.1
Alkaline phosphatase U/L	5 ± 0.25	5± 0.25

Results are presented as mean ± SD. Four positive and four control animals were used per time point. Significant differences were not detected between positive and control mice in mouse model 1 and 2 at any time point (p values were >0.0.5; values are not shown in the table).